

4. SITE 1263¹

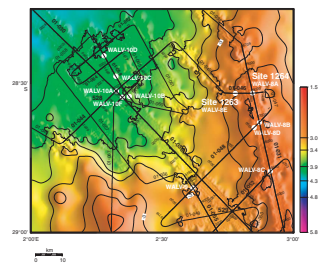
Shipboard Scientific Party²

INTRODUCTION

Site 1263 (proposed Site WALV-8E) is located at a water depth of 2717 m just below the crest of a north-south-trending segment of Walvis Ridge (Fig. F1). The site is ~250 m deeper than Deep Sea Drilling Project (DSDP) Site 525 to the southwest, where a 574-m-thick sedimentary sequence was recovered (Moore, Rabinowitz, et al., 1984). All sediments in this sequence are rich in biogenic carbonate. The Neogene section is truncated by a hiatus at 270 meters below seafloor (mbsf) so that upper Oligocene sediments overlie middle Eocene sediments. The upper Oligocene to Pleistocene sequence consists of nannofossil ooze and foraminifer-bearing nannofossil ooze. The Paleogene section includes nannofossil ooze and foraminifer-bearing nannofossil ooze and chalk and extends to 452 mbsf. DSDP Leg 74 shipboard paleontologists identified the Cretaceous/Paleogene (K/P) boundary at 452 mbsf. The lowermost part of the Site 525 sequence comprises Campanian–Maastrichtian sediments on top of basement. The sediments are cyclic in nature and are composed of nannofossil marly chalks and limestones and siltstones/sandstones of turbidite and/or slump origin down to 452 mbsf. The lowermost part of the sequence consists of sedimentary units in a basement complex. Site 525 was cored using a combination of the hydraulic piston corer and rotary drilling; as a result, recovery was poor.

Our main objective for this site was the recovery of undisturbed sediments recording critical intervals in the early Cenozoic, specifically the Paleocene/Eocene Thermal Maximum (PETM) and the period of global cooling and growth of polar ice caps across the Eocene/Oligocene (E/O) boundary into the earliest Oligocene (early Oligocene Glacial Maximum). We planned to recover 100% of the sedimentary section in multiple holes to make it possible to establish a cyclostratigraphy and to develop an astronomically tuned timescale. We aimed to fully document events across the critical intervals as well as short-lived episodes of cli-

F1. Locations of Sites 1263 and 1264 and alternate sites, p. 27.



¹Examples of how to reference the whole or part of this volume.
²Shipboard Scientific Party addresses.

mate fluctuation during the early Eocene Climatic Optimum. Site 1263 forms the shallow anchor of the Leg 208 Paleocene/Eocene (P/E) boundary depth transect.

We chose a location just below the ridge crest where the Neogene section is thin (estimated at ~50 m) to facilitate recovery of much of the Paleogene section using the advanced piston corer (APC) rather than the extended core barrel (XCB). Total sediment thickness was estimated to be 380 m (400 ms two-way traveltime [TWT] below seafloor), and the basal sediments are Campanian in age. At Site 525, a major unconformity was encountered across the E/O boundary. The Paleogene sections to the northeast of Site 525 along seismic reflection line GeoB 01-031 appear to be more complete. The seismic profiles show a series of reflectors (R_1 , $R_{P/E}$, and $R_{K/P}$) that can be traced from Site 525 to Site 1264 (proposed Site WALV-8A) (Fig. F2) to Site 1263 (common depth point 400, line GeoB 01-046) (Fig. F3) and indicate that the E/O unconformity fades laterally away from Site 525. This unconformity at Site 525 is represented in seismic line GeoB 01-031 as a zone of high-amplitude and truncated reflectors. This zone is also observed in the vicinity of Site 1264 but appears to be bounded by an additional section not present at Site 525. The next deeper prominent reflectors are the P/E boundary reflector ($R_{P/E}$) (290 ms TWT below seafloor) and the K/P boundary reflector ($R_{K/P}$) (370 ms TWT below seafloor). The correlation of reflectors from Site 525 to the proposed Sites WALV-8A, -8B, and -8C suggests that the Paleogene sequence is most complete at Sites 1263 and 1264. For the E/O and P/E boundary reflectors at Site 1263, we estimated relatively shallow burial depths of ~171 and ~276 mbsf, respectively, whereas at Site 1264, the depths were estimated to be ~238 and ~380 mbsf (velocity = 1.8 m/ms), respectively. Because the target reflectors at Site 1264 are considerably deeper than desirable for our planned Paleogene work, Site 1263 was selected as the primary site for recovery of a complete upper Maastrichtian–Paleogene sequence.

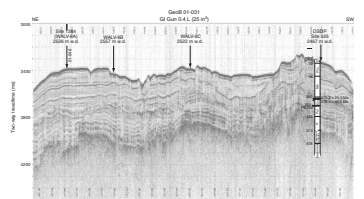
As expected, coring in four holes at Site 1263 yielded an expanded sequence of Paleogene sediment including intervals spanning climatic extremes at the E/O and P/E boundaries (see “Site 1263,” p. 15, in “Site Summaries” in the “Leg 208 Summary” chapter). Much of the upper Oligocene and Miocene was missing or condensed. Most of the section was cored using the APC, although the XCB had to be deployed for the deepest intervals (greater than ~250 mbsf). The P/E boundary interval, which was slightly deeper than estimated, was recovered at 284 mbsf using both the XCB and APC systems. Although recovery was less than optimal, it appears that 100% of the stratigraphic section was recovered in the four holes. The upper Paleocene and lower Eocene sediments exhibit distinct bedding cycles which can be correlated to cycles observed at Site 1262 and thus should be suitable for establishing a highly resolved record of regional deepwater chemistry and circulation.

OPERATIONS

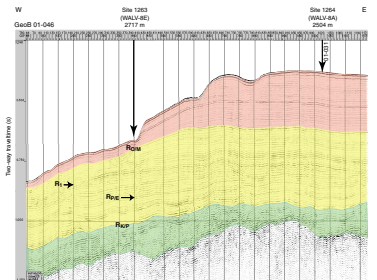
Transit to Site 1263

The 103-nmi transit to a newly approved location for Site 1263 (proposed Site WALV-8E) was accomplished at an average speed of 10.8 kt. The vessel was positioned over the new site by 1515 hr on 29 March 2003. The corrected precision depth recorder estimate for the water depth was ambiguous, within a range of 67 m. As a result, we tagged the

F2. Lines GeoB 01-031 and GeoB 01-046, p. 28.



F3. Line GeoB 01-046 with age reflector estimates, p. 29.



seafloor with the bit and then picked up the drill string ~5 m to obtain a mudline core.

The Drilling Sensor Sub (DSS), a measurement-while-drilling tool for measuring and recording drilling-dynamic data near the bit, was deployed for the first time in Hole 1263A. The first model of the DSS is a memory tool, which is 10 ft long with an 8¼-in outside diameter and a 4⅛-in through-bore to allow for core retrieval. It is made of nonmagnetic drill collar material and is positioned in the bottom-hole assembly (BHA) above the outer core barrel. The sensor's electronics and batteries are packaged in the collar wall. The tool measures weight on bit (WOB), torque on bit, annulus pressure, bore pressure, and annulus temperature. The sub was designed to Ocean Drilling Program (ODP) specifications and manufactured by APS Technology.

Four holes were drilled at Site 1263. Coring intervals, times, nominal recovery rates, core barrels that required drillover to be released from the sediment, and the deployments of the Advanced Piston Corer Temperature (APCT) tool, Tensor core orientation tool, and nonmagnetic core barrel are listed in Table T1.

T1. Coring summary, p. 69.

Hole 1263A

After two failed attempts at initiating Hole 1263A resulted in empty core barrels, the driller tagged the seafloor again, this time at 2726 meters below rig floor (mbrf). A mudline core was retrieved, and the seafloor depth was estimated to be 2728.2 mbrf (2717.1 meters below sea level) based on the recovery of the first core. Piston coring advanced to 284.1 mbsf, where the formation became too indurated for the APC. The bit was advanced by recovery when incomplete strokes were achieved on Cores 208-1263A-25H and 31H. The hole was deepened with the XCB system to the target depth of 345.6 mbsf. Active heave compensation (AHC) was used during XCB coring. AHC was turned off when the WOB indication began increasing without driller input. The operations engineer reported that the AHC deviation remained small (± 0.12 ft), whereas the cylinder force (WOB) continued to increase. The software running at the time was a version modified by Maritime Hydraulics (MH) with a velocity gain reduction and a valve overlap increase. At the next opportunity, another modified program from MH was loaded into the programmable logic controller. This software version only used the velocity gain reduction and appeared to improve performance. The AHC was used while coring Cores 208-1263A-34X, 35X, and 37X through 40X.

The hole was flushed with a 40-bbl sepiolite mud sweep and subsequently displaced with 120 bbl of sepiolite mud. The drill string was pulled back in the hole, and the bit was positioned at 82.2 mbsf for downhole logging operations. The first logging run with the triple combination (triple combo) tool string reached the bottom of the hole (347.0 mbsf). The lockable float valve closed during logging, and it required more than an hour of working the pump and logging winch controls before the tool was retracted into the drill string. The subsequent deployment of the Formation MicroScanner (FMS)-sonic tool string could not pass a bridge or tight spot at ~158 mbsf, and the instrument was recovered for a wiper trip. In a further attempt, the tool could not be lowered below 174 mbsf because of a constriction in the hole. A short logging run was made from 172 to 74 mbsf. Further logging plans were cancelled. The bit was pulled clear of the seafloor at 0125 hr on 2 April, and the vessel was offset 20 m north-northwest.

Hole 1263B

Hole 1263B was initiated at 0225 hr on 2 April and was drilled without coring to 46.0 mbsf. Coring with the APC advanced from 46.0 to 261.9 mbsf (214.8-m interval). A small interval from 196 to 197.2 mbsf was drilled to maintain a stratigraphic overlap with Hole 1263A. The APC achieved incomplete strokes on Cores 208-1263B-14H, 17H, 18H, and 19H, and the cores were advanced by recovery. The hole was deepened with the XCB from 261.8 to 338.5 mbsf. The uppermost part of the PETM interval was recovered in the core catcher of Core 208-1263B-28X (~284 mbsf). The recovery of this critical interval was compromised because of chert jammed in the core catcher. The AHC was on-line during the cutting of Cores 208-1263B-32X and 33X. The bit cleared the seafloor at 1330 hr on 3 April, and the vessel was offset 20 m south-southeast.

Hole 1263C

Hole 1263C was initiated at 1445 hr on 3 April, drilled without coring to 90.0 mbsf, spot-cored with the APC from 90.0 to 118.5 mbsf, drilled ahead to 193 mbsf, and cored from 193.0 to 285.7 mbsf. The last APC core (208-1263C-15H) contained the entire PETM clay layer. One XCB core advanced the hole to a total depth of 290.8 mbsf. Cores 208-1263C-7H, 14H, and 15H were advanced by recovery. The bit cleared the seafloor at 1830 hr on 4 April, and the vessel was offset 20 m south-southeast.

Hole 1263D

Hole 1263D was initiated at 1955 hr on 4 April and was drilled without coring to 272.0 mbsf. Cores 208-1263D-1H through 4H were obtained from the interval 272.0–286.6 mbsf. All cores were advanced by recovery, and another sample of the critical PETM boundary interval was successfully recovered.

The cored interval for the site was 778 m, and the recovered interval was 710 m (average nominal recovery = 91%). The total interval drilled without coring was 484 m.

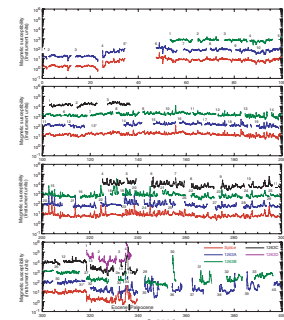
Four downhole temperature measurements (Hole 1263A: 31–116 mbsf) and one bottom water temperature measurement (Hole 1263B) with the APCT yielded an initial temperature gradient estimate of 2.5°C/100 m.

The bit was pulled clear of the seafloor and positioned at 364 m above the seafloor. Site 1263 was abandoned at 1015 hr on 5 April, and the vessel was offset in dynamic positioning mode 3.5 nmi east to Site 1264.

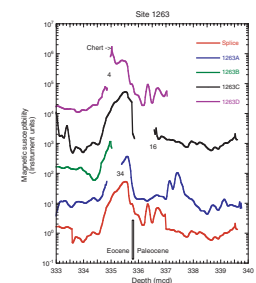
COMPOSITE DEPTH

Magnetic susceptibility (MS) and sediment lightness (L^*) data collected from Holes 1263A, 1263B, 1263C, and 1263D at 2.5-cm intervals were used to construct the composite section for Site 1263. The MS measurements were primarily used for core-to-core correlation and to construct the composite section (Figs. F4, F5). The depth offsets that define the composite section for Site 1263 are given in Table T2.

F4. MS data, p. 30.



F5. MS of P/E boundary intervals, p. 31.



T2. Composite depth scale, p. 71.

The composite depths of the top of the first six cores from Hole 1263A were calculated by assuming an 18% growth rate with depth. The composite data show that the cores from Site 1263 provide an almost continuous sequence from 48 to 340 meters composite depth (mcd), a few meters below the P/E boundary (Core 208-1263C-16X; upper Paleocene). The quality of the splice was limited by short cores; therefore, little overlap in some intervals and variable core quality resulting from APC and XCB coring (see example in Fig. F6), extremely disturbed cores resulting from the presence of chert and sediment flow (Cores 208-1263A-22H, 208-1263B-18H, and 208-1263C-4H), and two normal faults (Sections 208-1263A-4H-1, 20 cm, and 208-1263C-2H-2, 20 cm) affected our ability to make the spliced section. Nevertheless, the splice was created successfully, although some correlations between cores and their positions in the spliced record need to be handled with care. Cores 208-1263C-7H to 208-1263A-26H (~259 mcd), 208-1263C-9H to 208-1263A-28H (~283.5 mcd), 208-1263C-11H to 208-1263A-30H (~306 mcd), 208-1263C-27H to 208-1263D-1H (~318 mcd), and 208-1263B-9H, 208-1263A-27H, and 208-1263B-28X were appended to the base of the preceding cores (also see Table T3).

The top of Cores 208-1263B-18H and 19H and Core 208-1263C-4H were placed according to the growth rate for their depths (Fig. F7). The equivalent mcd for all cores below the splice (Table T3) was calculated by using the interpolated growth factor for the given mbsf depths. Following construction of the composite depth section for Site 1263, a single spliced record was assembled from the aligned core intervals from all four holes (Table T3).

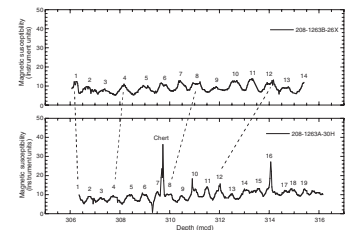
Cores that had been significantly stretched, squeezed, or disturbed by the coring process were not used for the splice, with one exception, the base of Core 208-1263A-22H. Without a stretch or squeezing correction, all points in each core are offset equally. As a result, most of the cycles are not perfectly aligned between holes (e.g., Fig. F4). Thus, the mcd values of the different holes approximate but do not precisely correspond to the same stratigraphic horizon in alternate holes.

The P/E boundary interval in the composite was taken from Core 208-1263D-4H (~340 mcd) (Fig. F5). The Site 1263 splice (Table T3) can be used as a guide to sample a single sedimentary sequence between 48 and 340 mcd, and it was used to plot other data sets from this site. The mcd-to-mbsf growth factors for Holes 1263A, 1263B, and 1263C were 18%, 18%, and 19%, respectively (Fig. F7).

LITHOSTRATIGRAPHY

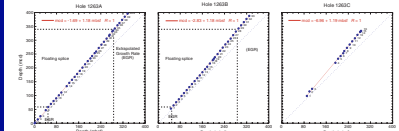
Four holes were drilled at Site 1263. Hole 1263A was cored to a depth of 400.7 mcd (340.1 mbsf); Hole 1263B was cored to 396.6 mcd (337.1 mbsf); Hole 1263C was cored to 339.9 mcd (289.1 mbsf); and Hole 1263D was cored to 337.3 mcd (286.6 mbsf). To expedite recovery of E/O and P/E boundary sections, Hole 1263B was washed to a depth of 53.3 mcd (46.0 mbsf) prior to coring. Hole 1263C was washed to 103.1 mcd (90.0 mbsf) and cored to 136.7 mcd (118.4 mbsf) to fill a recovery gap, and then it was further washed to 225.3 mcd (193.0 mbsf) to recover the P/E boundary. Hole 1263D was washed to 318.5 mcd (272.0 mbsf) to recover the P/E boundary. Physical property measurements were performed on whole-core and working-half sections from Hole 1263A; compressional wave (*P*-wave) velocity and moisture and density (MAD) measurements were made only on working halves that appeared

F6. Differential stretching of APC and XCB cores, p. 32.



T3. Splice tie points, p. 72.

F7. Mbsf vs. mcd plots, p. 33.



less disturbed. As a result, sampling was biased toward indurated sections in XCB cores.

The major lithologies recovered at Site 1263 include nannofossil ooze, chalky nannofossil ooze, foraminifer-bearing nannofossil ooze, and clay-bearing nannofossil ooze. Minor lithologies and accessories include foraminifer nannofossil ooze, ash-bearing nannofossil ooze, clayey nannofossil ooze, limestone, chert, and clay-bearing ash. The degree of induration varies from ooze to chalky ooze in the deeper part of the sequence. Combining measurements of MS, natural gamma radiation (NGR), and L^* with smear slide and visual analysis, we classified this sequence as a single lithostratigraphic unit composed of three subunits that are differentiated by minor variations in foraminifer content; MS, NGR, and L^* values; and carbonate content (Table T4; Fig. F8). Additional observations of physical properties and Mn and Fe contents are summarized in Figures F9, F10, F11, F12, F13, F14, and F15.

Description of Lithostratigraphic Units

Unit I

Interval: Sections 208-1263A-1H-1 through 40X-CC; 208-1263B-1H-1 through 33X-CC; 208-1263C-1H-1 through 16X-CC; 208-1263D-1H-1 through 4H-CC

Depth: Hole 1263A: 0.0–340.1 mbsf (0–400.7 mcd); Hole 1263B: 46.0–337.1 mbsf (53.3–396.6 mcd); Hole 1263C: 90.0–289.1 mbsf (103.1–339.9 mcd); Hole 1263D: 272.0–286.6 mbsf (318.5–337.3 mcd)

Age: Pleistocene to late Paleocene

Lithology: nannofossil ooze, foraminifer-bearing nannofossil ooze, clay-bearing nannofossil ooze, and chalky nannofossil ooze

Unit I, representing the entire section recovered at Site 1263, predominantly consists of nannofossil ooze. Variations in measured physical character, the degree of induration, and the relative abundance of skeletal components, organic matter, and clay (Figs. F8, F11) allow division into three subunits. MS and NGR values are low throughout the section, reflecting an overall high carbonate content (average = >90 wt%) (see “Geochemistry,” p. 17). A downcore reduction in porosity and increases in bulk density and P -wave velocity reflect normal consolidation trends for homogeneous sediments (Figs. F12, F13). In general, densities and sound velocities determined with whole-core multisensor track (MST) measurements correlate well with discrete sample measurements, indicating the absence of severe disturbance during core splitting (Fig. F14).

Subunit IA

Interval: Sections 208-1263A-1H-1 through 10H-6; 208-1263B-1H-1 through 5H-1, 40 cm

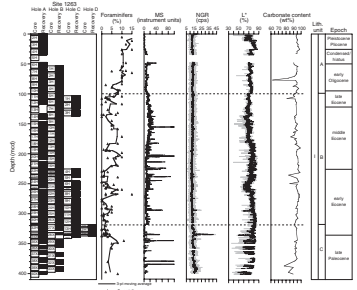
Depth: Hole 1263A: 0.0–87.3 mbsf (0–99.1 mcd); Hole 1263B: 46.0–84.4 mbsf (53.3–99.1 mcd)

Age: Pleistocene to late Eocene

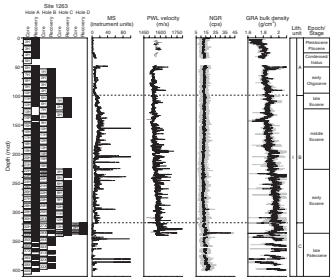
Lithology: foraminifer-bearing nannofossil ooze and nannofossil ooze

T4. Lithostratigraphic subdivisions, p. 73.

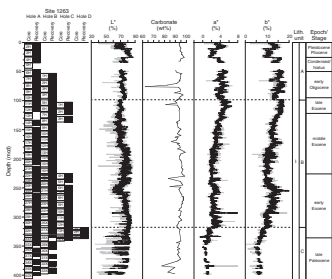
F8. Parameters used to define lithostratigraphic units, p. 34.



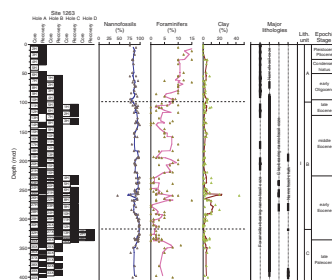
F9. MS, GRA bulk density, NGR, and PWL values, p. 35.



F10. Lightness, carbonate content, and chromaticity, p. 36.



F11. Smear slide components, p. 37.



Subunit IA is 99.1 mcd thick and grades downcore from foraminifer-nannofossil ooze to nannofossil ooze, with low MS and high L*. The uppermost 1.3 m of the subunit is enriched in foraminifers (>25%) associated with a sandy grain-size texture, which may be the result of sediment winnowing by bottom currents (e.g., Moore, Rabinowitz, et al., 1984). The grain size decreases downsection in conjunction with the increase in nannofossil percentage. In the upper 10 m of Subunit IA, color oscillates between light brownish gray and light gray. From 10 mbsf, the sediment is a uniform very pale brown; light gray oscillations start at 27 mbsf. Much of the section is mottled by large (1–6 cm in diameter) irregular pinkish white blebs that are lithologically similar to the surrounding sediment. These blebs may reflect variations in sediment diagenesis controlled by porosity differences associated with bioturbation and/or localized concentrations of organic matter. Additional evidence of bioturbation is not apparent in this interval, which could simply be the result of the homogeneous color of the sediments.

In Section 208-1263A-4H-1, a sharp, angular contact at ~80 cm (25.9 mcd) separates slightly foraminifer enriched sediment above from darker blebless sediment below (Fig. F16). This contact is coincident with downhole increases in MS and bulk density and decreases in porosity and L*^{*}; it may represent a slump or upper Neogene hiatus at Site 1263 (see “**Biostratigraphy**,” p. 8).

The basal contact of Subunit IA, located at 99.1 mcd, is marked by a gradational change toward slightly lower L*^{*}. This contact is in the E/O boundary interval (86–104 mcd) (see “**Biostratigraphy**,” p. 8). Above the contact, red-green-blue color and MS values decrease slightly, whereas L*^{*} increases slightly (Fig. F17).

Subunit IB

Interval: Sections 208-1263A-10H-7 through 31H-CC; 208-1263B-5H-1, 40 cm, through 26X-CC; 208-1263C-1H-1 through 12H-7, 50 cm

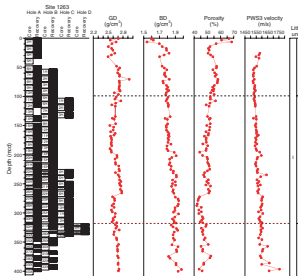
Depth: Hole 1263A: 87.3–271.6 mbsf (99.1–318.0 mcd); Hole 1263B: 84.4–271.6 mbsf (99.1–315.7 mcd); Hole 1263C: 90.0–272.6 mbsf (103.1–318.0 mcd)

Age: late Eocene to early Eocene

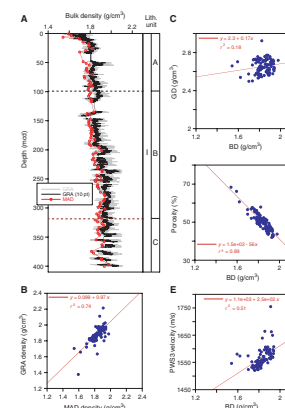
Lithology: nannofossil ooze, foraminifer-bearing nannofossil ooze, clay-bearing nannofossil ooze, and chalky nannofossil ooze

The upper boundary of Subunit IB is marked by a downhole decrease in L*^{*} and an increase in MS. Petrographically, this subunit is more diverse than Subunits IA and IC, comprising intervals of all major lithologies recovered at Site 1263 and displaying an overall downhole decrease in foraminifer abundance and increase in clay fraction and induration. Centimeter-scale chalky intervals are first observed at ~157 mcd and increase in frequency downhole. Color varies from very pale brown and light gray to white; the middle of the subunit is marked by meter-scale light–dark oscillations which may cycle at the 100-k.y. eccentricity band (see “**Age Model and Mass Accumulation Rates**,” p. 25). Furthermore, MS throughout this interval appears to cycle on a decimeter scale, suggesting possible forcing by orbital precession (Fig. F18). This signal weakens downhole as the abundance of volcanic ash increases (Fig. F18B). Irregularly shaped white blebs with halos of small, dark, opaque grains, interpreted in smear slide examination to be Mn oxides and Fe oxides, decrease in abundance downhole (Fig. F19). Halos are particularly pro-

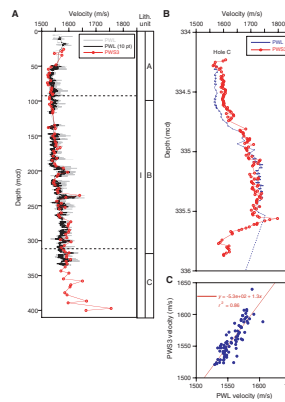
F12. Grain density, bulk density, porosity, and P-wave velocity, p. 38.



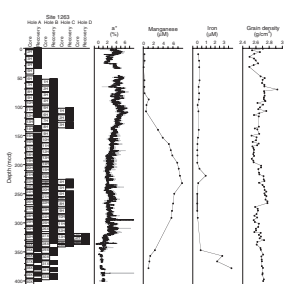
F13. Physical property measurements, p. 39.



F14. P-wave velocity data, p. 40.



F15. Chromaticity, Mn and Fe, and grain density, p. 41.



nounced between 135 and 145 mcd. Volcanic ash is first observed at 155.7 mcd, and chert nodules are first observed at 231.1 mcd. The grain density record of Site 1263 is marked by an interval of increased values between 200 and 270 mcd. This corresponds to a characteristic interval of high Mn values just below the absolute peak in Mn interstitial water concentrations (see “**Geochemistry**,” p. 17).

Peaks in MS and NGR values and a drop in L^* coincide with a 6-cm interval of reddish nannofossil clay at 295.9 mcd; this feature likely corresponds to a similar clay-rich layer recovered ~22 m above the P/E boundary at Site 1262 (Chron C24n clay layer). Roughly 2 m above the red interval at Site 1263, a darker clay-enriched horizon coincides with a series of less pronounced peaks (Fig. F20).

Subunit IC

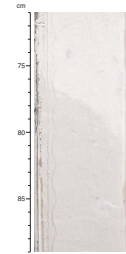
- Interval: Sections 208-1263A-32H-1 through 40X-CC; 208-1263B-27X-1 through 33X-CC; 208-1263C-12H-7, 50 cm, through 16X-CC; 208-1263D-1H-1 through 4H-CC
- Depth: Hole 1263A: 271.6–340.1 mbsf (318.0–400.7 mcd); Hole 1263B: 271.1–337.1 mbsf (318.5–396.6 mcd); Hole 1263C: 272.6–289.1 mbsf (318.0–339.9 mcd); Hole 1263D: 272.0–286.6 mbsf (318.5–337.3 mcd)
- Age: early Eocene to late Paleocene
- Lithology: nannofossil ooze, chalky nannofossil ooze

A marked downhole decrease in MS, a local minimum in carbonate content, and the onset of a gradual increase in NGR values define the upper boundary of Subunit IC. The 82.7-m-thick sequence is dominated by massive homogeneous nannofossil ooze and chalk with rare centimeter-scale intervals of partially silicified limestone. Subunit IC is almost entirely calcareous with the exception of 50–60 cm of sediment immediately above the P/E boundary. This boundary was recovered intact in two of four holes at ~335.6 mcd (Sections 208-1263C-14H-2, 149 cm, at 285.4 mbsf and 208-1263D-4H-1, 34 cm, at 285.0 mbsf) and is marked by a sharp contact between grayish brown ash-bearing clay above and light gray nannofossil ooze below. Portions of the clay-rich interval were recovered from Holes 1263A and 1263B. Bioturbation is not present in the 30 cm above the contact but is clearly visible upsection as sediment grades back into nannofossil ooze and chalk; it is not observed farther upsection because of color uniformity. The clay-rich interval is characterized by low carbonate content (see “**Geochemistry**,” p. 17) and L^* and by high MS and NGR values (Figs. F21, F8). Working-half *P*-wave velocity measurements were taken at a 1-cm sampling interval on Section 208-1263C-14H-2, revealing a stepped downhole increase in sound velocity from ~1600 to ~1800 m/s just above the contact. Below this peak, velocity returns to ~1600 m/s over a 1-m interval (Fig. F14C).

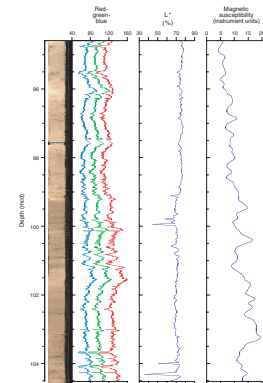
BIOSTRATIGRAPHY

Carbonate-rich Pleistocene through upper Paleocene sediments were recovered at Site 1263, with a clay layer marking the lowermost Eocene. Variably preserved nannofossils are present in all samples. Slight dissolution and overgrowth of discoasters are common. Planktonic foraminifers generally show good preservation, but fragmentation occurs across the E/O boundary interval and severe fragmentation and a barren sam-

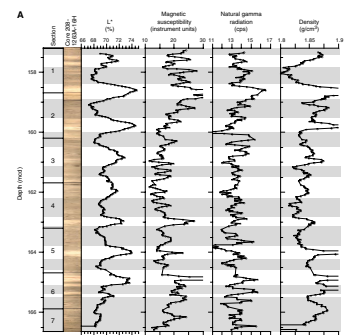
F16. Angular contact with an upper Neogene hiatus, p. 42.



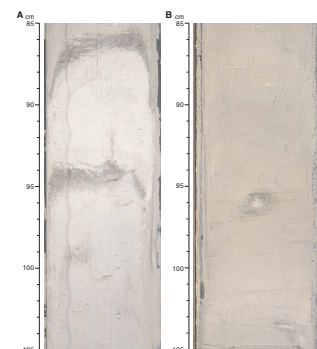
F17. Digital image, RGB color variations, L^* , and MS across the E/O boundary, p. 43.



F18. Digital image, L^* , MS, NGR, and bulk density from the Subunit IB cyclic interval, p. 44.



F19. Large and small light-colored blebs, p. 46.



ple were observed in the lowermost Eocene. Benthic foraminifers are rare in almost all samples and show generally good preservation, but dissolution and fragmentation occur in the lowermost Eocene. Benthic and planktonic foraminifers in Cores 208-1263A-38X through 40X (373–401 mcd) contain recrystallized or filled-in specimens.

Shipboard examination of calcareous nannofossils and planktonic foraminifers permitted preliminary zonal and stage assignments (Fig. F22; Tables T5, T6, T7, T8). Biochronological ages plotted against mcd delineate overall sedimentation rates (Fig. F23) (see “Age Model and Mass Accumulation Rates,” p. 25). Most of the Miocene and the upper Oligocene are not represented because of unconformities; the upper and uppermost middle Eocene are condensed, but the lower Eocene through upper Paleocene is expanded. Benthic foraminifers indicate upper abyssal depths (2000–3000 m) for the site from the middle Eocene through Pleistocene. The paleodepth could not be ascertained for the early Eocene, and it was middle lower bathyal (~1500 m) during the late Paleocene through Pleistocene (Table T9).

Calcareous Nannofossils

Calcareous nannofossil assemblages were examined in core catcher and additional samples for selected intervals of all holes. Depth positions and age estimates of key biostratigraphic markers are shown in Table T5; a distribution chart for the core catcher samples is shown in Table T6.

Nannofossils are present throughout the section and have moderate to good preservation except in a 5-cm-thick interval just above the P/E boundary, where only a few solution-resistant taxa are present. Discoasterids are generally affected by overgrowth, which prevents the recognition of some species, mainly in the Eocene.

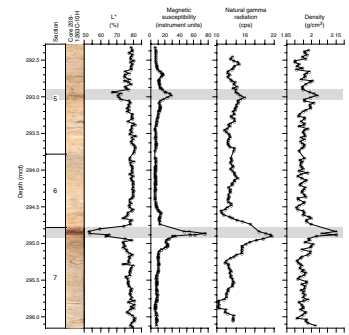
Pleistocene–Miocene (0–26 mcd)

Core 208-1263A-1H is placed in the Pleistocene, and the interval from Cores 208-1263A-2H through Sample 4H-1, 50 cm, is placed in the Pliocene. Samples 208-1263A-4H-1, 80 cm, through 4H-6, 100 cm, contain upper and middle Miocene assemblages. Lower Miocene nannofossils (of Subzone CN1c and Zone NN2) are present in Section 208-1263A-4H-CC, suggesting that there is an unconformity between these samples.

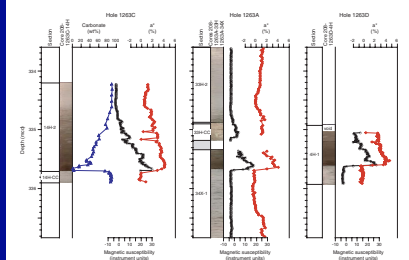
Oligocene (48–83 mcd)

Lowermost upper Oligocene and lower Oligocene sediments were recovered in Cores 208-1263A-6H through 10H and 208-1263B-1H through 4H. The nannofossil assemblages show signs of slight dissolution and generally low diversity, but the Oligocene markers *Sphenolithus ciproensis* and *Sphenolithus distentus* are present. These small sphenoliths show variable abundances and are rare or have discontinuous distributions in some intervals. Although their lowermost occurrences are not distinct events at many locations (Olafsson and Villa, 1992), at Site 1263 we could recognize the lowermost occurrences (bottom [B]) of *S. ciproensis* and *S. distentus*, which define the boundaries of Subzone CP19a and Zone CP18, respectively. Among the other Oligocene sphenoliths, *Sphenolithus predistentus* is consistently present, whereas *Sphenolithus pseudoradians* occurs sporadically and in low abundances in the

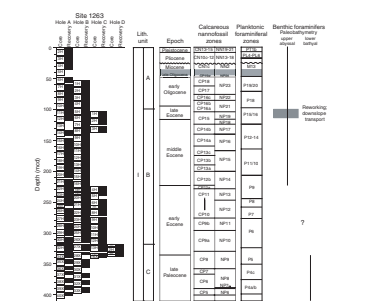
F20. Digital image, L*, MS, NGR, and bulk density of clay-enriched horizons, p. 47.



F21. Digital images of P/E boundary sections, p. 48.



F22. Planktonic foraminiferal and calcareous nannofossil biozonation, p. 49.



T5. Selected calcareous nannofossil datums, p. 74.

T6. Range and abundance of calcareous nannofossils, p. 76.

T7. Selected planktonic foraminiferal datums, p. 77.

T8. Range and abundance of planktonic foraminifers, p. 78.

upper part of its range (Cores 208-1263A-8H and 9H). Key elements of lower Oligocene assemblages such as *Reticulofenestra* spp., *Dictyococcites* spp., and *Cyclicargolithus* spp. are common to abundant, whereas representatives of the genus *Helicosphaera* are absent in most of the Oligocene, with the exception of *Helicosphaera compacta*. The zonal boundaries CP17/CP16c (NP23/NP22) and CP16c/CP16b (NP22/NP21) occur between Sections 208-1263A-8H-4 and 8H-5 and in Section 208-1263A-9H-4, respectively.

Eocene/Oligocene Boundary Interval (86–104 mcd)

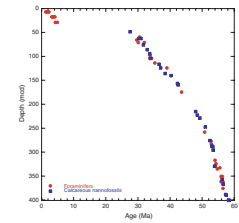
The succession of nannofossil events that characterizes the Eocene–Oligocene transition was recognized in Cores 208-1263A-9H through 11H and 208-1263B-4H and 5H. The boundary between Subzones CP16c and CP16b (NP22/NP21) and the uppermost occurrence (top [T]) of *Ericsonia formosa* is distinct. In Zones NP22 and NP21, *Isthmolithus recurvus* is rare and occurs discontinuously. In Zone NP21 (CP16b+a), an increase in the relative abundance of *Ericsonia obruta* approximates the E/O boundary. Common to abundant *E. obruta* occurs in a short interval in Sections 208-1263A-9H-5 and 10H-3, corresponding to the basal Oligocene. Among the rosette-shaped discoasters, the T of *Discoaster barbadiensis*, which together with the T of *Discoaster saipanensis* defines the boundary between Subzone CP16a and Zone CP15 (NP21/NP20), was difficult to locate because the species is rare and occurs discontinuously in the upper part of its range. The T of *D. saipanensis* in Cores 208-1263A-11H and 208-1263B-5H places sediments below these levels in the uppermost Eocene.

Eocene (95–335 mcd)

Highly diverse calcareous nannofossils are present throughout the Eocene. Major components of the assemblages are *Chiasmolithus* spp., *Coccolithus eopelagicus*, *Dictyococcites* spp., *Discoaster* spp., *Ericsonia* spp., *Reticulofenestra umbilicus*, *Reticulofenestra dictyoda*, *Sphenolithus* spp., and *Zygrhablithus bijugatus*. Overgrowth affects the solution-resistant taxa (e.g., *Discoaster* species and the middle Eocene markers *Nannotetrina* spp.) and sometimes hampers their identification. Most of the Eocene zonal boundaries could be recognized (Fig. F22), with the exception of the upper middle Eocene Subzone CP14b/CP14a (NP17/NP16) boundary and the upper lower Eocene Zone CP11/CP10 boundary. The marker for the first of these boundaries (P14b/CP14a; *Chiasmolithus solitus*) was not recognized because of preservation problems, and we used the B of *Dictyococcites scrippsae* to approximate this boundary. As for the second boundary (CP11/CP10), its marker species *Toweius crassus* is present in older sediments in the CP9b zonal interval and the species is thus not reliable. Three nannofossil events (the B of *D. scrippsae*, the B of *Dictyococcites bisectus*, and the T of *Chiasmolithus grandis*) characterize upper middle Eocene Zone NP17, which has a duration of 3.2 m.y., and they all occur in Core 208-1263A-7H, suggesting that this interval is condensed.

The lower Eocene (Cores 208-1263A-22H through 32H and 208-1263B-13H through 26X) assemblages are characterized by abundant *Tribracliatius orthostylus*, common *Sphenolithus radians*, and discoasters (e.g., *Discoaster lodoensis*, *Discoaster diastypus*, and *Discoaster multiradiatus*).

F23. Sedimentation rates, p. 50.



F29. Selected benthic foraminifers, p. 79.

Paleocene/Eocene Boundary Interval (322–336 mcd)

Specimens of the *Rhomboaster-Tribrachiatus* plexus belonging to the species *Tribrachiatus contortus* and preceding the lowest occurrence of the lowermost Eocene marker *T. orthostylus* have rare and scattered occurrences in Cores 208-1263A-29H through 32H and are poorly preserved because of recrystallization. Therefore, the boundary between Subzones CP9b and CP9a (NP11 and NP10) could not be confidently recognized and it is placed tentatively at the lowermost occurrence of *S. radians*. In the sediments just above the benthic extinction event (BEE) (Sections 208-1263A-33X-2 through 34X-1), common specimens of *Rhomboaster cuspis* and *Rhomboaster calcitrapa* are present and provide a distinct nannofossil biostratigraphic signal. As observed at Site 1262, the genus *Fasciculithus* shows a distinct distribution pattern in its final range, with a decrease in abundance coincident with the increase of *Z. bijugatus* (between Samples 208-1263A-33H-2, 110 cm, and 13H-2, 126 cm), just above the BEE. The genus *Fasciculithus* has its uppermost occurrence in Cores 208-1263A-32H and 208-1262B-27X.

Paleocene (336–401 mcd; bottom of sequence)

Paleocene assemblages belonging to the biostratigraphic interval from Zones CP8 through CP4 (NP9–NP5) are present in the lower part of the sedimentary record (Cores 208-1263A-35X through 40X, Cores 208-1262B-30X through 32X, and Sections 208-1262C-14H-CC through 16X-CC). Nannofossils are generally diverse and moderately preserved. Common *Discoaster* taxa (*D. multiradiatus*, *Discoaster nobilis*, and *Discoaster mohleri*) characterize the upper part of the Paleocene interval. Other important components of the assemblages are *Toweius* spp., *Coccolithus pelagicus*, *Prinsius* spp., *Chiasmolithus* spp., *Cruciplacolithus* spp., *Heliolithus* spp., and *Ericsonia* spp. All the key elements for the biostratigraphic classification of this time interval were recorded, and the boundaries between upper Paleocene Zones CP8 through CP4 (NP9–NP5) were recognized (Fig. F22).

Planktonic Foraminifers

Examination of core catcher samples revealed that planktonic foraminifers are abundant and generally well preserved throughout much of the section, although specimens display signs of diagenetic alteration in the lowermost part of the cored section (upper Paleocene). Additional samples were taken through a short stratigraphic interval that contains the P/E boundary interval in Hole 1263A. Shipboard examination of the assemblages facilitated preliminary determination of the stratigraphic ranges for various taxa (Table T8).

Pleistocene–Miocene (0–29 mcd)

Section 208-1263A-1H-CC (2.06 mcd) contains a typical Pleistocene temperate water fauna. Common species are *Globorotalia crassaformis*, *Globorotalia truncatulinoides*, *Globorotalia tumida*, *Globoconella inflata*, *Globigerinoides ruber*, *Globigerinoides sacculifer*, *Globigerinella siphonifera*, *Hirsutella scitula*, and *Neogloboquadrina pachyderma* (dextral). The base of Subzone Pt1a (~2.02 Ma), used to approximate the Pliocene/Pleistocene boundary, is placed between Sections 208-1263A-1H-CC and 2H-CC at an estimated depth of ~7 mcd.

The T of *Sphaeroidinellopsis seminulina* falls between Sections 208-1263A-2H-CC and 3H-CC, indicating that the base of the lower Pliocene Zone PL4 (3.18 Ma) is at ~18 mcd. The presence of *Paragloborotalia kugleri*, *Globoquadrina dehiscens*, and *Catapsydrax dissimilis* in Section 208-1263A-4H-CC indicates an early Miocene age for that sample (Subzone M1b). Thus, an unconformity at ~29 mcd separates lower Pliocene from lower Miocene sediments.

Oligocene (48–83 mcd)

Poor core recovery and reworking precluded recognition of the Oligocene/Miocene boundary. Core 208-1263A-5H is mostly barren, but Section 208-1263A-5H-CC (34.54 mcd) contains *P. kugleri*, which places this assemblage in the lowermost Miocene (Zone M1). Mixed with this lower Miocene assemblage, however, are Oligocene taxa (e.g., *Globigerina angulisuturalis* and *Chiloguembelina cubensis*), indicating extensive reworking. Moreover, Section 208-1263A-6H-CC (56 mcd) yields an upper-lower Oligocene assemblage (P20) that contains characteristic species such as *C. cubensis*, *Paragloborotalia opima*, *Globoquadrina venezuelana*, *Globigerina euapertura*, and *Globigerina ciperoensis*. Sections 208-1263A-7H-CC (68 mcd) and 8H-CC (79 mcd) are assigned to Zone P19 based on the presence of rare “*Globigerina*” *ampliapertura*.

Eocene/Oligocene Boundary Interval (83–110 mcd)

The E/O boundary interval is in Cores 208-1263A-9H through 11H. The presence of species of the genus *Pseudohastigerina* and the absence of typical late Eocene taxa places Sections 208-1263A-9H-CC (90 mcd) and 10H-CC (100 mcd) in Zone P18, the lowermost zone of the Oligocene. The assemblage in Section 208-1263A-10H-CC is heavily fragmented and contains numerous hantkeninid spines that have been reworked up into the lowermost Oligocene. Section 208-1263A-11H-CC (110 mcd) is assigned to the upper Eocene (Zones P15–P16) and is best described as a “*Globigerinatheka* sand.” The scarcity of other taxa in this sample reflects intense dissolution and/or sorting.

Eocene (110–335 mcd)

The overall absence of several key tropical marker species due to the location of the site in a temperate region reduced the level to which the Eocene could be biostratigraphically subdivided. Section 208-1263A-12H-CC (118 mcd) straddles the upper/middle Eocene boundary and is assigned to Zone P15 based on the presence of *Turborotalia cerroazulensis*, *Turborotalia cerroazulensis cocoaensis*, and *Globigerinatheka semiinvoluta* and the absence of morozovellids and acarininids. The base of Zone P15 is placed at 124 mcd (between Sections 208-1263B-6H-CC and 7H-CC), as indicated by the co-occurrence of *Acarinina* spp. and *T. cerroazulensis cocoaensis*.

The absence of *Orbulinoides beckmanni* hinders differentiation of Zones P12, P13, and P14, and Sections 208-1263A-14H-CC through 16H-CC (142–167 mcd) are thus loosely assigned to Zones P12–P14. Taxa common to these *Hantkenina* spine-bearing assemblages are *Acarinina spinuloinflata*, *Acarinina bullbrooki*, *Acarinina crassata*, small *Morozovella spinulosa*, and *Globigerinatheka* spp.

Only two specimens of *Morozovella aragonensis* are found in Section 208-1263A-17H-CC (177 mcd), marking the uppermost occurrence of

this species. Consequently, Sections 208-1263A-17H-CC and 18H-CC are assigned to Zone P11. The relative abundance of *M. aragonensis* increases downhole in Sections 208-1263A-18H-CC through 26H-CC (187–270 mcd). The absence of such dissolution-susceptible marker species as *Hantkenina nuttalli* and *Planorotalites palmerae* hampers differentiation of Zones P9 and P10, the boundary of which demarcates the middle/early Eocene boundary. We substituted a downhole reduction in globigerinathekid diversity and concomitant increases in the relative abundances of *Morozovella caucasica*, *Subbotina higginsi*, and “*Globigerinatheka*” *semmi* as alternative biostratigraphic indexes. Using these criteria, we tentatively place the middle/lower Eocene boundary in Section 208-1263A-19H-CC at 199 mcd. Sections 208-1263A-20H-CC through 23H-CC (210–240 mcd) are assigned to Zone P9 based on the presence of common, well-developed morphotypes of *M. caucasica*.

The absence of the marker taxon *P. palmerae* prevents the distinction between Zones P8 and P9. Thus, a downhole decrease in the relative abundance of *M. caucasica* is used to tentatively assign Sections 208-1263A-24H-CC and 25H-CC (252–256 mcd) to Zone P8. Section 208-1263A-26H-CC is assigned to Zone P7 based on the co-occurrence of *M. aragonensis* and extremely rare *Morozovella formosa*. Sections 208-1263A-27H-CC through 31H-CC (281–318 mcd) are ascribed to Zone P6. Common taxa in these P6 assemblages are *Morozovella subbotinae*, *Morozovella gracilis*, *Morozovella marginodentata*, *Morozovella aequa*, *Acarinina soldadoensis*, *Acarinina coalingensis*, “large biserial” taxa, *Igorina broedermanni*, *Subbotina* spp., and *Globanomalina planoconica*. Rare specimens of *Morozovella velascoensis* are present in Section 208-1263A-32H-CC (330 mcd), indicating that the Zone P5/P6 boundary is at ~324 mcd.

Paleocene/Eocene Boundary Interval (334.68–336.58 mcd)

Preservation steadily declines downhole through the lowermost Eocene. Planktonic foraminifer shell sizes decrease as levels of shell fragmentation increase between Samples 208-1263A-33H-2, 108 cm, and 34X-1, 2 cm. Preservation continues to decline downhole until Sample 208-1263A-34X-1, 27 cm (~335.61 mcd), which is barren. The base of this clay-rich interval is correlative with the BEE at the P/E boundary (~335.66 mcd). Below this clay-rich interval (Samples 208-1263A-34X-1, 37 cm, through 124 cm), preservation improves and abundant large planktonic foraminifers are present. Assemblages from below the P/E boundary are composed of taxa such as *M. subbotinae*, *M. aequa*, *M. velascoensis*, *Morozovella oclusa*, *Subbotina velascoensis*, *G. planoconica*, *A. soldadoensis*, and *A. coalingensis*.

Paleocene (336–401 mcd; bottom of sequence)

The oldest sediments recovered from Site 1263 are of the upper Paleocene Zone P4 (~57.1 Ma). The Zone P4/P5 boundary is delimited by the T of *Globanomalina pseudomenardii* (55.9 Ma) at ~351 mcd, and Zone P4 extends downsection from Sections 208-1263A-36X-CC through 40X-CC. Preservation declines through this interval, with specimens exhibiting chalky infilling and signs of recrystallization. Assemblages in this interval are composed primarily of *G. pseudomenardii*, *G. planoconica*, *M. velascoensis*, *Morozovella acutispira*, *Morozovella conicotruncata*, *Morozovella angulata*, *Acarinina mckannai*, *Acarinina subphaerica*, *Acarinina nitida*, and assorted igorinids and subbotinids.

Benthic Foraminifers

All core catcher samples from Hole 1263A were semiquantitatively investigated for benthic foraminifers. In addition, samples were studied from intervals in Holes 1263B and 1263C (which were not recovered in Hole 1263A) and across the P/E boundary in Holes 1263A and 1263C (Table T9).

In most samples, benthic foraminifers are outnumbered by planktonic foraminifers, with the exception of those in the lowermost Eocene in which the assemblages have suffered strong dissolution. Preservation is generally good, with the exception of samples with strong dissolution in the lowermost Eocene and samples from the lowermost three cores, where specimens are recrystallized and filled in (Sections 208-1263A-38X-CC and 40X-CC; 391–401 mcd).

Benthic foraminiferal assemblages from Site 1263 indicate deposition at upper abyssal depths (2000–3000 m) in samples from above 234 mcd (Sections 208-1263A-1H-CC through 22H-CC). Paleodepths could not be estimated for Section 208-1263A-23H-CC through Sample 34X-1, 27–28 cm (241–336 mcd; lower Eocene), because benthic foraminifers are not reliable depth indicators during that period (Müller-Merz and Oberhänsli, 1991). Samples below 336 mcd were deposited at middle lower bathyal depths (~1500 m).

Sections 208-1263A-1H-CC through 3H-CC (2–21 mcd) contain assemblages with common *Globocassidulina subglobosa*, *Cibicidoides wuellerstorfi*, *Cibicidoides mundulus*, *Oridorsalis umbonatus*, and *Pyrgo* spp., with varying relative abundances of the *Uvigerina peregrina* group, *Pullenia* spp., and minor *Osangularia culter*, *Bulimina rostrata*, *Bolivinita pseudothalmanni*, *Gyroidinoides* spp., *Siphonodosaria* spp., *Nuttallides umbonifera*, and *Epistominella exigua*. At present, similar assemblages occur along Walvis Ridge at water depths between ~2000 and 3300 m (Schmiedl et al., 1997). At these depths, bottom waters are derived from northern sources (North Atlantic Deep Water).

Assemblages in Sections 208-1263A-4H-CC through 6H-CC (35–56 mcd) resemble the assemblages in the shallower samples but lack *C. wuellerstorfi* and mainly contain long-lived abyssal to lower bathyal taxa such as *Cibicidoides* spp., *O. umbonatus*, *Pullenia* spp., and *Siphonodosaria* spp.

Sections 208-1263A-7H-CC through 11H-CC (69–110 mcd) contain typical upper abyssal upper Eocene through lower Oligocene assemblages including *Bulimina semicostata*, *Bulimina elongata*, *C. mundulus*, *O. umbonatus*, *Gyroidinoides* spp., *Anomalinoidea spissiformis*, *Nonion havanense*, and common *Siphonodosaria* spp. as well as unilocular, laevidentalinid, and pleurostomellid taxa and rare *N. umbonifera* and *Vulvulina spinosa*. Section 208-1263A-10H-CC (100 mcd) has abundant large-ribbed *Orthomorphina* spp., indicative of downslope transport.

Sections 208-1263C-1H-CC through 208-1262A-22H-CC (113–234 mcd) are species rich and are characterized by the presence of abundant very large specimens of *Nuttallides truempyi* and large *B. semicostata*, *Cibicidoides praemundulus*, and (as in the assemblage above) *O. umbonatus*, *Gyroidinoides* spp., *A. spissiformis*, *N. havanense*, common *Siphonodosaria* spp. as well as unilocular, laevidentalinid, and pleurostomellid taxa. Section 208-1263C-1H-CC (113 mcd) has abundant large *Orthomorphina* spp., indicative of downslope transport, as well as some specimens of *Plectofrondicularia paucicostata* that (as *Plectofrondicularia lirata*) have been recorded from the upper Eocene at several South Atlan-

tic DSDP sites to the east and west of the Mid-Atlantic Ridge over a large depth range (Tjalsma, 1983; Clark and Wright, 1984).

Section 208-1263A-23H-CC through Sample 34X-1, 27–28 cm (241–336 mcd), contain assemblages that are less species rich, as is typical for the lower Eocene in the South Atlantic Ocean over a large depth range (Clark and Wright, 1984; Müller-Merz and Oberhänsli, 1991; Thomas and Shackleton, 1996). These assemblages are characterized by the presence of *Aragonia aragonensis* and small smooth-walled species of *Abyssamina* and *Clinapertina*, small smooth-walled buliminid species (e.g., *Bulimina kugleri* and *Bulimina simplex*), and small specimens of *N. truempyi*, *A. spissiformis*, and *N. havanense*. *Tappanina selmensis* and *Siphogenerinoides brevispinosa* are rare, as are specimens of unilocular, laevidentalinid, and pleurostomellid taxa. In the lowermost part of this interval (Samples 208-1263A-33H-2, 124–125 cm, through 34X-1, 27–28 cm [334.84–335.61 mcd]), species richness is extremely low and long-lived unilocular and laevidentalinid taxa are absent. Similar assemblages have been described from immediately above the P/E BEE on Walvis Ridge (Müller-Merz and Oberhänsli, 1991; Thomas and Shackleton, 1996).

The BEE occurs between Samples 208-1263A-34X-1, 27–28 cm (335.61 mcd), and 34X-1, 37–38 cm (335.71 mcd); Samples 208-1263B-28X-CC, 38–30 cm (335.09 mcd), and 29X-1, 1–2 cm (342.86 mcd); and Samples 1263C-14H-2, 144–145 cm (335.65 mcd), and 14H-CC, 3–4 cm (335.74 mcd). Samples immediately above the lithologic contact of clay-rich material over carbonate-rich material are almost barren but contain minute specimens of *N. truempyi*, *T. selmensis*, *O. umbonatus*, *B. kugleri*, *B. simplex*, and *Abyssamina quadrata*; most are dominated by *N. truempyi*.

Samples below the BEE through the bottom of the hole (336–401 mcd) contain typical extremely species rich Paleocene lower bathyal through abyssal assemblages including *Stensioeina beccariiformis*, *Aragonia velascoensis*, *Paralabamina lunata*, *Paralabamina hillebrandti*, *Pullenia coryelli*, large thick-walled species of *Gyroidinoides* such as *Gyroidinoides beisseli*, *Gyroidinoides globosa*, and *Gyroidinoides quadrata*, and large agglutinant taxa (e.g., *Clavulinoides* spp., *Marssonella oxycona*, and *Gaudryina pyramidata*). In contrast to Site 1262, lower bathyal indicator species such as *Alabamina creta*, *Bolivinoidea delicatulus*, *Coryphostoma midwayensis*, and *Neoflabellina semireticulata* are present, indicating middle lower bathyal depths (~1500 m).

PALEOMAGNETISM

Drilling and Core Orientation

Every other core at Site 1263 was recovered with a nonmagnetic core barrel until the first barrel had to be drilled over (see Table T1 and “Operations,” p. 2). As at Site 1262, no obvious differences were noticed in the magnetic data between sediments recovered with the nonmagnetic core barrel and those recovered with the standard core barrel.

All APC cores from Holes 1263A, 1263B, and 1263C were successfully oriented with the Tensor tool, with the exception of Cores 208-1263A-1H through 3H, 208-1263B-19H and 25H, and 208-1263C-1H through 3H (see Table T1 and “Operations,” p. 2).

Archive-Half Measurements

The archive halves of 93 cores from Holes 1263A, 1263B, 1263C, and 1263D were measured in the pass-through magnetometer. Natural remanent magnetization (NRM) was measured on all cores. Most cores were demagnetized at 10 and 15 mT. A strong vertical overprint was largely removed by demagnetization to 10 mT. In some cases, 15-mT demagnetization appeared to further resolve the characteristic polarity.

Section 208-1263B-2H-3 was demagnetized up to 25 mT. Although the additional demagnetization changed the inclination slightly, it did not significantly affect the polarity interpretation. Examples of demagnetization behavior of this section are shown in Figure F24. Demagnetization steps above 10 mT show quasi-univectorial decay toward the origin, indicating that the characteristic remanent magnetization was largely isolated through alternating-field (AF) demagnetization.

Both the archive and working halves of Section 208-1263B-29X-4 were demagnetized to 15 mT as part of an experiment to determine the source of bias in the declination data (see “Paleomagnetism,” p. 20, in the “Explanatory Notes” chapter).

Discrete Sample Measurements

Twelve pilot samples were stepwise AF demagnetized and confirmed removal of a vertical overprint in most cases by 10 mT and in some cases by 5 mT. Inclinations after demagnetization to 15 mT generally agreed with the archive-half pass-through data (Fig. F25). When the pass-through data are not well resolved, the discrete samples often provide a less ambiguous polarity determination, suggesting that shore-based discrete sample analysis will play an important role in clarifying the magnetostratigraphy. In many cases, the discrete sample directions became erratic when demagnetized to values $<1 \times 10^{-3}$ A/m. Below this value, intensities of the samples began to approach the stated resolution of the magnetometer for discrete samples (4×10^{-4} A/m).

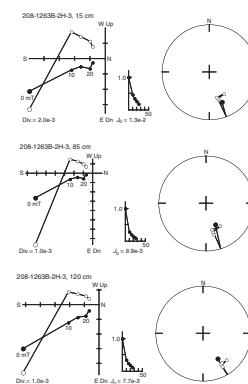
Remanent Magnetization Intensity

In Figure F26, we plot intensities of remanent magnetization with depth both before and after 15-mT AF demagnetization. The magnitude of the initial NRM is on the order of 10^{-2} to 10^{-1} A/m, primarily reflecting the strong low-coercivity overprint, as observed at Site 1262. After demagnetization to 15 mT, lower intensity values ($\sim 10^{-4}$ A/m) are observed from 0 to 30 mcd and from 330 mcd to the bottom, with higher values ($\sim 10^{-3}$ A/m) in between. The variations of magnetization after 15-mT demagnetization are well matched between holes, as is MS (see Fig. F4). Intensity variation of the soft component (0–10 mT) is roughly proportional to that of the hard-coercivity component (>15 mT).

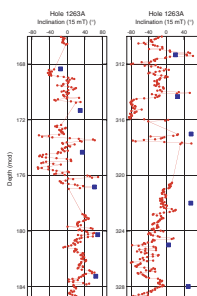
Magnetostratigraphy

The very soft nannofossil ooze at Site 1263 does not carry a clean signal (Fig. F27), making the magnetostratigraphy difficult to interpret. Preliminary chron assignments (Fig. F27; Table T10) were attempted where a reversal appears to be particularly well resolved or where the same feature is seen in sediments from more than one hole. However, the assignments are based largely on biostratigraphic age estimates and

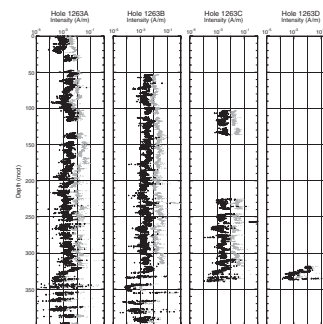
F24. Vector endpoint, intensity, and equal-area diagrams, p. 51.



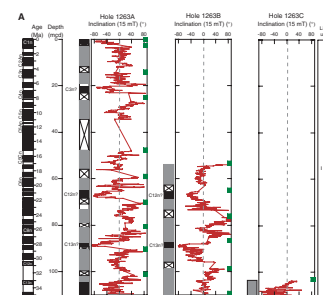
F25. Inclinations from discrete samples and half cores, p. 52.



F26. Intensities, 0- and 15-mT demagnetization, p. 53.



F27. Magnetostratigraphic interpretation, p. 54.



T10. Magnetostratigraphic age-depth tie points, p. 80.

not on identifiable reversal patterns. Note that none of the chron assignments should be used with any real confidence.

A relatively well resolved normal polarity interval at ~20–23 mcd in Hole 1263A is likely to be part of Chron C3n based on the top of nanofossil datum *Amaurolithus* spp. (4.56 Ma) at 12.07–23.29 mcd. Two normal events appear to be at least partially resolved in Holes 1263A and 1263B at ~65–69 mcd and ~88–89 mcd. The upper normal event is assigned to Chron C12n (30.479–30.939 Ma) based on the bottom of the nanofossil datum *S. distentus* (30.32 Ma) and the T of *S. pseudoradians* (30.95 Ma), which roughly coincide in depth with the normal event (see Table T5 and “Biostratigraphy,” p. 8). The lower event coincides with the top of nanofossil datum *E. formosa* (32.9 Ma) at 85.52–86.47 mcd, and this normal event is assigned to Chron C13n (33.058–33.545 Ma).

In the interval from ~100 to 200 mcd (Fig. F27B), a few tentative chron assignments are made where the data appear to be better resolved, but little confidence is placed in these. In the interval from ~200 to 300 mcd (Fig. F27C), the inclination record appears to be biased toward negative values (normal polarity) with positive (reversed polarity) spikes within 1–2 m of core tops. Based on the biostratigraphy, this interval corresponds to the lower to middle Eocene, where several long reversed polarity intervals should be represented. The bias cannot result from an insufficiently removed drilling overprint, which would be in the opposite direction. The bias may be an artifact of soft-sediment deformation, and no attempt to interpret the record in this interval was made. Below 320 mcd, most of the record comes from XCB cores that are significantly disturbed, and again, no polarity interpretations were made.

Other Studies

At this site, a preliminary study of demagnetization fractions of the vertical components was attempted. Detailed analysis and evaluation of ~15,000 data points from Hole 1263A suggests that

1. Downward vertical components associated with a drilling overprint may be useful as an indicator of deformation during drilling and/or splitting.
2. The coercivity fraction between 10 and 15 mT may be useful as an indication of magnetic contamination.
3. Frequent or sudden large changes of NRM intensity may contribute to spurious signals in inclination and intensity data, as observed by Parker and Gee (2002).

GEOCHEMISTRY

Volatile Hydrocarbons

A total of 34 headspace samples from Site 1263 (all from Hole 1263A) were analyzed (Table T11). The concentration of CH₄ (C₁) in most of the samples was at an atmospheric background level (range = 1.6–2.0 µL/L [ppmv]) and did not exceed 3 ppmv in any sample. No hydrocarbon gases higher than C₁ were detected.

T11. Composition of headspace gases, p. 81.

Interstitial Water Chemistry

Interstitial waters from 30 samples were collected at Site 1263: 26 from Hole 1263A (10.2–378.2 mcd) and 4 from Hole 1263B (281.3–313.4 mcd). The samples from the two holes were taken to constitute a single depth profile using the composite depth scale. Slight differences in lithology may cause minor breaks in the concentration-depth gradients of some chemical parameters. Chemical constituents were determined according to the procedures outlined in “Geochemistry,” p. 23, in the “Explanatory Notes” chapter. Results of the chemical analyses are presented in Table T12.

pH, Salinity, Alkalinity, Chloride, and Sodium

The pH of pore waters at Site 1263 ranges from 7.29 to 7.70, although this maximum value appears to be anomalous. Excluding the 7.70 maximum, the average pH of Site 1263 interstitial waters is 7.44 ± 0.07 (Table T12). All values are lower than the average seawater value of 8.1, and there is no distinct depth trend. Salinity typically ranges from 34.0 to 35.5 g/kg (mean = 34.8 ± 0.4 g/kg).

Alkalinity is relatively constant with depth and, ignoring a suspiciously high value of 5.93 mM at 55.0 mcd and an anomalously low value of 2.09 mM at 97.5 mcd, the average value is 3.05 ± 0.21 mM (Fig. F28A). Apart from the anomalously low value, all interstitial water samples have a higher alkalinity than average seawater (2.33 mM; International Association of Physical Sciences of the Ocean [IAPSO] certified value).

Chloride concentrations are generally constant with depth (average = 559 ± 18 mM) with the exception of a low value of 476 mM, which occurs at a depth of 77.4 mcd (Fig. F28B). The sodium profile does not exhibit any significant downhole trend, with concentrations between 463 and 486 mM (Fig. F28C).

Potassium, Calcium, Magnesium, Strontium, and Lithium

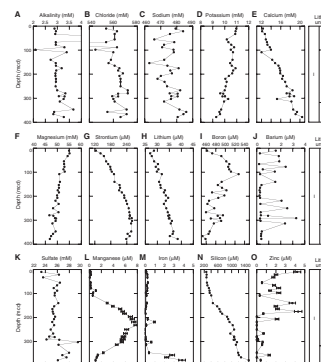
Site 1263 downhole trends in potassium, calcium, and magnesium are consistent with those resulting from exchange with basaltic basement at depth (Gieskes, 1981), with potassium and magnesium decreasing and calcium increasing slightly with depth (Fig. F28D, F28E, F28F). Calcium values increase from 12.3 mM (10.2 mcd) to 20.5 mM (378.2 mcd) (Fig. F28E). The shallowest Site 1263 interstitial water calcium value of 12.3 mM is higher than that from Site 1262 (8.49 mM at 4.45 mcd) and the mean seawater value of 10.6 mM (IAPSO certified value). The calcium concentration of the deepest (231 mcd) sample from Site 1262 of 17.6 mM is similar to that from the equivalent depth (231.8 mcd) at Site 1263 of 16.9 mM.

The magnesium pore water profile (Fig. F28F) from Site 1263 is characterized by a general decrease with depth, from 54.9 mM in the shallowest sample (10.2 mcd) to 46.9 mM at the base of the section (378.2 mcd). Pore water potassium concentrations decrease slightly with depth from 11.0 mM (10.2 mcd) to 9.30 mM (378.2 mcd) (Fig. F28D).

Strontium concentrations increase downhole from 125 μ M in the shallowest sample (10.2 mcd) to peak at values >250 μ M for ~70 m (279.5–347.1 mcd) (Fig. F28G). Below 347.1 mcd, strontium values appear to decrease slightly; but with only three samples below this depth, no real assessment of trends can be made. The strontium pore water

T12. Interstitial water analyses, p. 82.

F28. Chemical constituents in interstitial waters, p. 58.



profile indicates a source of strontium to the interstitial waters between 279.5 and 347.1 mcd and diffusion of this strontium into the sediments above. This input of strontium is most likely from the dissolution and recrystallization of carbonates (e.g., Baker et al., 1982).

Lithium concentrations increase gradually from 28.6 μM in the shallowest sample (10.2 mcd) to 38.4 μM toward the base of the section (378.2 mcd) (Fig. F28H). A very similar lithium pore water profile was observed at Site 1262. The increase with depth suggests a source of lithium from the sediment to the pore waters.

Boron and Barium

Pore water boron concentrations increase from 462 to 528 μM over the depth interval from 10.2 to 108.4 mcd (Fig. F28I) then decrease downhole to a value of 458 μM at the bottom of the section (378.2 mcd). Laboratory experiments under controlled temperatures and pressures have shown that boron is leached from terrigenous sediments into fluids (e.g., James et al., 2003), and a study of Leg 186 interstitial water samples concluded that the removal of boron from clays and volcanic ash was responsible for boron enrichment in the pore waters (Deyhle and Kopf, 2002). Therefore, the pore water boron peak at 108.4 mcd could indicate either increased concentrations of terrigenous sediment or the enhanced dissolution of terrigenous components in this interval. Barium values fluctuate between ~ 0.3 and 3.29 μM downhole, with zones of consistently low barium concentrations occurring from 153.7 to 207.0 mcd and below 347.1 mcd (Fig. F28J).

Sulfate, Manganese, and Iron

The sulfate pore water profile at Site 1263 is characterized by relative stability at values between 25 and 26 mM from 55.0 to 292.6 mcd. The uppermost samples (10.2–32.5 mcd) exhibit more variability and lower values, whereas samples from below 292.6 mcd display greater variability and generally higher values (Fig. F28K). Below 313.4 mcd XCB drilling was used, and it is possible that the increased sulfate values from this depth and below were caused by increased seawater contamination associated with the XCB technique, although none of the other chemical profiles exhibit such a shift toward seawater values. Overall, the sulfate concentrations at Site 1263 (average = 25.73 ± 1.18 mM) are higher than those recorded at Site 1262 (average = 22.54 ± 0.65 mM), which suggests the sediments at Site 1263 contain even less organic matter than those recovered at Site 1262 (see “Carbonate and Organic Carbon,” p. 20, in “Sediment Geochemistry”).

The Site 1263 manganese pore water profile exhibits a large, broad peak extending from 108.4 to 347.1 mcd, climaxing at 231 mcd with a concentration of 7.82 μM (Fig. F28L). The mean concentration above and below this interval is 0.60 ± 0.47 μM . The maximum concentration of manganese in seawater is 3.6 nM (Burton, 1996). Pore water concentrations of dissolved Fe are typically low and invariant throughout the upper 300 m of the section (Fig. F28M). Below 347.1 mcd, iron concentrations increase dramatically to 3.83 μM at 378.2 mcd. The broad peak in pore water manganese concentrations and the subsequent increase in iron below the manganese peak suggest elevated reduction associated with enhanced anaerobic microbial activity (e.g., Malone et al., 2002). Under conditions where reducible iron oxides and manganese oxides are limited, continuing anaerobic microbial activity would shift to re-

duction of sulfate, and lower sulfate concentrations and increased alkalinity would be expected (e.g., Gieskes, 1981). However, both sulfate and alkalinity pore water profiles are relatively constant through the section, suggesting the large manganese peak and increase in iron may not be associated with anaerobic microbial activity. Instead, it is possible that the manganese and iron pore water enrichments at Site 1263 are the result of inorganic sedimentary diagenesis, which requires further investigation.

Silicon and Zinc

Dissolved silicon in pore fluids from Site 1263 increases slightly from 262 μM at a depth of 10.2 mcd to 454 μM at 140.0 mcd. Below 140.0 mcd, the silicon concentrations increase more rapidly downhole and peak at 1498 μM at the bottom of the hole (378.2 mcd). The maximum concentration of dissolved silicon measured in the pore waters of Site 1263 sediments is almost three times the maximum observed at Site 1262 and during the study of Leg 74 interstitial waters (Gieskes et al., 1984). Ash layers have been observed in the sediments from Site 1263 below ~185 mcd and substantial chert deposits were recovered below ~225 mcd, but it seems that these minor siliceous lithologies do not occur in sufficient volume to account for the high silicon concentrations in the pore waters.

Zinc concentrations from Site 1263 pore waters varied between 4.32 and 0 μM (below detection limits) in the upper section (10.2–207.0 mcd). Below 207.0 mcd, the zinc concentrations of the interstitial waters were consistently low and often below the detection limits (F280).

Summary of Interstitial Water Chemistry

Although the calcium, potassium, and magnesium interstitial water profiles at Site 1263 suggest that a simple diffusion profile between seawater and basement basalt is responsible for the chemistry of the pore waters, other elements including strontium, lithium, manganese, iron, and silicon indicate that diagenetic processes occurring in the sediments also have a strong impact on the interstitial water chemistry. Further geochemical study of the sediments (shipboard by sediment dissolution inductively coupled plasma–atomic emission spectroscopy) is required to understand the nature of the diagenesis of Site 1263 sediments.

Sediment Geochemistry

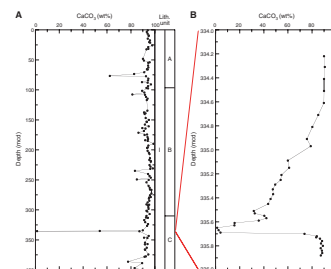
Carbonate and Organic Carbon

Carbonate determinations by coulometry were made for a total of 163 samples from Site 1263 (Table T13). The values for carbonate are generally high (mean = 85.5 wt%) but range from 1.33 to 98.96 wt% (Table T13; Fig. F29). High-resolution (every 2 to 10 cm) samples were analyzed for carbonate content across the P/E boundary section from Hole 1263C (Fig. F29B) and show a drastic drop from ~85 to 1.33 wt% within <10 cm (mcd) of sediment at the initiation of the P/E event. Above 335.64 mcd, the carbonate values recover to ~40 wt% over a few centimeters before slowly returning to >80 wt% by 334.6 mcd.

Elemental analysis of total carbon indicates low (0.86–0.00 wt%; mean = 0.09 wt%) concentrations of organic carbon in Site 1263 sedi-

T13. Sedimentary calcium carbonate and total and organic carbon, p. 83.

F29. Sedimentary carbonate contents, p. 59.



ments (Table T13), although no samples from the carbonate-barren P/E boundary sediments were analyzed.

Extractable Hydrocarbons

Extraction of organic matter was attempted on several sample residues after squeezing interstitial water. Analyzable amounts of extracts were obtained from 40 g of carbonate-rich Samples 208-1263A-17H-5, 145–150 cm (175.2 mcd), and 36X-2, 140–150 cm (357.0 mcd).

The aliphatic hydrocarbon fractions of the samples are dominated by C₁₂–C₂₂ iso- and anteiso-alkanes. It is notable that C₁₇–C₁₉ *n*-alkanes of algal origin are not major components in Sample 208-1263A-17H-5, 145–150 cm. Long chain alkanes, namely C₂₉, C₃₁, and C₃₃, were detected in Sample 208-1263A-36X-2, 140–150 cm, indicating a contribution of organic matter from higher terrestrial plants.

DOWNHOLE MEASUREMENTS

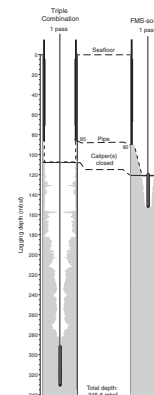
Logging Operations

Three logging runs including the triple combo tool string configuration, FMS-sonic tool string configuration, and vertical seismic profiling using the three-component Well Seismic Tool (WST-3) (see Fig. F6, p. 51, in the “Explanatory Notes” chapter) were planned for Hole 1263A. After completion of the APC and XCB drilling operation (bit size = 9⁷/₈ in) at 345.6 mbsf, the hole was displaced with 120 bbl of 8.9-lb/gal sepiolite mud and the bit was withdrawn to 85 mbsf in preparation for logging. A summary of the logging operation is provided in Figure F30, and a breakdown of the chronology is provided in Table T14, including some details of the tools used. The tool rig-up began at 0230 hr on 1 April and was completed by 0030 hr on 2 April after a blockage at 174 mbsf during the first FMS-sonic run and the identification of a progressive hole collapse prevented further tool penetration. The WST-3 run was canceled.

The triple combo tool string configuration with the Lamont-Doherty Earth Observatory high-resolution Multi-Sensor Gamma Ray Tool (MGT) on top and the Temperature/Acceleration/Pressure (TAP) tool on bottom was run to the bottom of the hole (3075 mbrf; 345 mbsf), and logging began at 0700 hr on April 1. The lockable flapper valve was not latched open, and the tool string reentered the pipe only after pumping water through the pipe for some time. Because of this problem, the tool string was run out of the hole to the rig floor at 1000 hr and the MGT run was cancelled. The caliper readings from the triple combo tool string suggested that the upper section of the hole was enlarged to 18 in (i.e., wider than the maximal caliper extension). Inspection of the tool at the end of the run revealed that the caliper was broken and that the hole condition might have been better than it appeared. The tool sustained no serious damage.

The FMS-sonic tool string was rigged up, and the first run was blocked just outside the pipe. A wiper trip was run and the tool string was run into the hole again, reaching a new blockage at 174 mbsf. Logs were taken from that point. The caliper readings from the FMS-sonic tool string suggested that the hole (at least the upper section) was slowly collapsing (some intervals <8.5 in). The FMS-sonic tool string was retrieved from the rig floor, and logging operations were completed

F30. Logging operations, p. 60.



T14. Logging operations, Hole 1263A, p. 85.

by 0030 hr on 2 April. The heave conditions were excellent, typically <1 m throughout the logging operation. Consequently, the wireline heave compensator experienced no problems during this operation.

Data Quality

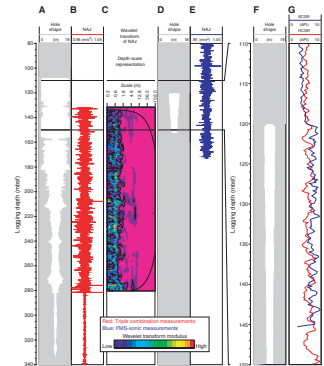
The triple combo caliper indicated that the hole conditions were very good in the lower 60 m of the borehole (XCB drilling). Above this interval, the hole shape is characterized by washouts that increase up-hole (Fig. F31A). Apparently, the worst section of the hole logged with the caliper is between 118 (caliper closed) and 127 mbsf, where the hole diameter is >18 in (and the caliper was probably broken). A hole diameter of this magnitude normally would degrade the quality of the data acquired with tools that require contact with the borehole wall (e.g., the density or porosity tools). However, little evidence of deterioration of data quality exists uphole in these logs (Fig. F32).

Tool string accelerometer data from the TAP tool, which integrates the effects of heave, sidewall contact, and wireline stretch on the tool string, indicate that hole conditions and stick-slip of the tool remained at low levels until the cable head entered the BHA (Fig. F31B). As a further check, a wavelet analysis of these accelerometer data was undertaken. The wavelet transform (WT) analysis of the acceleration data allows the multiscale components of the tool acceleration to be deciphered (Fig. F31C). The analyzed record (133–277 mbsf) is characterized by acceleration/deceleration, mainly over a range <1 m. Major washouts are characterized by localized stick-slip displacement over intervals of intermediate scale (~4–7 m). The high-frequency component could be explained by incomplete heave compensation; the other components are related to hole condition (size of the washout). The comparison of the wavelet representation and hole shape shows that the intervals where tool acceleration changes correspond to changes in hole diameter (Fig. F31A, F31C).

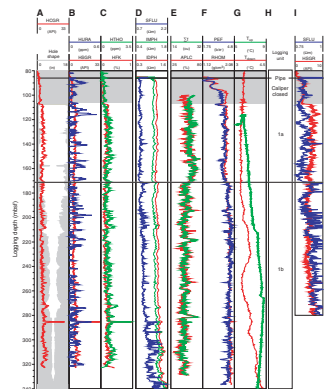
The FMS-sonic caliper readings clearly show a much smaller hole than the triple combo caliper readings showed 12 hr earlier. These observations suggest that damage sustained by the triple combo caliper arm in the open hole may have caused an overestimation of the recorded hole size or, alternatively, showed the progressive collapse of the hole, resulting in the blockage of the tool string at 174 mbsf (Fig. F31D). As for the triple combo tool string, acceleration of the FMS-sonic tool string remained at low levels (Fig. F31E).

The original logs were depth-shifted to the seafloor (–2727 m). The seafloor depth was based on the step in the Hostile Environment Natural Gamma Ray Sonde (HNGS) gamma radiation logs (triple combo tool string). The seafloor depth determined in this manner differs by 1.2 m from the seafloor depth determined from the mudline. Because of the lack of clear correlatable features between the computed gamma radiation logs of the triple combo HNGS tool and the FMS-sonic Scintillation Gamma Ray (SGT) tool, particularly given the short section where FMS-sonic calipers were open (Fig. F31F), no unambiguous depth match between the runs with the two tool strings could be established (Fig. F31G). Therefore, the same depth shift to the seafloor (–2727 m) was applied to the FMS-sonic logs.

F31. Quality of triple combo and FMS-sonic logs, p. 61.



F32. Downhole logging stratigraphy, triple combo tool string, p. 62.



Logging Stratigraphy

The logged section is characterized by very subtle variations around very low mean values. For example, total gamma radiation does not exceed 33 API and is mostly below 10 API. As total radioactivity is low, the absolute abundance of each contributing element (uranium, thorium, and potassium) is also low (Fig. F32A, F32B, F32C). The resistivities (spherically focused resistivity [SFLU], medium-induction phasor-processed resistivity [IMPH], and deep-induction phasor-processed resistivity [IDPH]) are commonly plotted on a logarithmic scale because of the typically wide range of these values over several orders of magnitude. Here, resistivities are between 0.3 and 2.2 Ωm and are plotted on a linear scale (Fig. F32D). Highest variabilities are recorded in porosity (APLC) and density (RHOM) logs (Fig. F32E, F32F) and their associated parameters, namely the formation capture cross section (Σ_f) and the photoelectric factor (PEF). In the upper part of the logged section (base of pipe to 170 mbsf), the porosity is >57% and the density <1.9 g/cm³. Below 170 mbsf, the porosity decreases to ~50% with a concomitant increase in density to ~2.0 g/cm³.

Based on (1) the homogeneity of the formation and (2) the previous general description of the formation, one logging unit containing two subunits has been defined. These subunits are differentiated by the density, porosity, and resistivity logs (Fig. F32).

Logging Subunit 1a

Depth: base of pipe (85 mbsf)–170 mbsf

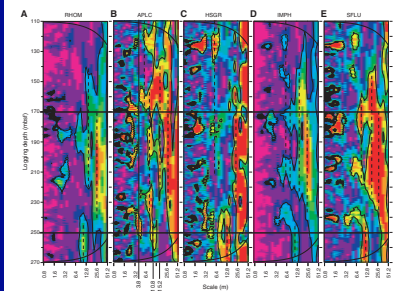
Logging Subunit 1a is characterized by low density (<1.9 g/cm³), high porosity (>55%), and low shallow resistivity (SFLU) values (~0.8 Ωm) (Figs. F32, F33). Logging Subunit 1a partly correlates with lithostratigraphic Subunit IB, containing nannofossil ooze, clay-bearing nannofossil ooze, and chalky nannofossil ooze (see “Subunit IB,” p. 7, in “Unit I” in “Description of Lithostratigraphic Units” in “Lithostratigraphy”). The noticeable drop in the gamma counts and density/porosity values and their associated parameters, as well as in the resistivity values at ~106 mbsf, may not correspond to a lithologic change but instead reflects the lack of environmental correction of these logs, as the caliper was closed at this depth.

Logging Subunit 1b

Depth: 170 mbsf to the bottom of the hole (345.7 mbsf)

The upper boundary of logging Subunit 1b is defined by a rapid change in the density and porosity logs (Figs. F32, F33), corresponding to similar changes in logging bulk density and density data from the cores (see “Physical Properties,” p. 11, in the “Explanatory Notes” chapter and “Lithostratigraphy,” p. 5). The gamma ray counts for this subunit show a major peak at 286 mbsf and a minor one at 273 mbsf. Intermediate (IMPH) and deep (IDPH) resistivities fluctuate little through this subunit but show a very subtle increase downhole. The PEF of logging Subunit 1b is slightly higher than that for logging Subunit 1a above (Fig. F32F), suggesting a change in mineralogy in this interval. This logging subunit correlates with the bottom part of lithostrati-

F33. Wavelet transform of logs, p. 63.



graphic Subunit IB, containing nannofossil ooze, clay-bearing nannofossil ooze, and chalky nannofossil ooze, and lithostratigraphic Subunit IC, containing nannofossil ooze and chalky nannofossil ooze (see “Subunit IB,” p. 7, and “Subunit IC,” p. 8, both in “Unit I” in “Description of Lithostratigraphic Units” in “Lithostratigraphy”).

Over the logged portion of the hole, all logs display pervasive cyclicity at a number of depth scales (Fig. F33). The density (RHOM) shows stronger variations at longer wavelengths (cycles are ~30, 15, and 10 m) than porosity (APLC), with which it is anticorrelated (Fig. F33). Porosity (APLC) and total gamma radiation (HSGR) logs both show cyclicity down to the submeter scale (Fig. F33). Intermediate (IMPH) and shallow (SFLU) resistivity cycles are similar to density cycles but with greater detail. The changes in the spatial distribution of these localized cycles conform with and thus reinforce the previously defined unit subdivision (note the change in the pattern of the WT representation, particularly density [RHOM] at ~170 mbsf).

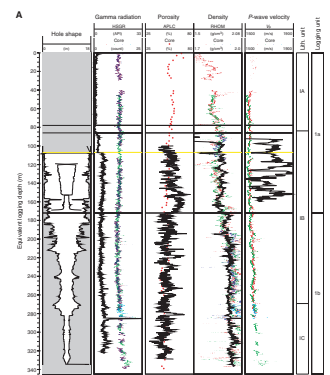
Discussion

Comparison between continuous and in situ logs with the whole-core MST records (gamma radiation, density, and velocity) and discrete sample moisture (porosity) and density (MAD) data provides the basis for depth matching the core-derived composite depth (mcd) scale to the logging depth and thus creating a logging equivalent depth—a necessary step to correct for the expansion of the cores and obtain correct sedimentation and mass accumulation rates (see “Age Model and Mass Accumulation Rates,” p. 33, in the “Explanatory Notes” chapter). The total gamma counts, porosity, density, and velocity, as well as the core recovery, lithostratigraphy, lithologic subunit division, MS, and color reflectance data, have been linearly compressed on the depth axis by 18%, the core-derived composite depth growth rate (see “Composite Depth,” p. 4). These data are presented at this compressed equivalent logging depth scale in Figure F34. On this scale, core and logging data are in relatively good agreement with regard to depth: within 1 m at 288 mbsf and a few meters below (e.g., compare the gamma ray data in Fig. F34A). However, the match between gamma radiation, porosity, and density is better in logging Subunit 1b than in logging Subunit 1a (especially porosity), indicating the need for a slightly different compression ratio for the cores in these subunits.

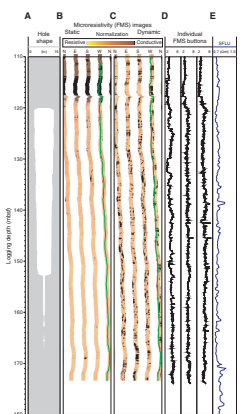
Given the data, only the microresistivity (FMS-sonic) images with a vertical resolution of ~5 cm can theoretically resolve higher-frequency cycles seen, for example, in color reflectance data. In the section logged with the FMS-sonic tool string (110–173 mbsf) (Fig. F35A), the static normalized microresistivity image shows an increase in resistivity downhole (Fig. F35B) and the dynamically normalized image (window height = 0.5 m) does not display a clear pattern of lithification (Fig. F35C). Combined factors such as (1) the homogeneity of the formation, (2) its low resistivity values, and (3) the weak coverage of the borehole wall by the FMS-sonic tool string limit the use of the FMS images for further cyclostratigraphic studies.

As a preliminary step in the comparison between logging and core properties, Figure F36 shows the relationship between density vs. sonic velocity measured on the cores (Fig. F36A), downhole density vs. core density (Fig. F36B), and downhole density vs. sonic velocity in cores (Fig. F36C), with all data relative to the equivalent logging depth. Except for the lower part of the hole (equivalent logging depth > 320

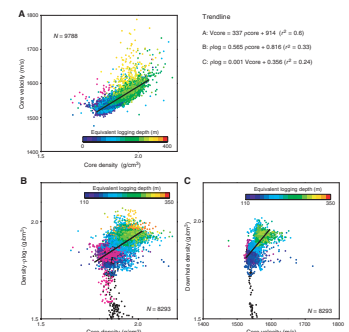
F34. Core-log integration, p. 64.



F35. FMS images and cyclostratigraphic limitations, p. 66.



F36. Seismic modeling inputs, p. 67.



mbsf), the core velocity increases as core density increases with depth. Below 320 mbsf, the linear coefficient between the two parameters increases. Where logging data are corrected for environmental effects (caliper is open; below 115 mbsf; blue to red dots), a linear relationship between core and logging densities exists.

AGE MODEL AND MASS ACCUMULATION RATES

A 400.7-mcd-thick (340.1 mbsf) upper Paleocene (~58 Ma) to Pleistocene pelagic sediment sequence was recovered at Site 1263. Sixty-two biostratigraphic and six magnetostratigraphic datums were selected to construct an age-depth model for this site (Table T15; Fig. F37). Linear sedimentation rates (LSRs), total mass accumulation rates (MARs), and carbonate MARs were calculated at 1-m.y. intervals (Table T16) (see “Age Model and Mass Accumulation Rates,” p. 33, in the “Explanatory Notes” chapter).

Age-Depth Model

The main objective of Site 1263 was to recover a complete and well-resolved upper Paleocene to lower Eocene section, and the site was chosen to yield this critical stratigraphic interval at a relatively shallow burial depth. The sediment section at Site 1263 is therefore characterized by a significant condensed interval comprising a major unconformity in the upper Oligocene to upper Miocene section (28–5 Ma; 49–29 mcd). Biostratigraphic and magnetic reversal data are in general agreement for the upper Paleocene to lower Oligocene section, and the age model is based on all datum types. The Pliocene–Pleistocene age model is roughly constrained by planktonic foraminifers only (Fig. F37). The most significant discrepancies between nannofossil and planktonic foraminiferal datums exist in the partly condensed middle Eocene to lower Oligocene interval, where reworking is common.

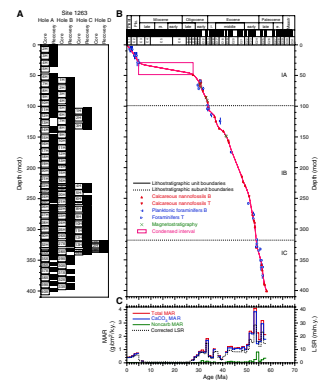
Linear Sedimentation and Mass Accumulation Rates

LSRs range between <1 and 29 m/m.y., and total MARs range from <0.1 to 4.1 g/cm²/k.y. Total MAR fluctuations essentially represent variations in carbonate MAR. LSRs and carbonate MARs were highest from 58 to 51 Ma (late Paleocene to early Eocene) and relatively constant from 51 to 43 Ma (middle Eocene). The rates dropped in the late Eocene to very low values and formed a moderate peak in the early Oligocene (34–29 Ma). The magnitude of the extremely low LSRs and MARs cannot be determined for the upper Oligocene to upper Miocene. The Pliocene–Pleistocene rates are generally low to moderate.

Noncarbonate MARs averaged over 1-m.y. intervals are generally low (<0.2 g/cm²/k.y.) throughout the section, and the small fluctuations may be within the analytical uncertainty. The moderately high noncarbonate value of 0.8 g/cm²/k.y. in the interval of 54–55 Ma is related to the presence of the carbonate-poor intervals of a few centimeters to several decimeters thickness (see “Lithostratigraphy,” p. 5, and “Geochemistry,” p. 17). These short-term carbonate dissolution events are smoothed out in the MAR record as a result of our 1-m.y. sampling of the age-depth model, dictated by the limited resolution of the shipboard age-depth control points and density and carbonate data.

T15. Datum levels, p. 86.

F37. Age-depth model, p. 68.



T16. Age-depth model, LSRs, and MARs, p. 87.

REFERENCES

- Baker, P.A., Gieskes, J.M., and Elderfield, H., 1982. Diagenesis of carbonates in deep-sea sediments—evidence from Sr²⁺/Ca²⁺ ratios and interstitial dissolved Sr²⁺ data. *J. Sediment. Petrol.*, 52:71–82.
- Burton, J.D., 1996. The ocean: a global geochemical system. In Summerhayes, C.P., and Thorpe, S.A. (Eds.), *Oceanography: An Illustrated Guide*: London (Manson Publishing Ltd.), 166.
- Cande, S.C., and Kent, D.V., 1995. Revised calibration of the geomagnetic polarity timescale for the Late Cretaceous and Cenozoic. *J. Geophys. Res.*, 100:6093–6095.
- Clark, M.W., and Wright, R.C., 1984. Paleogene abyssal foraminifers from the Cape and Angola basins, South Atlantic Ocean: DSDP 73. In Hsü, K.J., LaBrecque, J.L., et al., *Init. Repts. DSDP, 73*: Washington (U.S. Govt. Printing Office), 459–480.
- Deyhle, A., and Kopf, A., 2002. Strong B-enrichment and anomalous boron isotope geochemistry in the Japan forearc. *Mar. Geol.*, 183:1–15.
- Gieskes, J.M., 1981. Deep-sea drilling interstitial water studies: implications for chemical alteration of the oceanic crust, layers I and II. In Warme, J.E., Douglas, R.G., and Winterer, E.L. (Eds.), *The Deep Sea Drilling Project: A Decade of Progress*. Spec. Publ.—Soc. Econ. Paleontol. Mineral., 32:149–167.
- Gieskes, J.M., Johnston, K., and Boehm, M., 1984. Interstitial water studies, Leg 74. In Moore, T.C., Rabinowitz, P.D., et al., *Init. Repts. DSDP, 74*: Washington (U.S. Govt. Printing Office), 701–711.
- James, R.H., Allen, D.E., and Seyfried, W.E., Jr., 2003. An experimental study of alteration of oceanic crust and terrigenous sediments at moderate temperatures (51 to 350°C): insights as to chemical processes in near-shore ridge-flank hydrothermal systems. *Geochim. Cosmochim. Acta*, 67:681–691.
- Lourens, L.J., Hilgen, F.J., Laskar, J., Shackleton, N.J., and Wilson, D., in press. The Neogene period. In Gradstein, F.M., Ogg, J., and Smith, A.G. (Eds.), *A Geological Time Scale 2004*: Cambridge (Cambridge Univ. Press).
- Malone, M.J., Claypool, G., Martin, J.B., and Dickens, G.R., 2002. Variable methane fluxes in shallow marine systems over geologic time: the composition of pore waters and authigenic carbonates on the New Jersey shelf. *Mar. Geol.*, 189:175–196.
- Moore, T.C., Jr., Rabinowitz, P.D., et al., 1984. *Init. Repts. DSDP, 74*: Washington, D.C. (U.S. Govt. Printing Office).
- Müller-Merz, E., and Oberhänsli, H., 1991. Eocene bathyal and abyssal benthic foraminifera from a South Atlantic transect at 20–30° S. *Palaeogeogr., Palaeoclimatol., Palaeoecol.*, 83:117–171.
- Olafsson, G., and Villa, G., 1992. Reliability of sphenoliths as zonal markers in Oligocene sediments from the Atlantic and Indian Oceans. In Proto Decima, F., Monechi, S., and Rio, D. (Eds.), *Proc. Int. Nanoplankton Assoc. Conf., Firenze 1989*. Mem. Sci. Geol., 43:261–275.
- Parker, R.L., and Gee, J.S., 2002. Calibration of the pass-through magnetometer—II. Application. *Geophys. J. Int.*, 150:140–152.
- Schmiedl, G., Mackensen, A., and Müller, P.J., 1997. Recent benthic foraminifera from the eastern South Atlantic Ocean: dependence on food supply and water masses. *Mar. Micropaleontol.*, 32:259–287.
- Thomas, E., and Shackleton, N., 1996. The Palaeocene–Eocene benthic foraminiferal extinction and stable isotope anomalies. In Knox, R.W.O'B., Corfield, R.M., and Dunay, R.E. (Eds.), *Correlation of the Early Paleogene in Northwest Europe*. Geol. Soc. Spec. Publ., 101:401–441.
- Tjalsma, R.C., 1983. Eocene to Miocene benthic foraminifers from DSDP Site 516, Rio Grande Rise, South Atlantic. In Barker, P.F., Carlson, R.L., Johnson, D.A., et al., *Init. Repts. DSDP, 72*: Washington (U.S. Govt. Printing Office), 731–756.

Figure F2. Site 1264 on line GeoB 01-031 (Part 1) with the location of crossing line GeoB 01-046 along which Site 1263 is located. Also shown are the locations of proposed Sites WALV-8B, WALV-8C, and Deep Sea Drilling Project (DSDP) Site 525. GI = generated injection. w.d. = water depth. PETM = Paleocene/Eocene Thermal Maximum. K = Cretaceous.

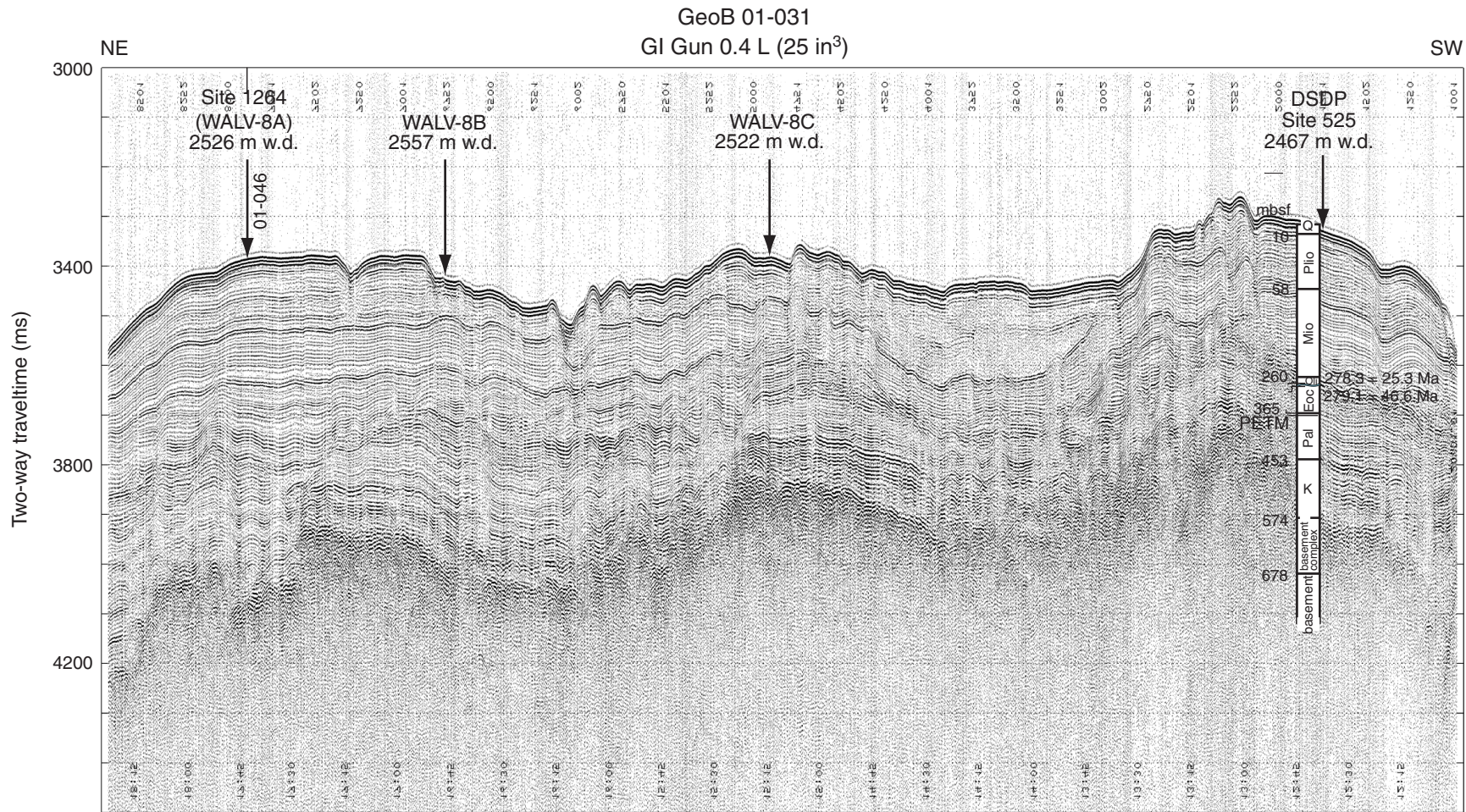


Figure F3. Line GeoB 01-046 and Sites 1263 and 1264 plotted with age estimates of prominent reflectors. R_1 is a regional reflector associated with an erosional unconformity. Using an average velocity of 1.8 m/ms, the Paleocene/Eocene boundary reflector ($R_{P/E}$) is estimated to be at ~276 mbsf and the Cretaceous/Paleogene boundary reflector ($R_{K/P}$) at ~352 mbsf. $R_{O/M}$ = Oligocene/Miocene boundary reflector. CDP = common depth point. V.E. = vertical exaggeration.

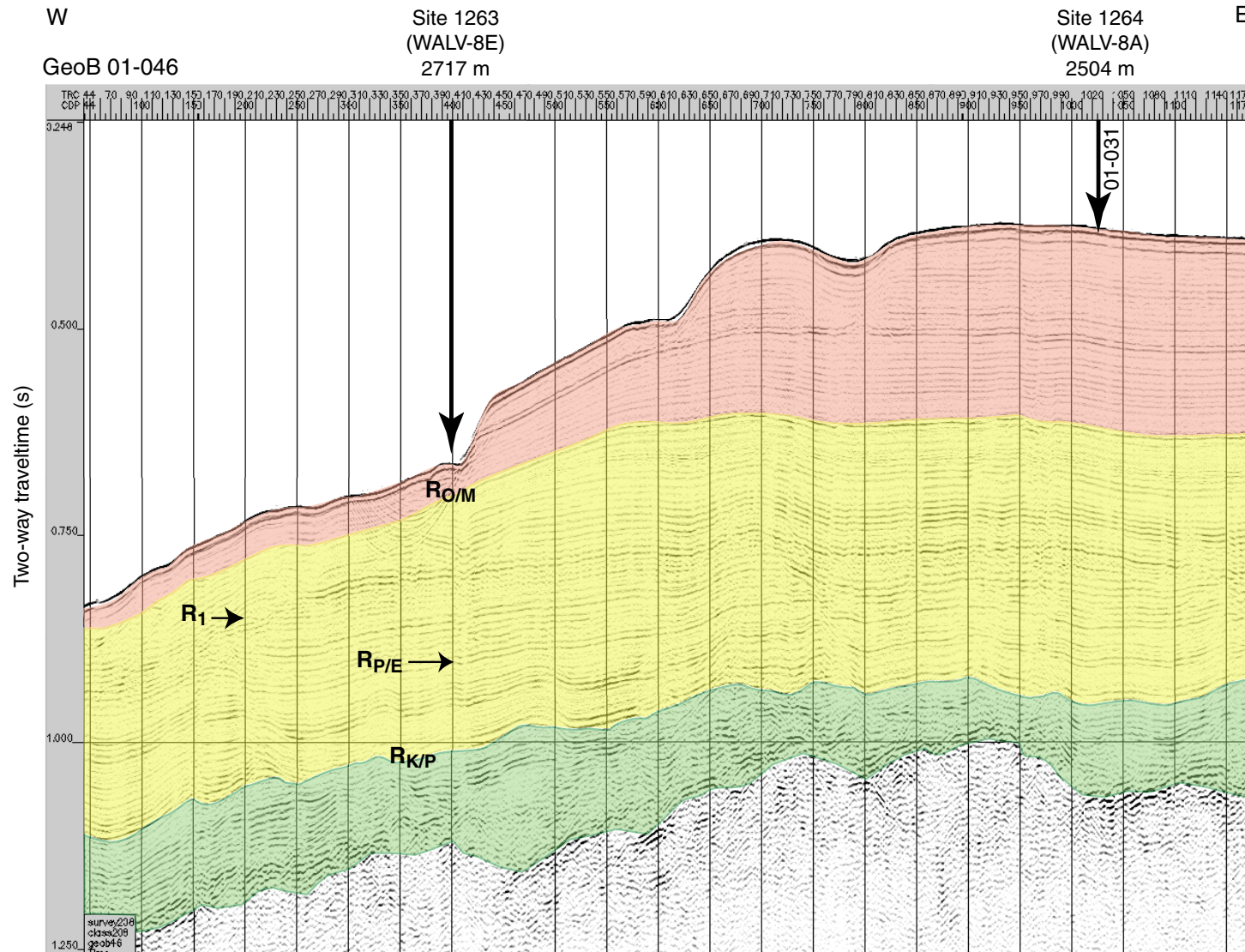


Figure F4. Magnetic susceptibility data from 0 to 400 mcd of Site 1263. Data from Holes 1263A, 1263B, 1263C, and 1263D are offset from the spliced record by 10, 100, 1000, and 10000, respectively. Magnetic susceptibility values lower than 2 were multiplied by 0.5 and incremented by 1. Numbers near the tops of the individual core records are the core numbers. * = data from the top of the core is missing or removed because of coring disturbance.

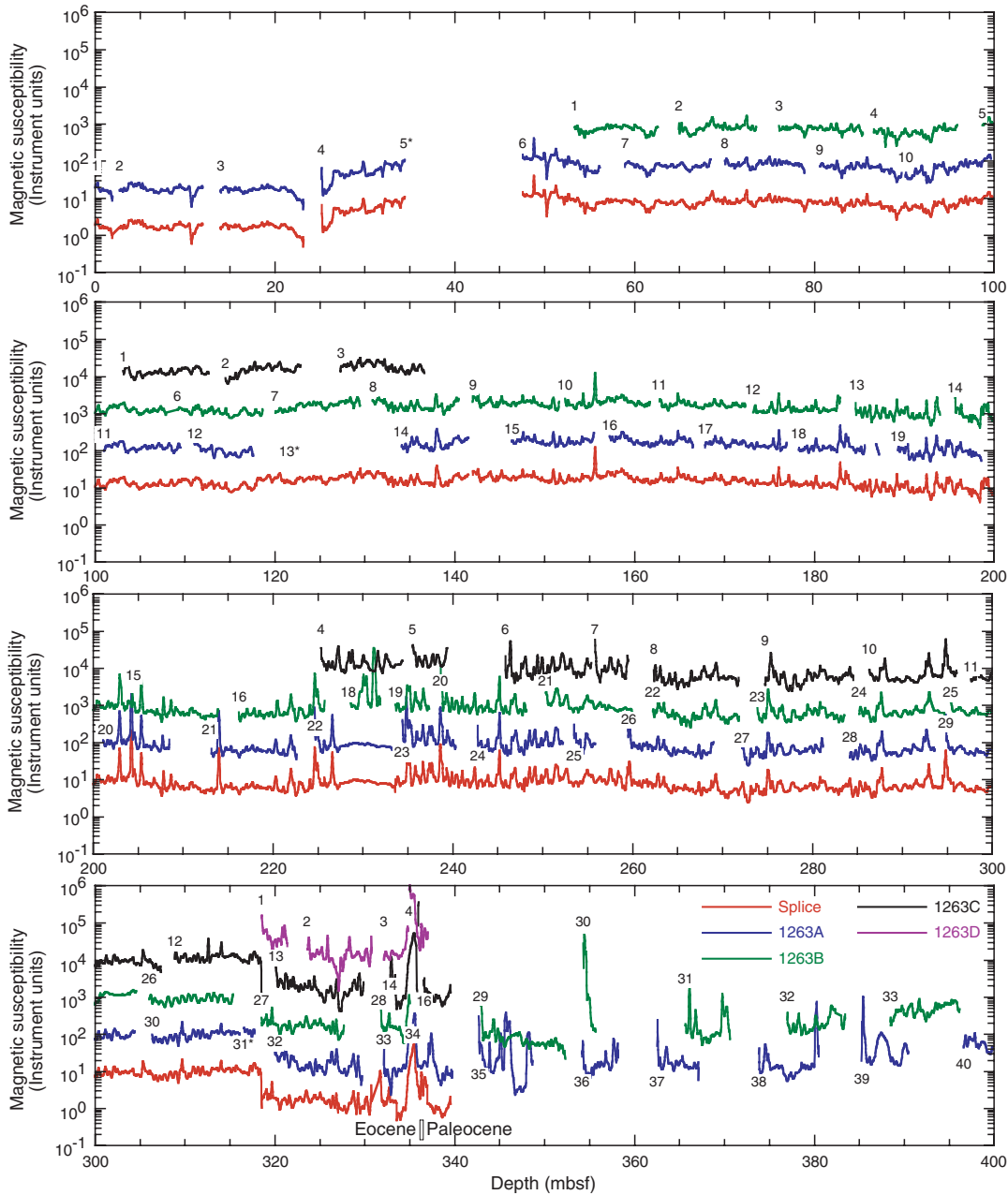


Figure F5. Magnetic susceptibility data for the P/E boundary intervals in the Site 1263 splice and in the individual holes (1263A, 1263B, 1263C, and 1263D). Note that the base of the P/E boundary in Hole 1263A is probably not complete and that the magnetic susceptibility data of Hole 1263D was contaminated by small pieces of chert during the coring process.

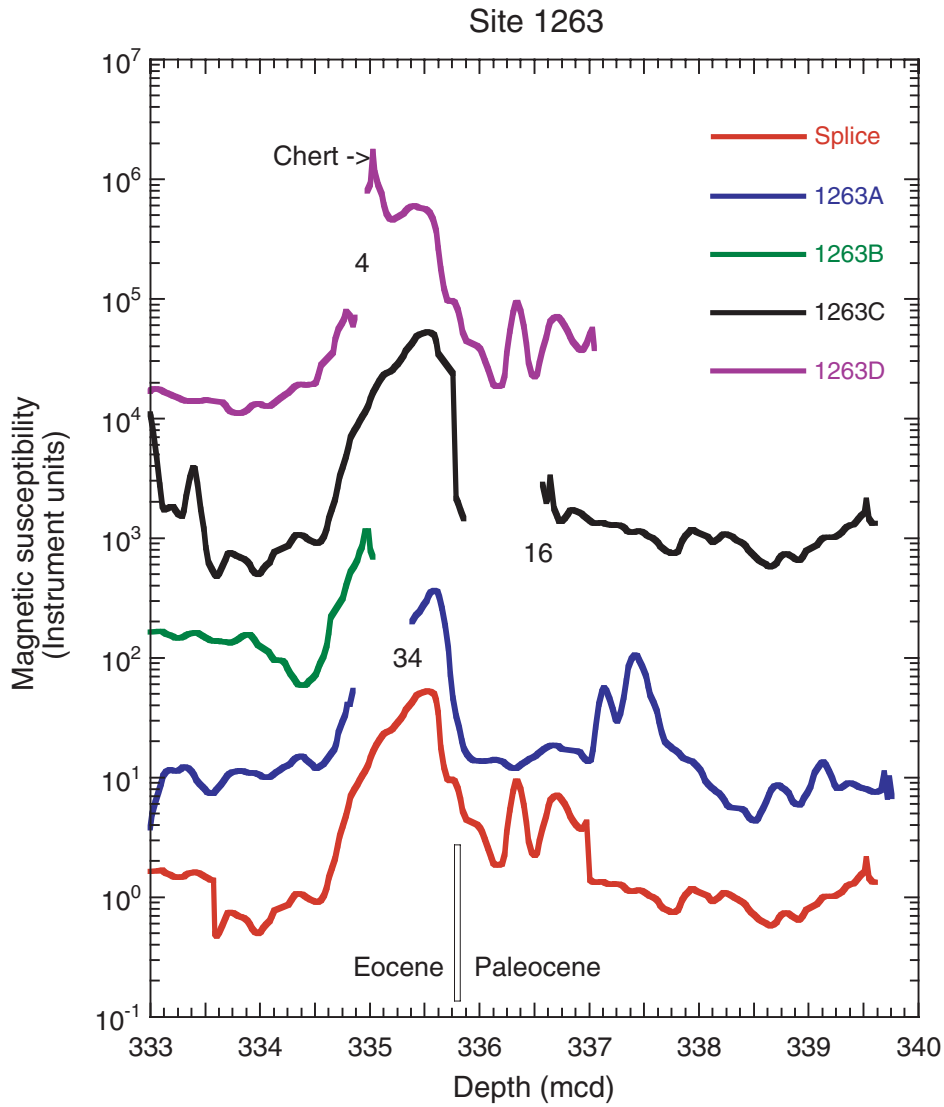


Figure F6. Differential stretching of cores recovered by APC (Core 208-1263A-30H) and XCB (Core 208-1263B-26X) drilling techniques.

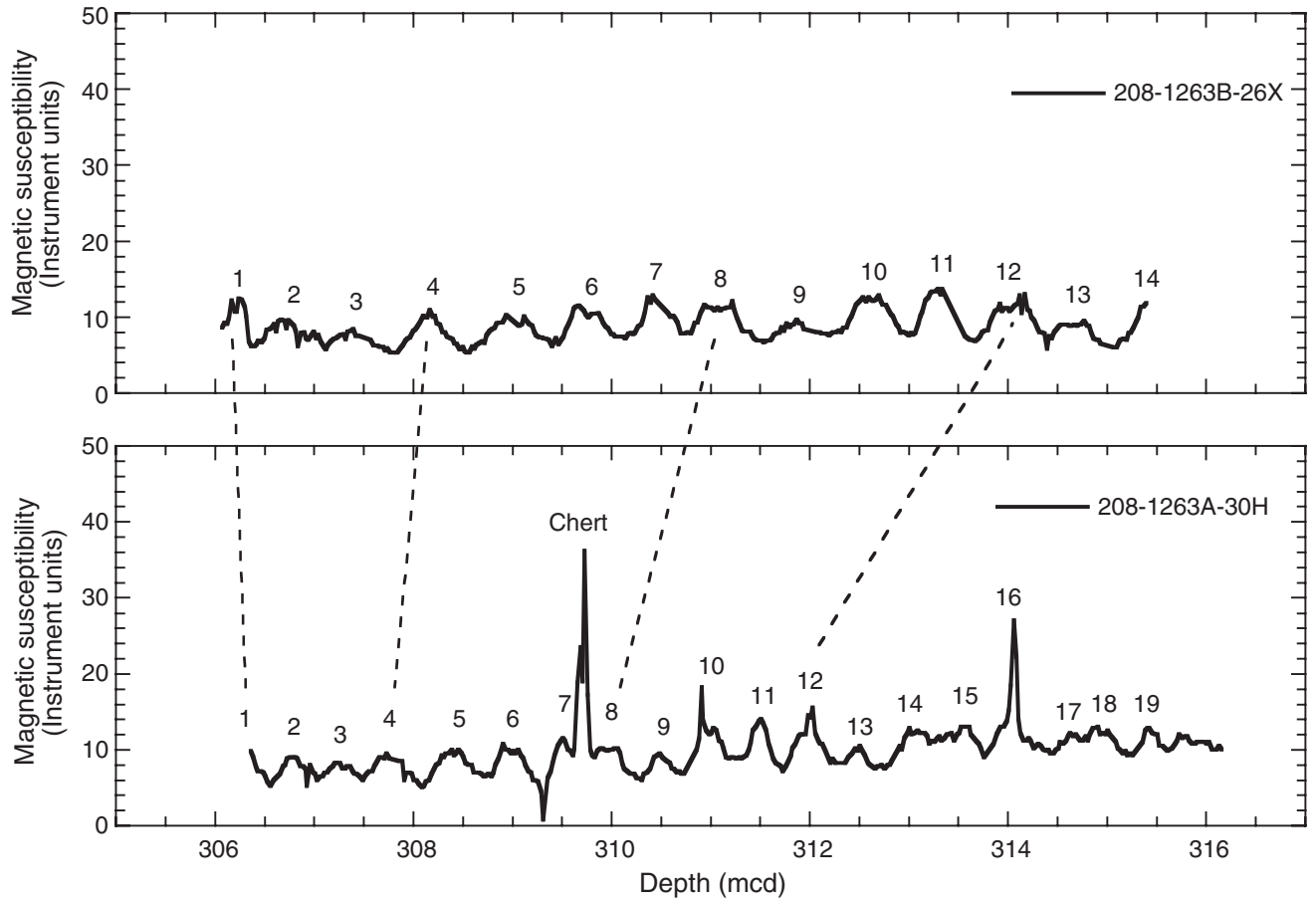


Figure F7. Mbsf vs. mcd growth rates for Holes 1263A, 1263B, and 1263C.

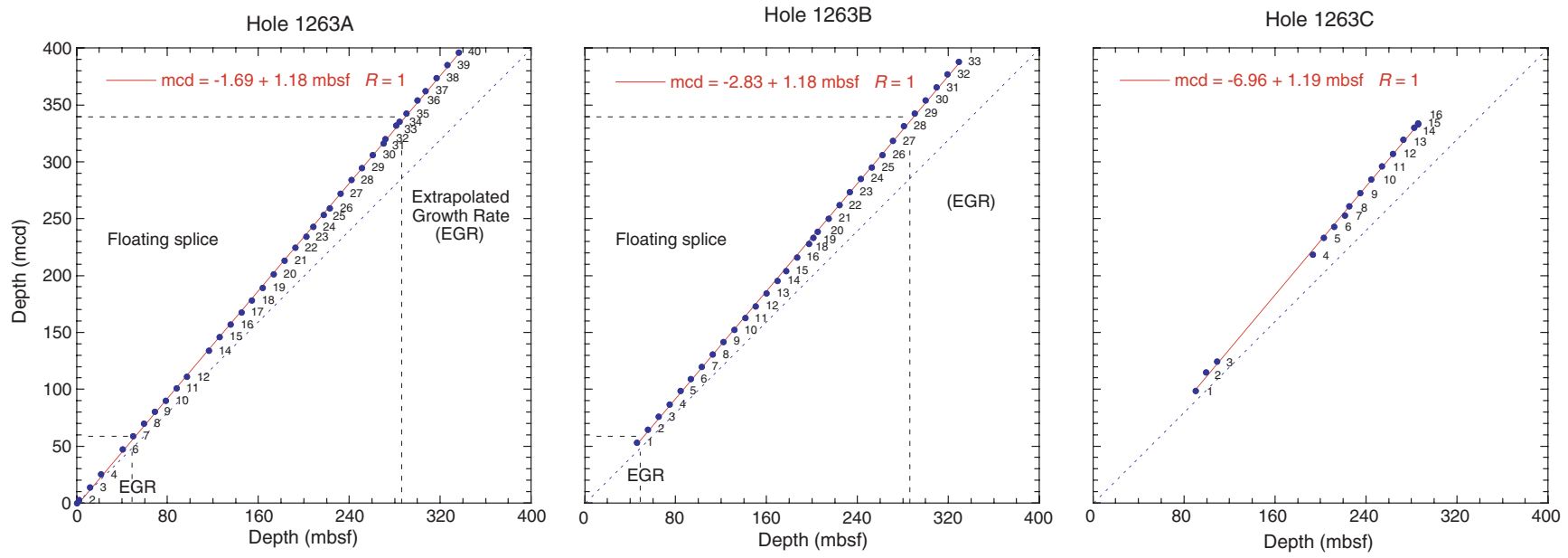


Figure F8. Site 1263 lithostratigraphic composite illustrating stratigraphic variation in parameters used to define lithostratigraphic units. Foraminifer percentages (triangles) are smoothed with a 3-point moving average (line). Natural gamma radiation (NGR) values are smoothed with a 5-point moving average. L* = sediment lightness, MS = magnetic susceptibility.

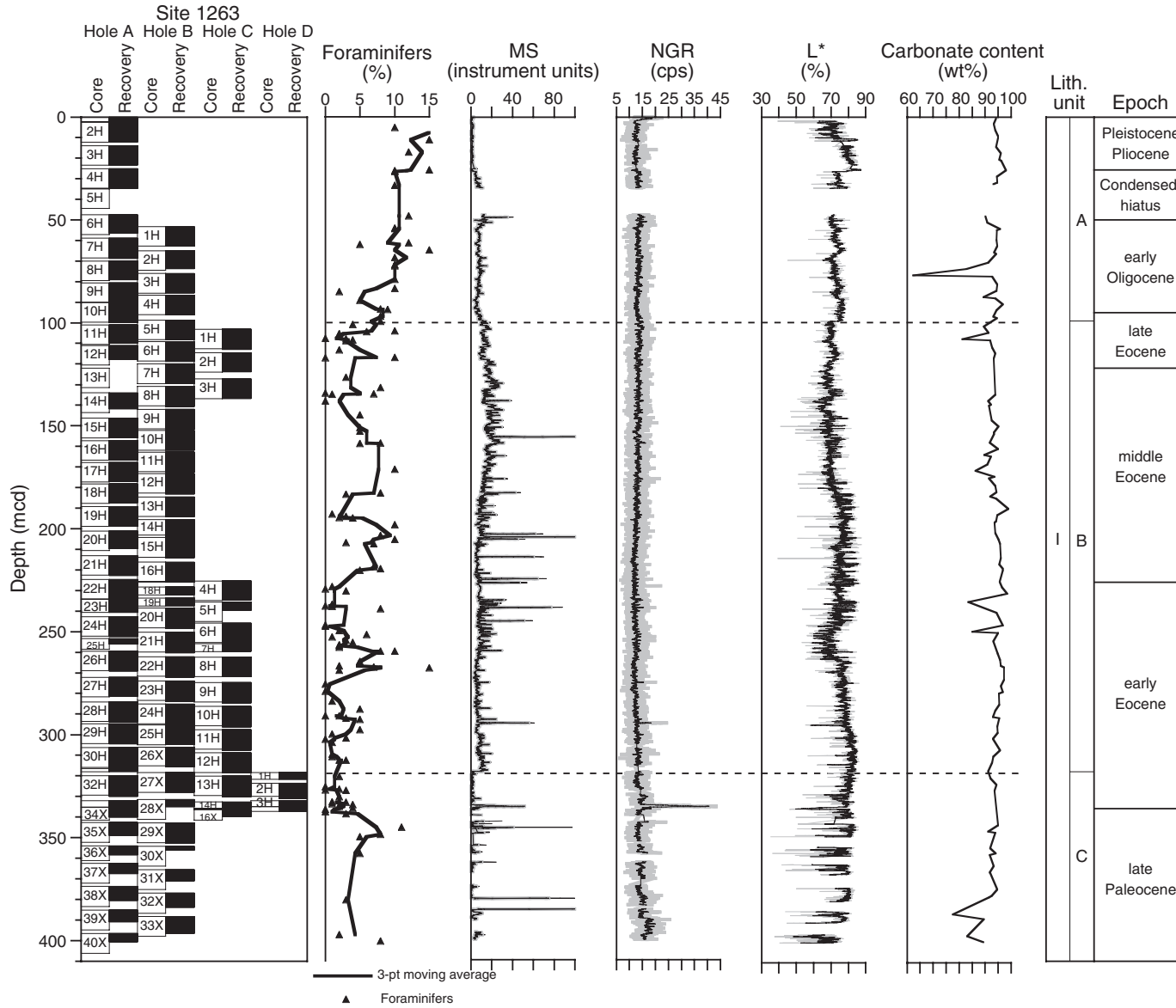


Figure F9. Site 1263 lithostratigraphic composite illustrating stratigraphic variation in whole-core multi-sensor track measurements of magnetic susceptibility (MS), gamma ray attenuation (GRA) bulk density, natural gamma radiation (NGR), and *P*-wave velocity logger (PWL) values. GRA data are smoothed with a 10-point moving average; all other data are smoothed with a 5-point moving average.

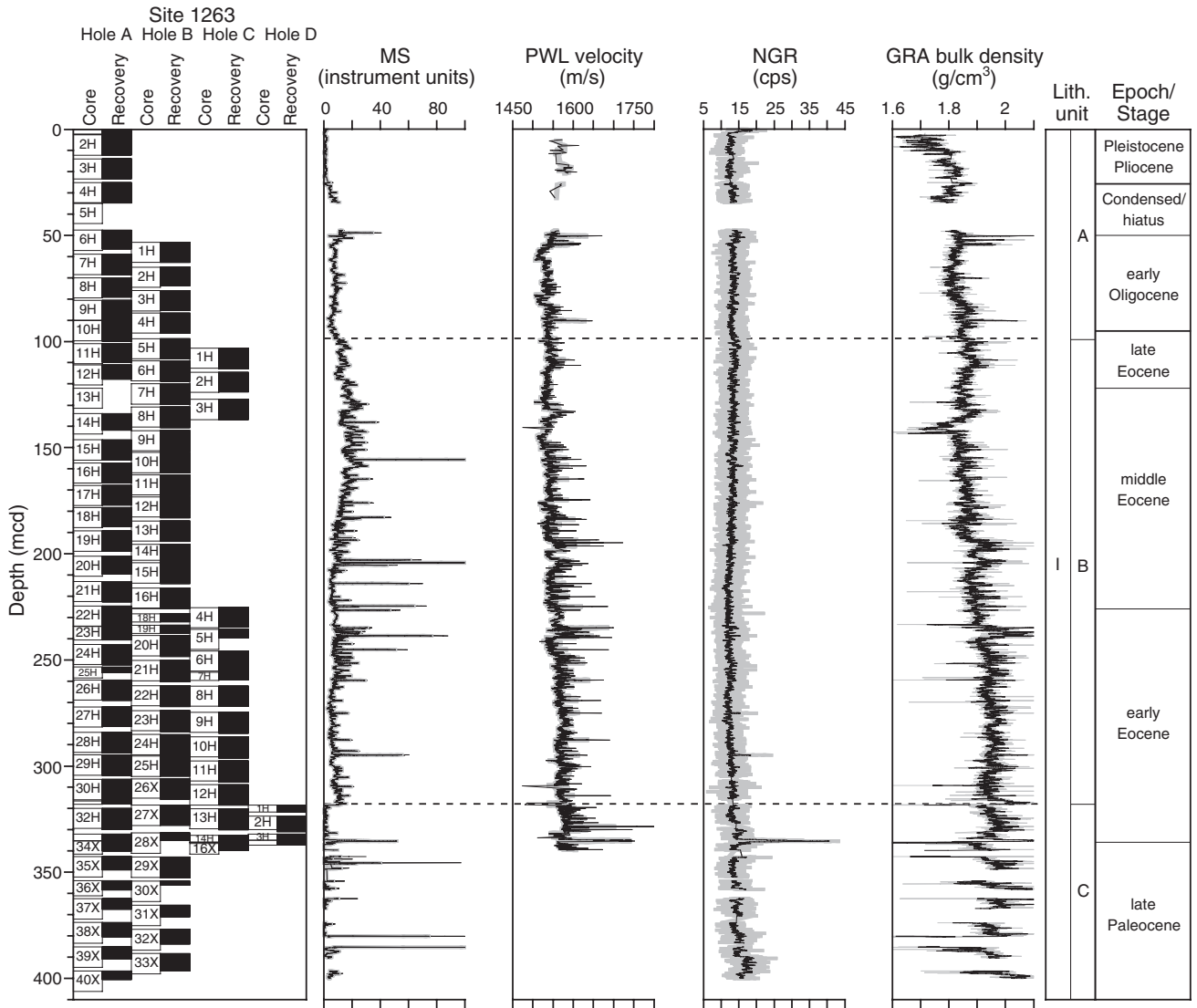


Figure F10. Site 1263 lithostratigraphic composite illustrating stratigraphic variation in lightness (L^*), carbonate content, and chromaticity (a^* and b^*). Color data smoothed with a 5-point moving average.

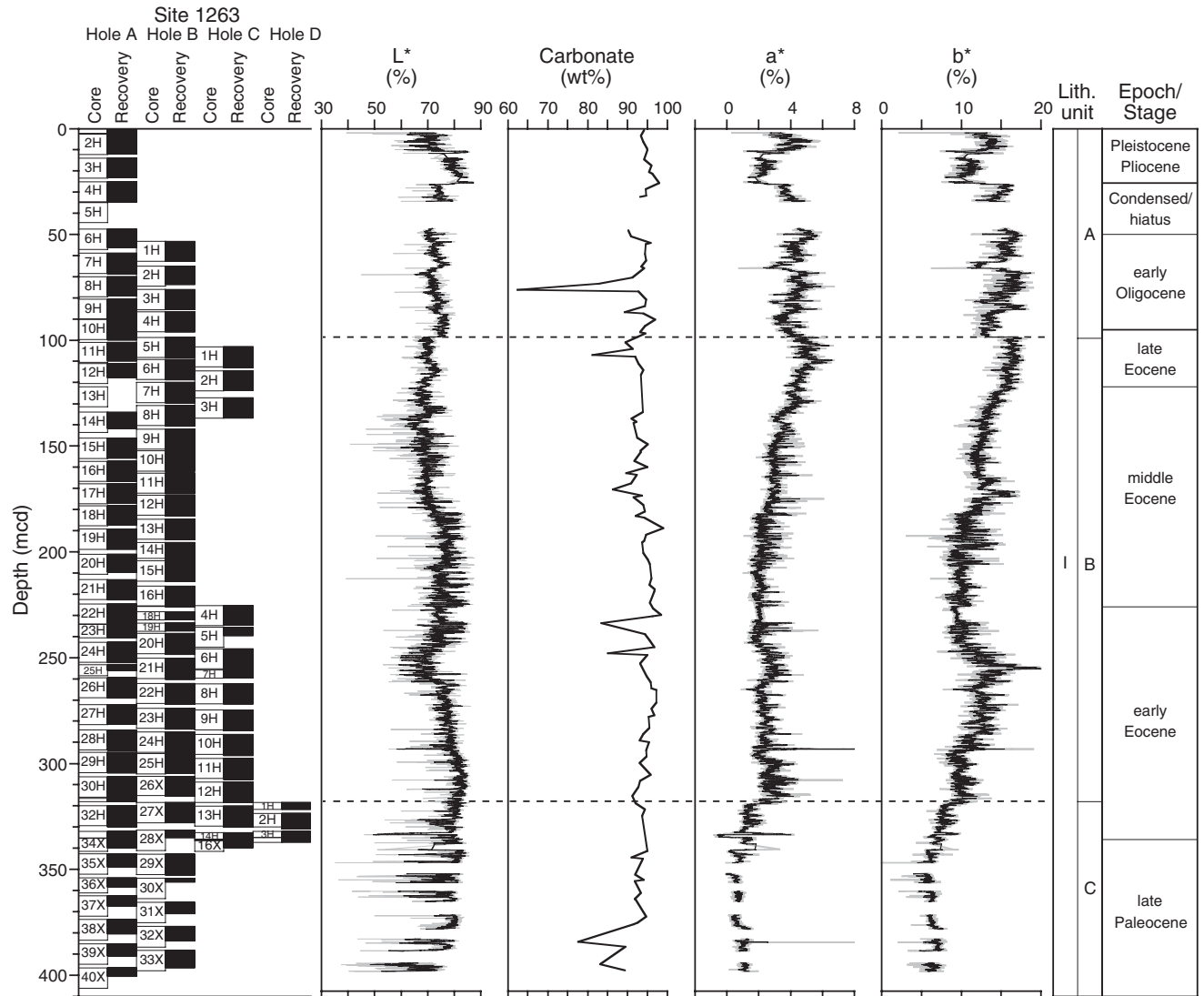


Figure F11. Site 1263 (single points) lithostratigraphic composite illustrating stratigraphic variation in predominant and accessory smear slide components, smoothed with a 3-point moving average (solid lines). Major lithologies are also shown.

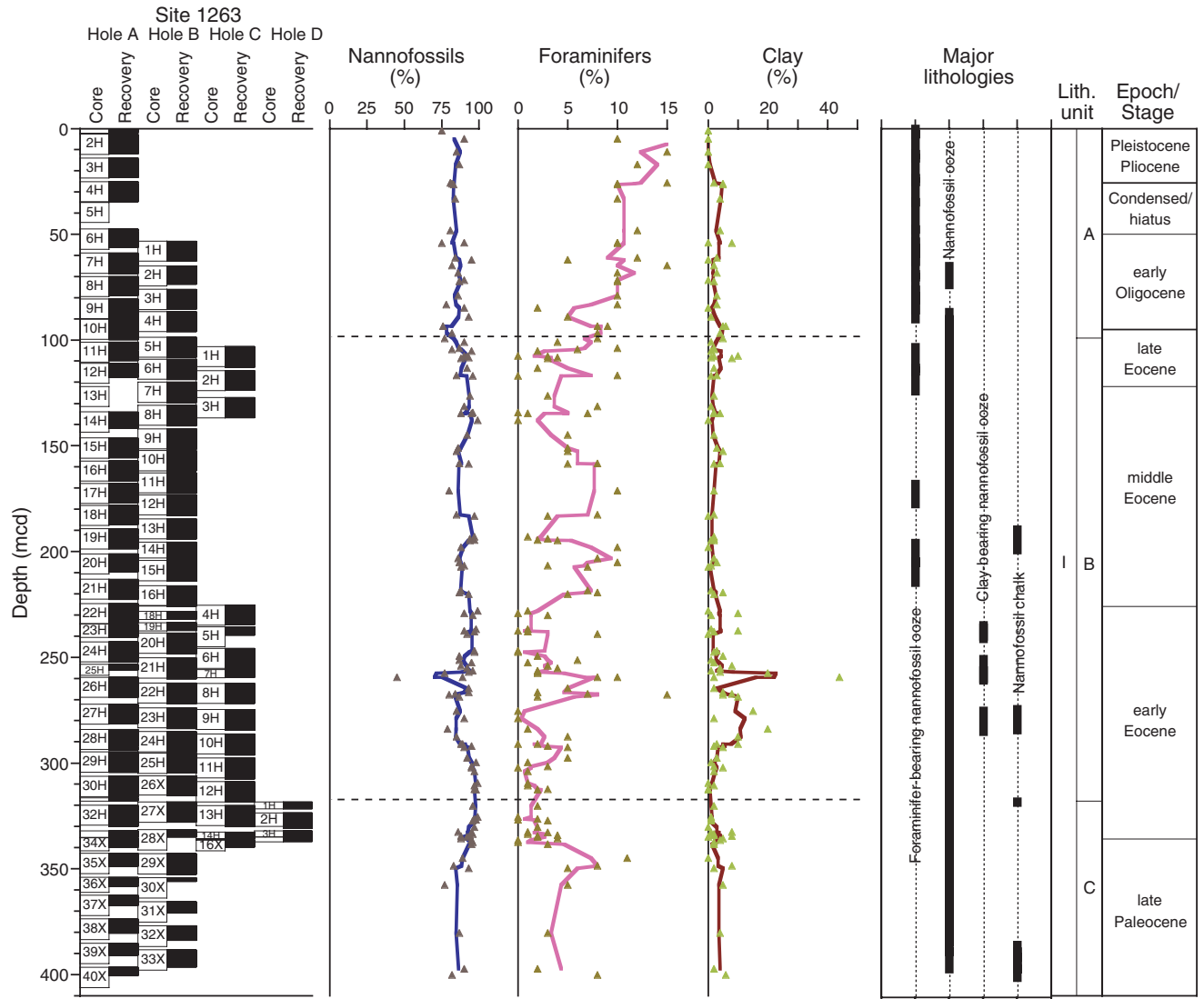


Figure F12. Site 1263 lithostratigraphic composite illustrating stratigraphic variation in physical properties of grain density (GD), bulk density (BD; MAD method), porosity, and *P*-wave velocity sensor (PWS3) measurements.

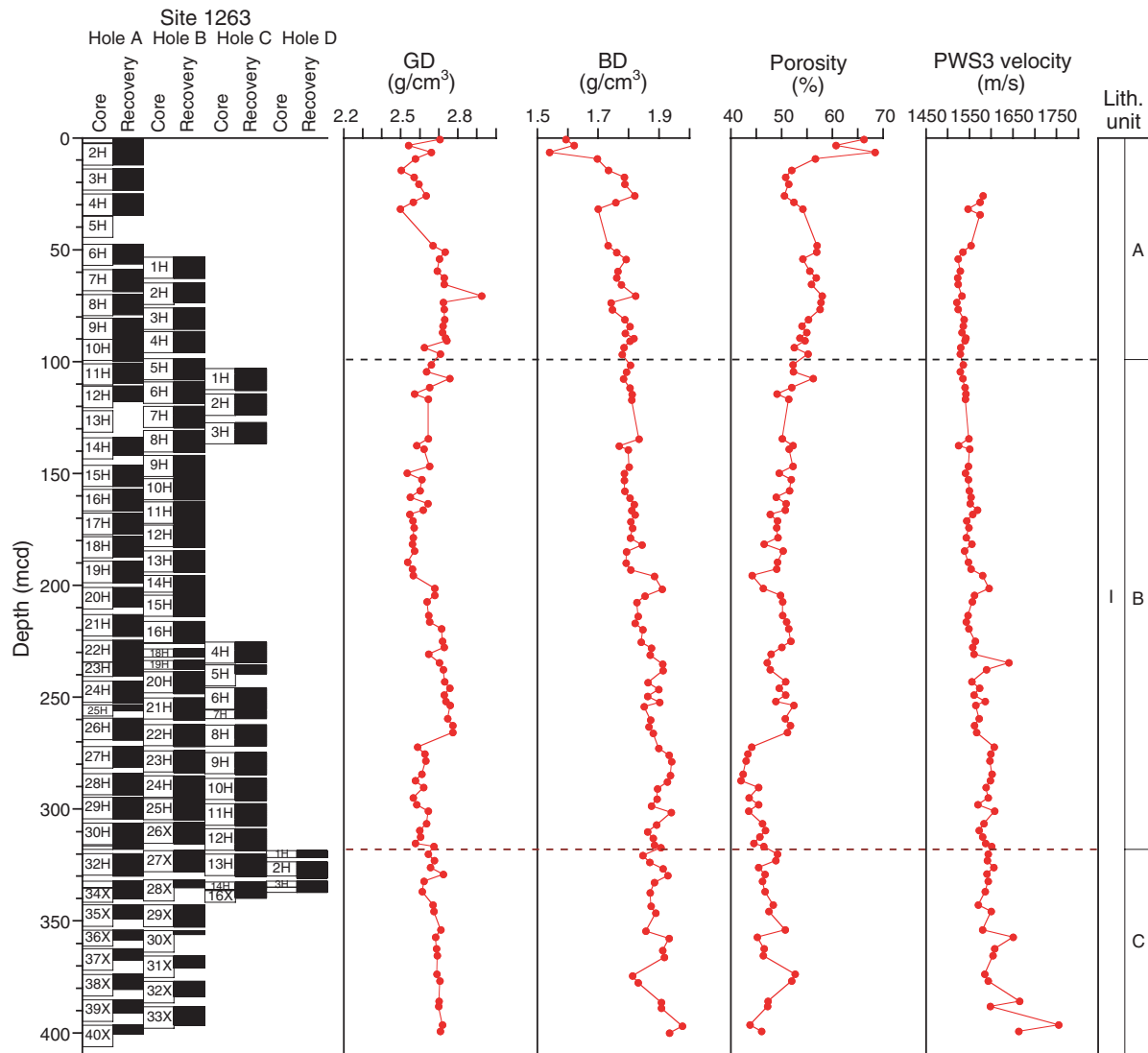


Figure F13. A, B. Comparison between bulk density measured by gamma ray attenuation (GRA, small dots) and the moisture and density (MAD [large dots]) methods. C. Correlation of grain density (GD) vs. bulk density (BD; MAD method). D. Correlation of porosity vs. BD (MAD method). E. Correlation of *P*-wave velocity sensor (PWS3) and BD (MAD method) measurements.

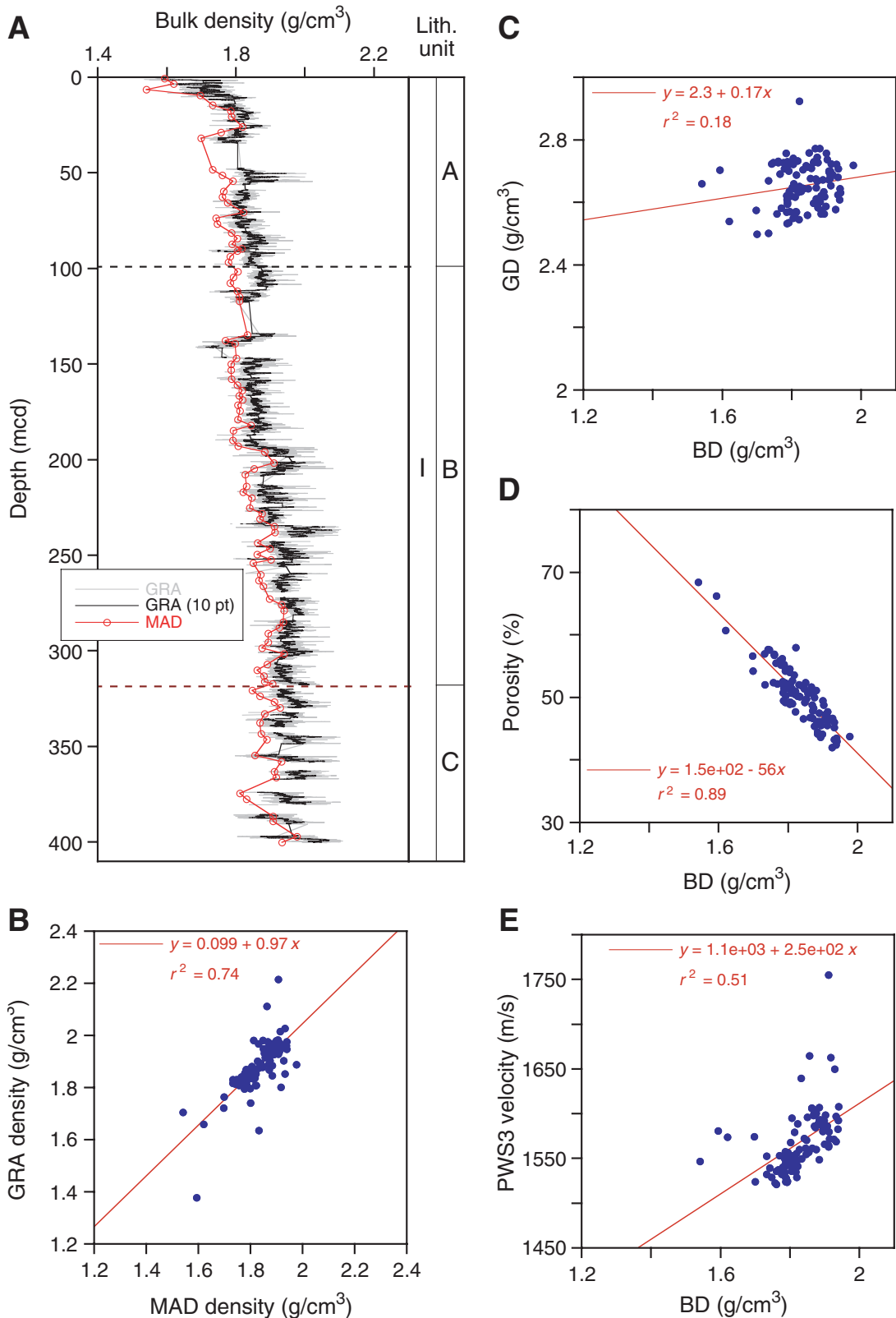


Figure F14. A. Comparison of *P*-wave velocities measured on the whole-core multisensor track *P*-wave logger (PWL) and the split core *P*-wave transducer (PWS3). B. Close-up of measured velocities (line = PWL, solid circles = PWS3) at the P/E boundary. C. Scatterplot of PWL vs. PWS3.

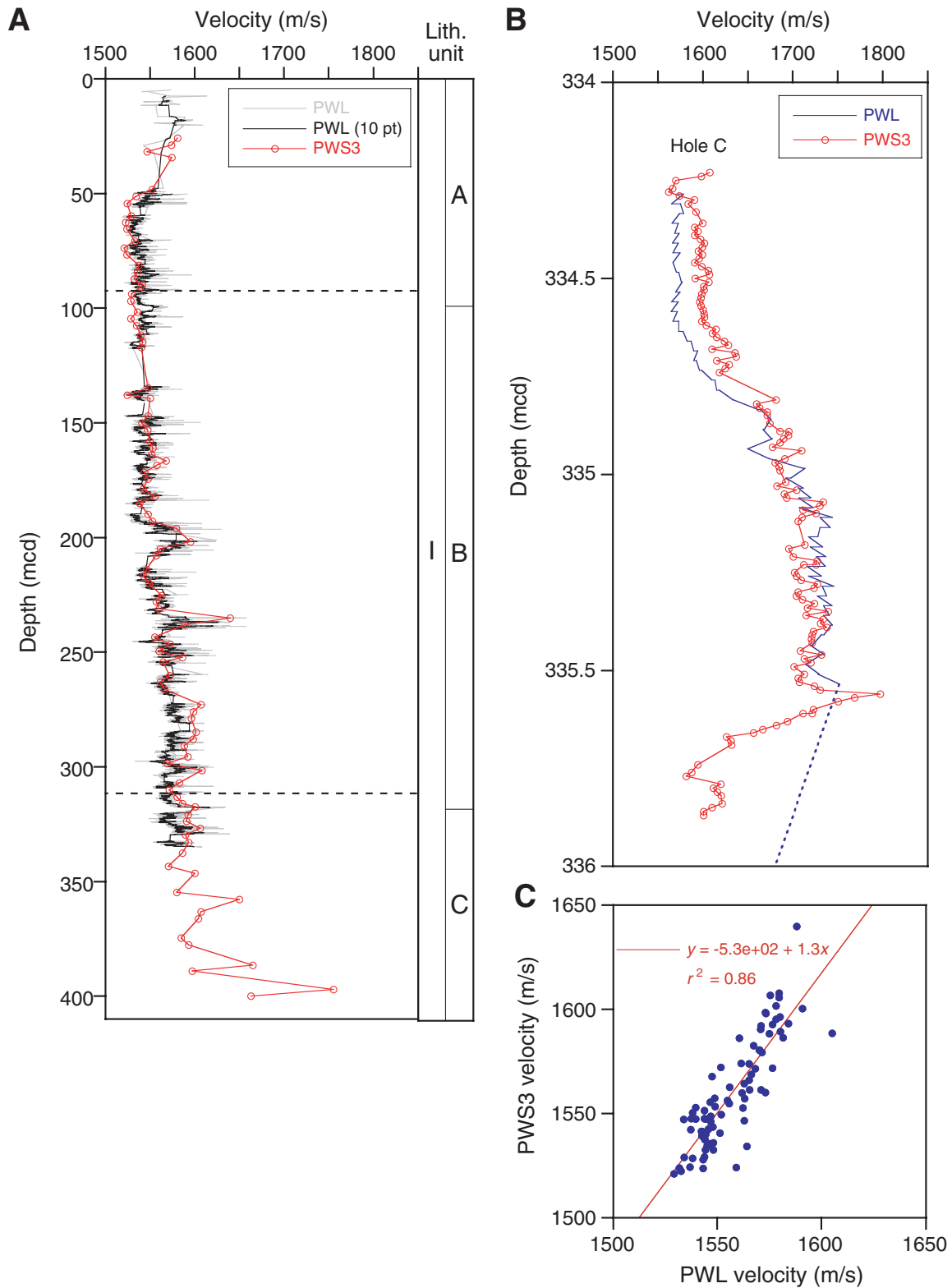


Figure F15. Site 1263 lithostratigraphic composite illustrating chromaticity (a^*), manganese and iron concentrations in the interstitial waters, and grain density.

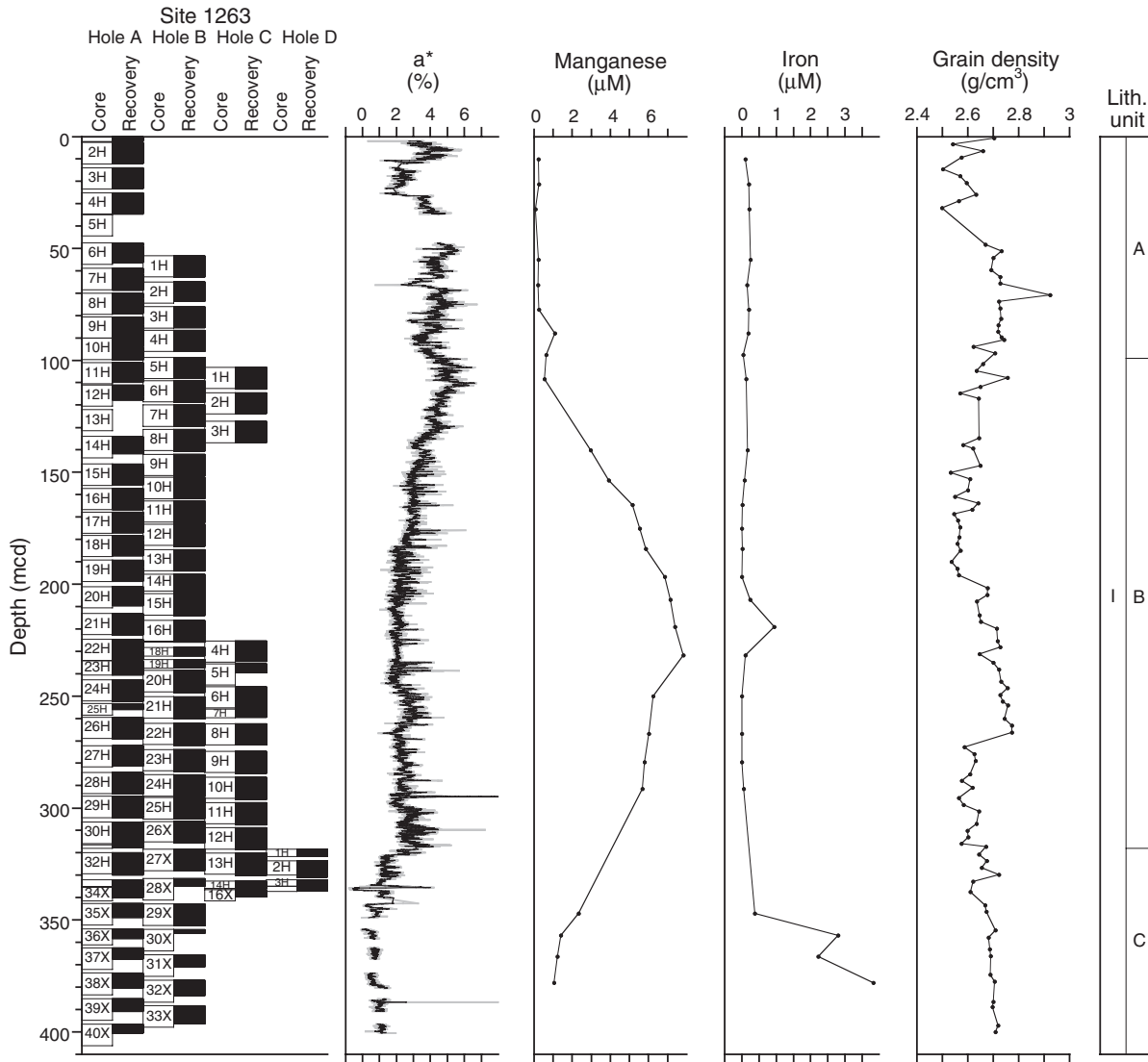


Figure F16. Close-up photograph of an angular contact coincident with an upper Neogene hiatus (interval 208-1263A-4H-1, 71–89 cm).

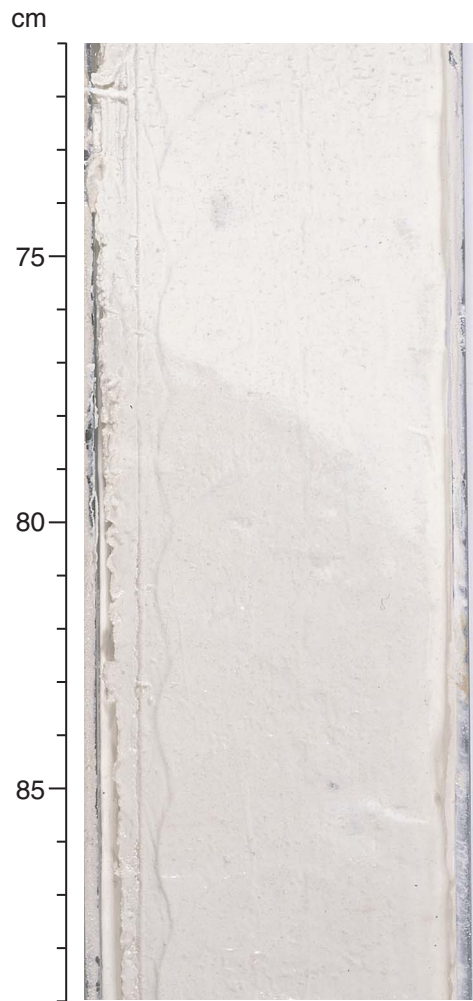


Figure F17. Composite digital image, red-green-blue color variations, sediment lightness (L^*), and magnetic susceptibility across the Eocene/Oligocene boundary interval (94.6–104.5 mcd), following the stratigraphic splice.

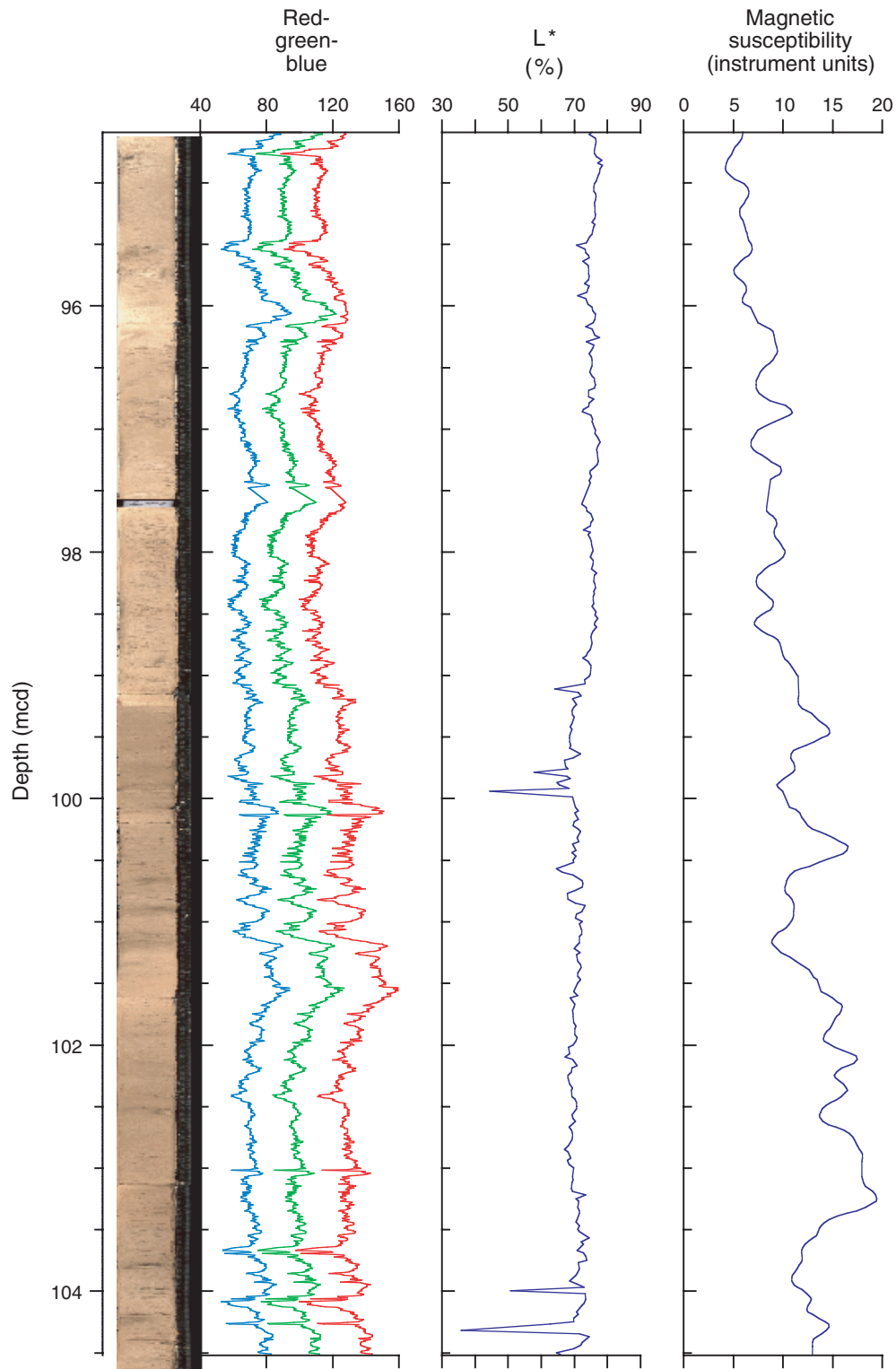


Figure F18. Composite digital image, sediment lightness (L^*), magnetic susceptibility, natural gamma radiation, and bulk density. A. Upper extreme of the Subunit IB cyclic interval. Natural gamma ray data are smoothed using a 5-point moving average. (Continued on next page.)

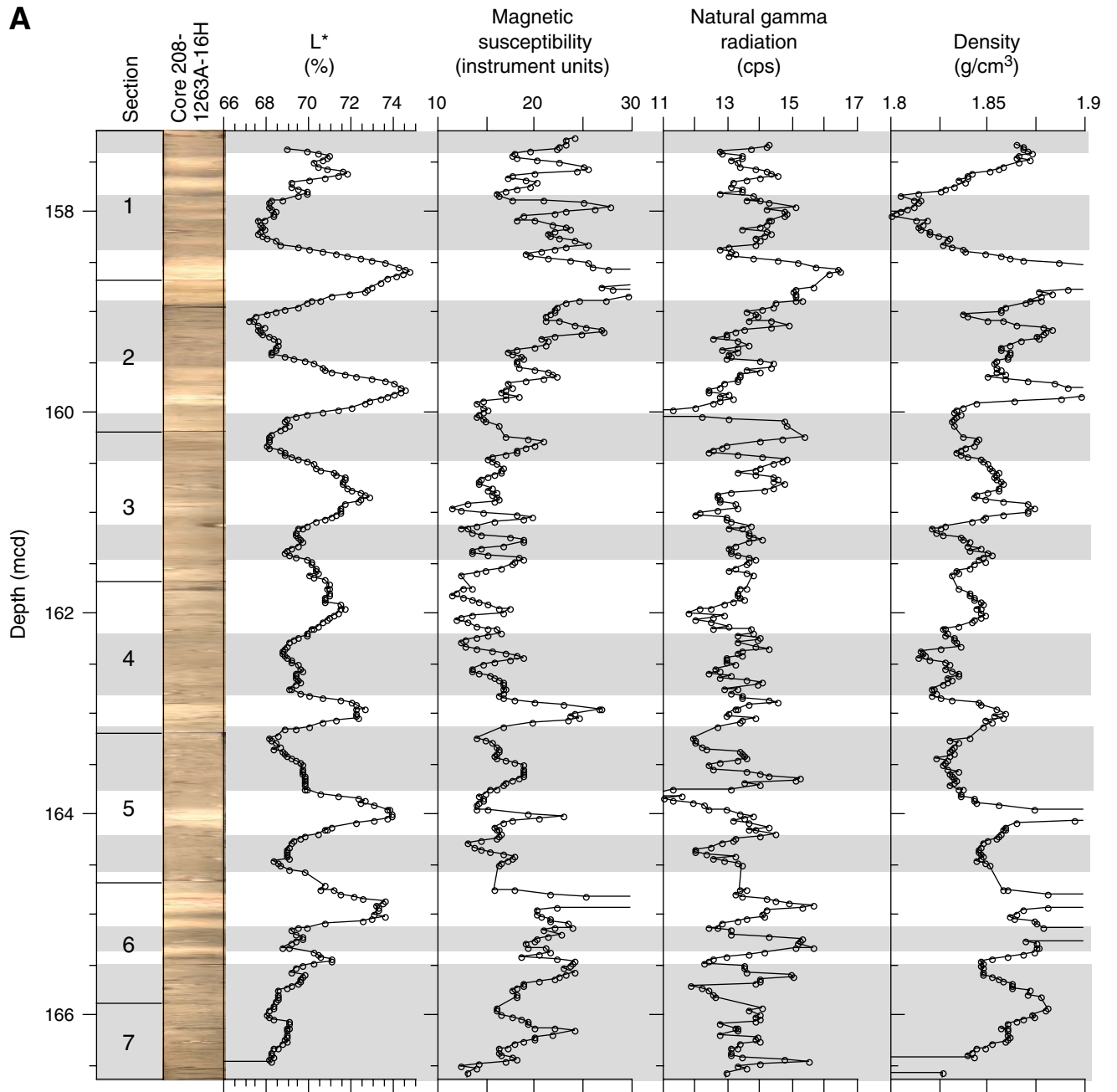


Figure F18 (continued). B. Lower extreme of the Subunit IB cyclic interval.

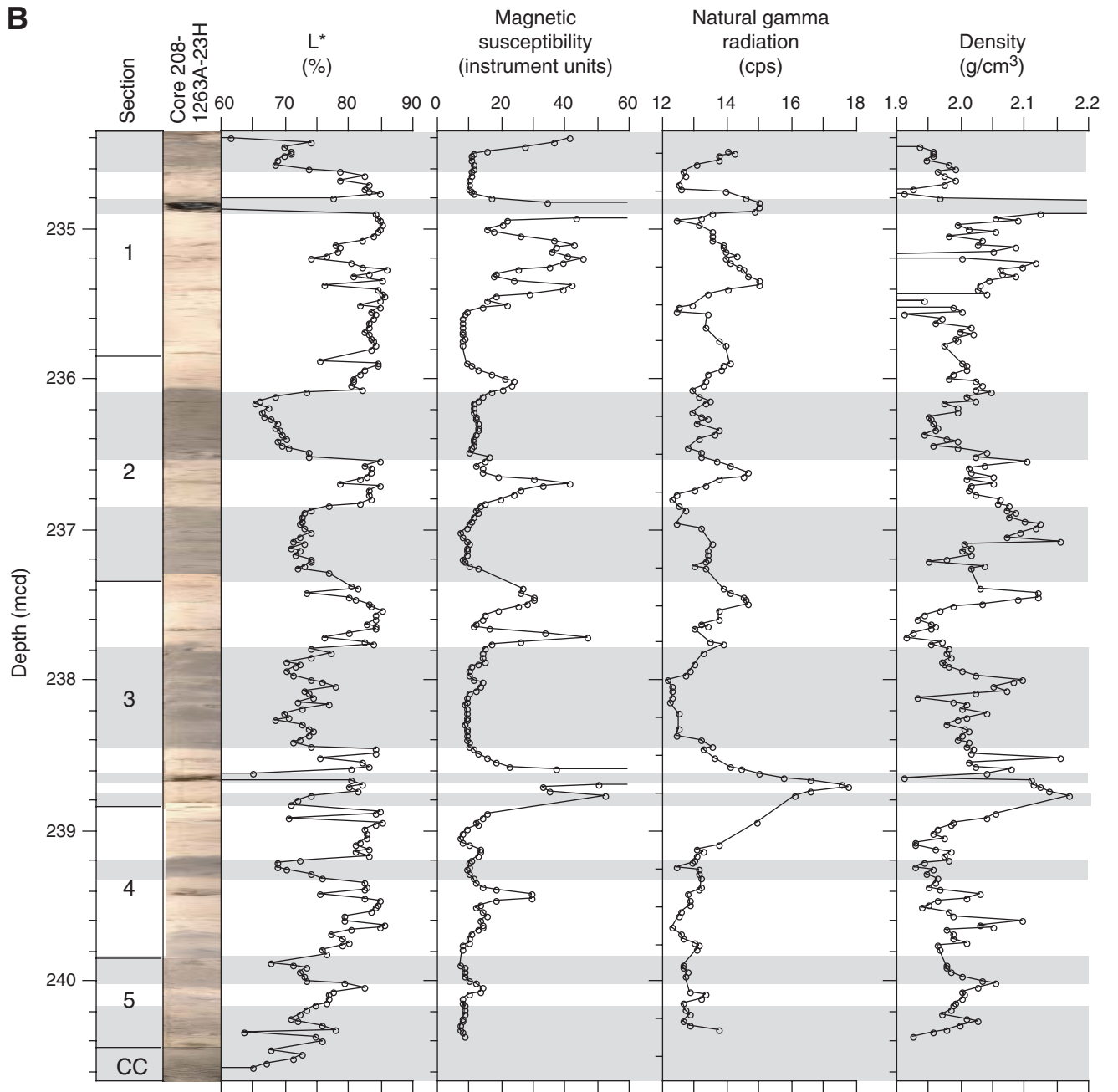


Figure F19. Close-up photographs of (A) large (interval 208-1263B-20H-4, 85–105 cm) and (B) small (interval 208-1263B-20H-5, 85–105 cm) light-colored blebs of nannofossil ooze with halos of fine opaque grains. Matrix sediment is also nannofossil ooze.

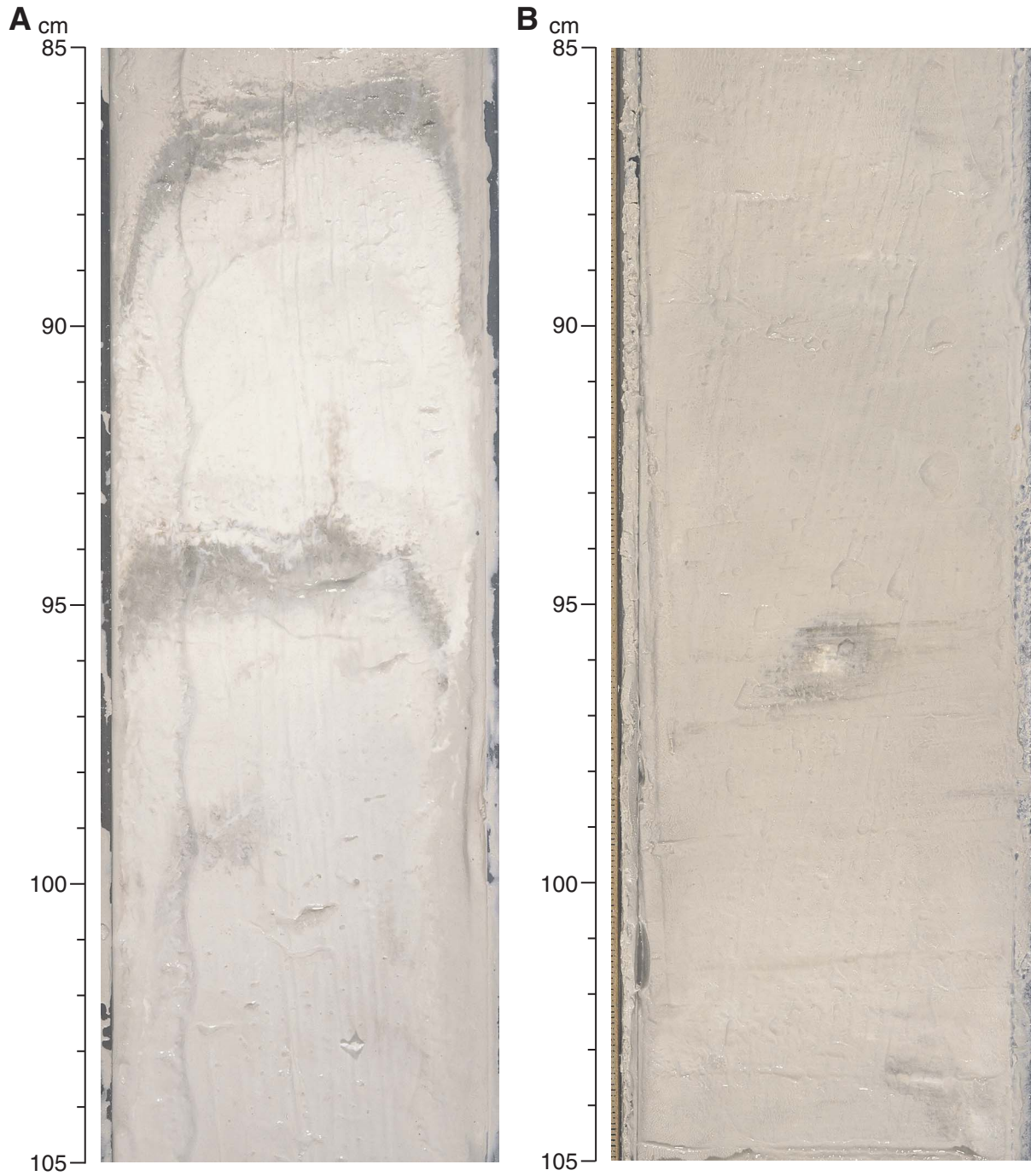


Figure F20. Composite digital image, sediment lightness (L^*), magnetic susceptibility, natural gamma radiation (5-point moving average of counts per second), and bulk density of the clay-enriched horizons in Subunit IB.

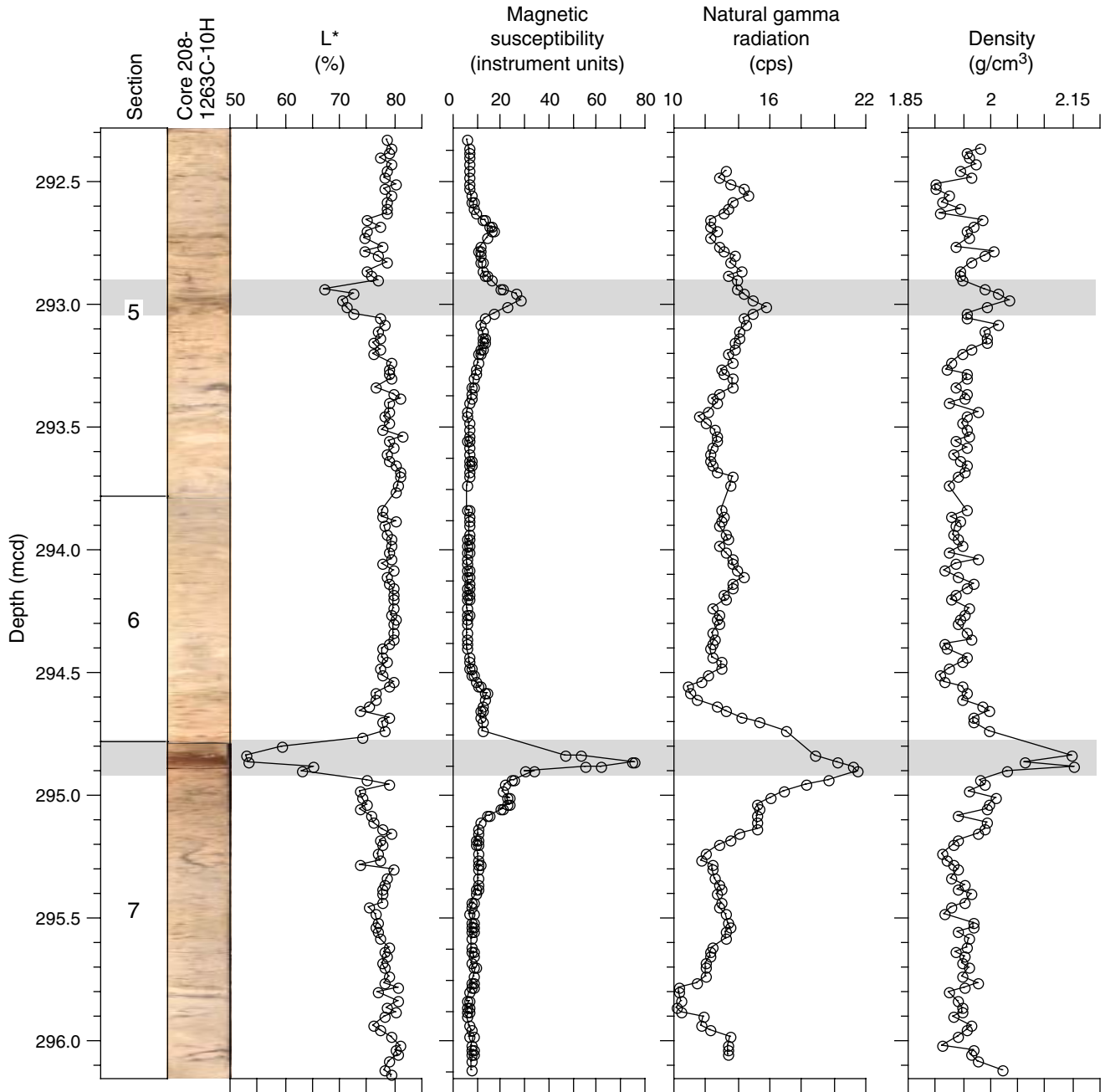


Figure F21. Site 1263 high-resolution composite digital images of P/E boundary sections in Holes 1263A, 1263C, and 1263D (345.5–346.0 mcd) depicting abrupt chromaticity (a^* [red diamonds]) and magnetic susceptibility (black circles) changes. Carbonate content (blue triangles) is illustrated for Hole 1263C. The Site 1263A clay/carbonate contact is unconformable. Roughly 25 cm of the basal clay is missing.

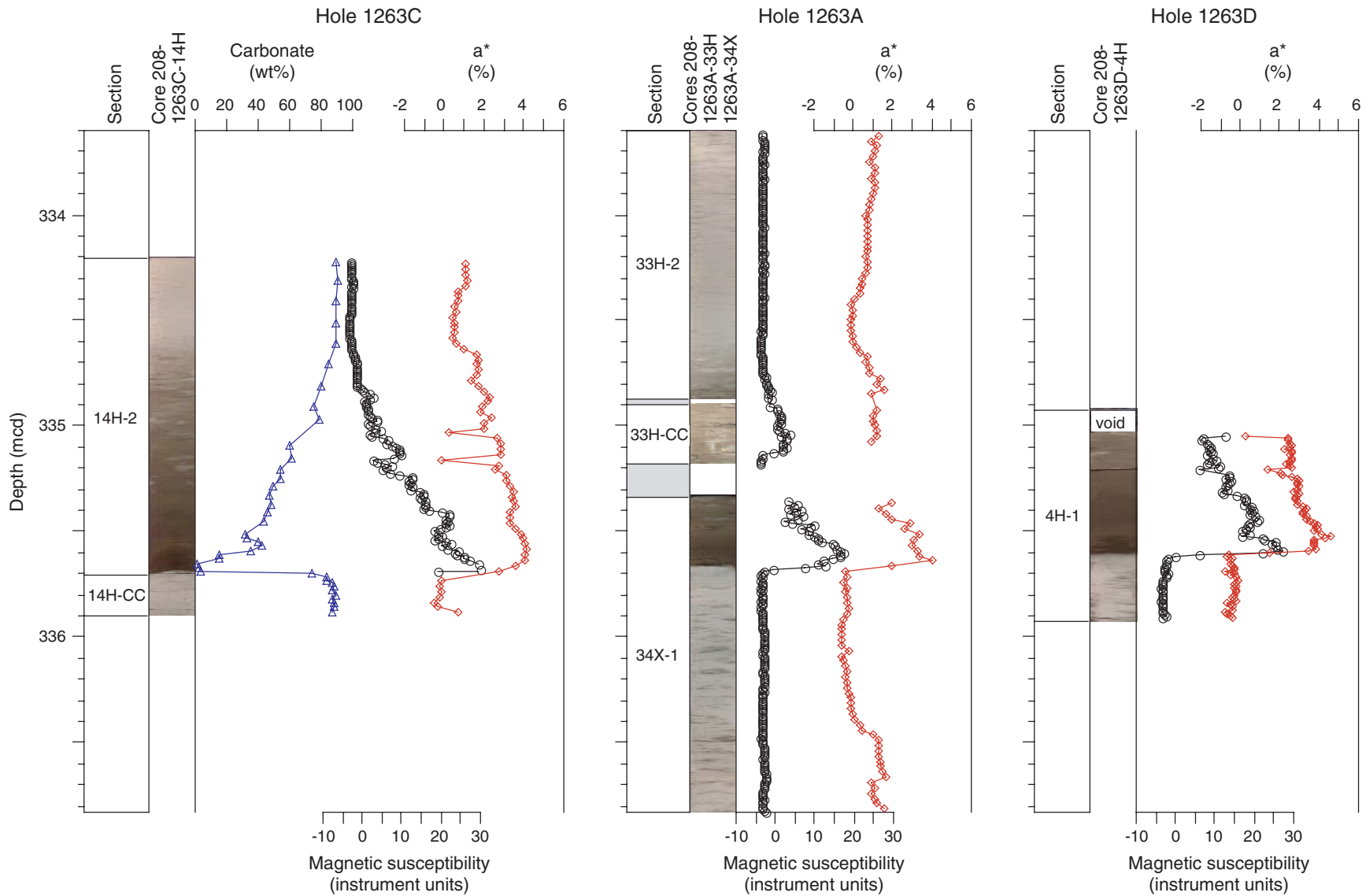


Figure F22. Summary of composite planktonic foraminiferal and calcareous nannofossil biozonation constructed for Site 1263. Paleobathymetric history of Site 1263 is inferred from benthic foraminifers shown on right. Shading indicates an interval of reworking.

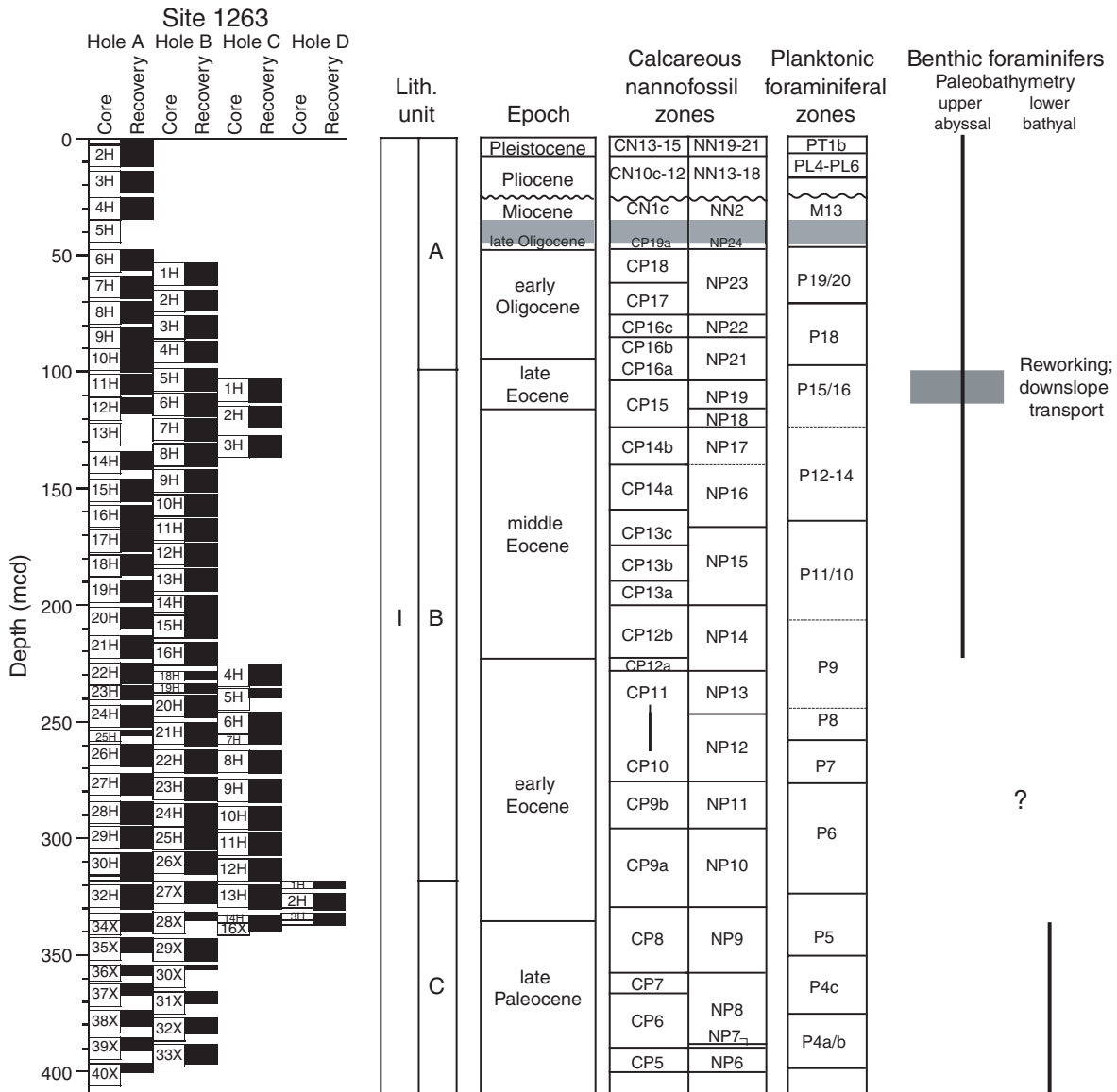


Figure F23. Summary of sedimentation rates at Site 1263 constructed using datum levels of calcareous nan-
nofossils and planktonic and benthic foraminifers.

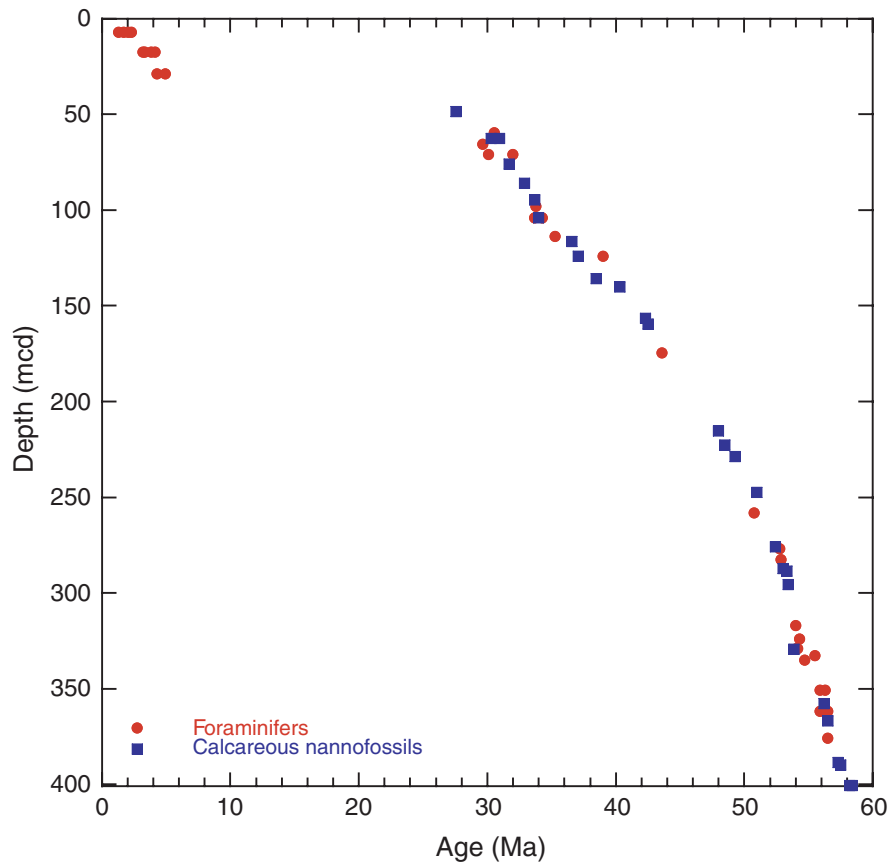


Figure F24. Typical examples of orthogonal vector endpoint (left), intensity (middle), and equal-area (right) diagrams for progressive demagnetization results from archive-half Section 208-1263B-2H-3. Open circles = vertical projection in the orthogonal diagram and the upper hemisphere in the equal area diagram, respectively.

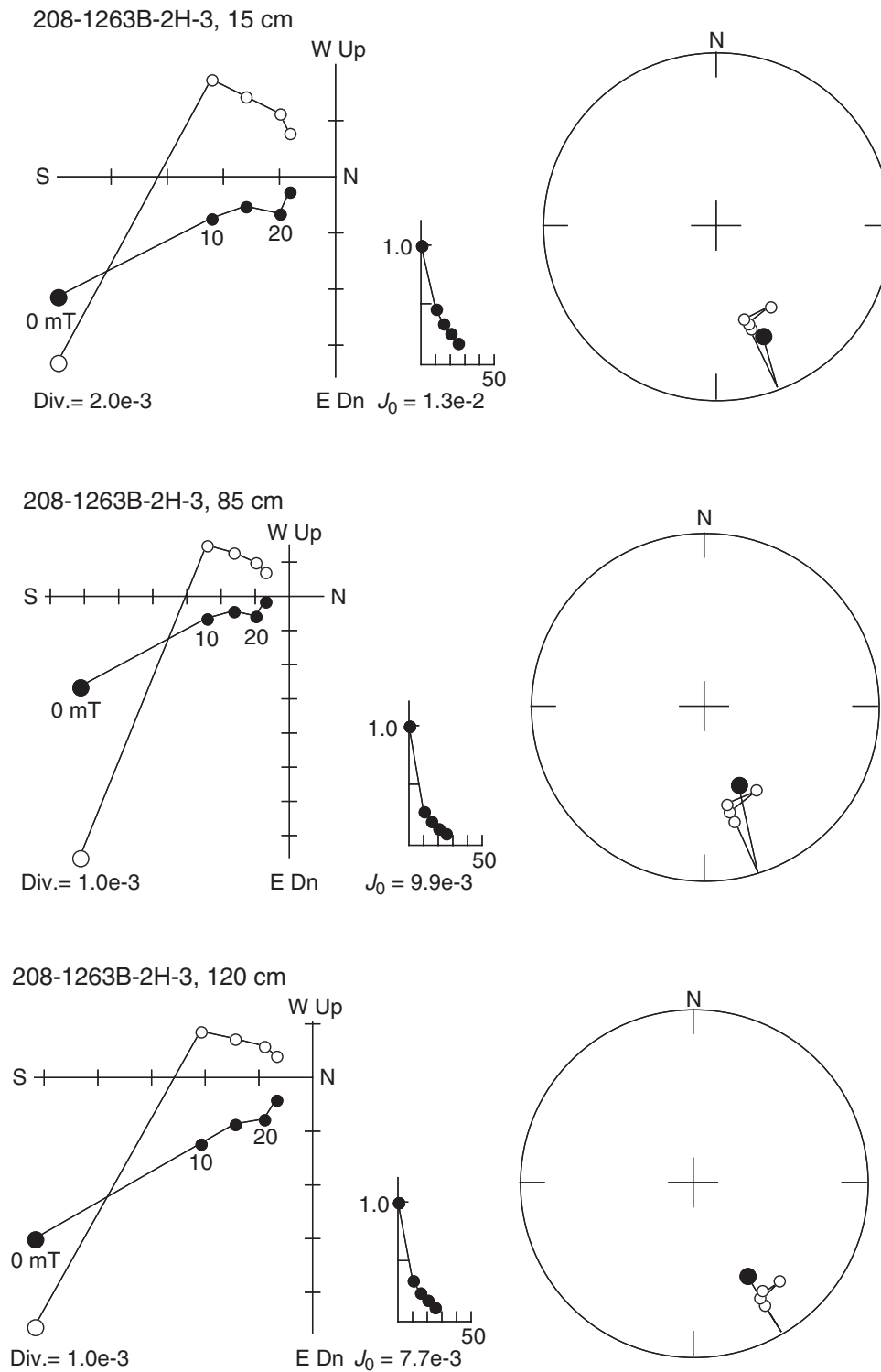


Figure F25. Inclinations after demagnetization at 15 mT from pilot discrete samples (squares) and archive-half cores (line with dots) at Hole 1263A.

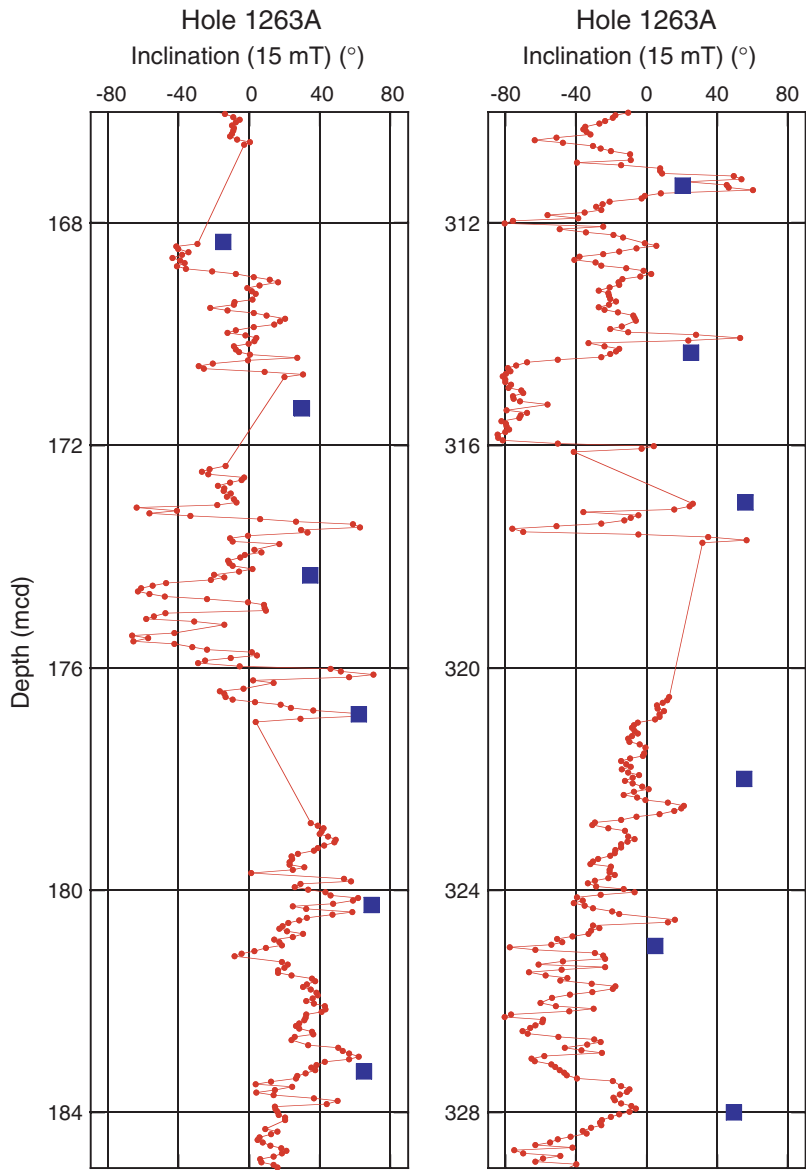


Figure F26. Downhole variation in intensities of remanent magnetization before (gray) and after demagnetization at 15 mT (black) at Holes 1263A, 1263B, 1263C, and 1262D.

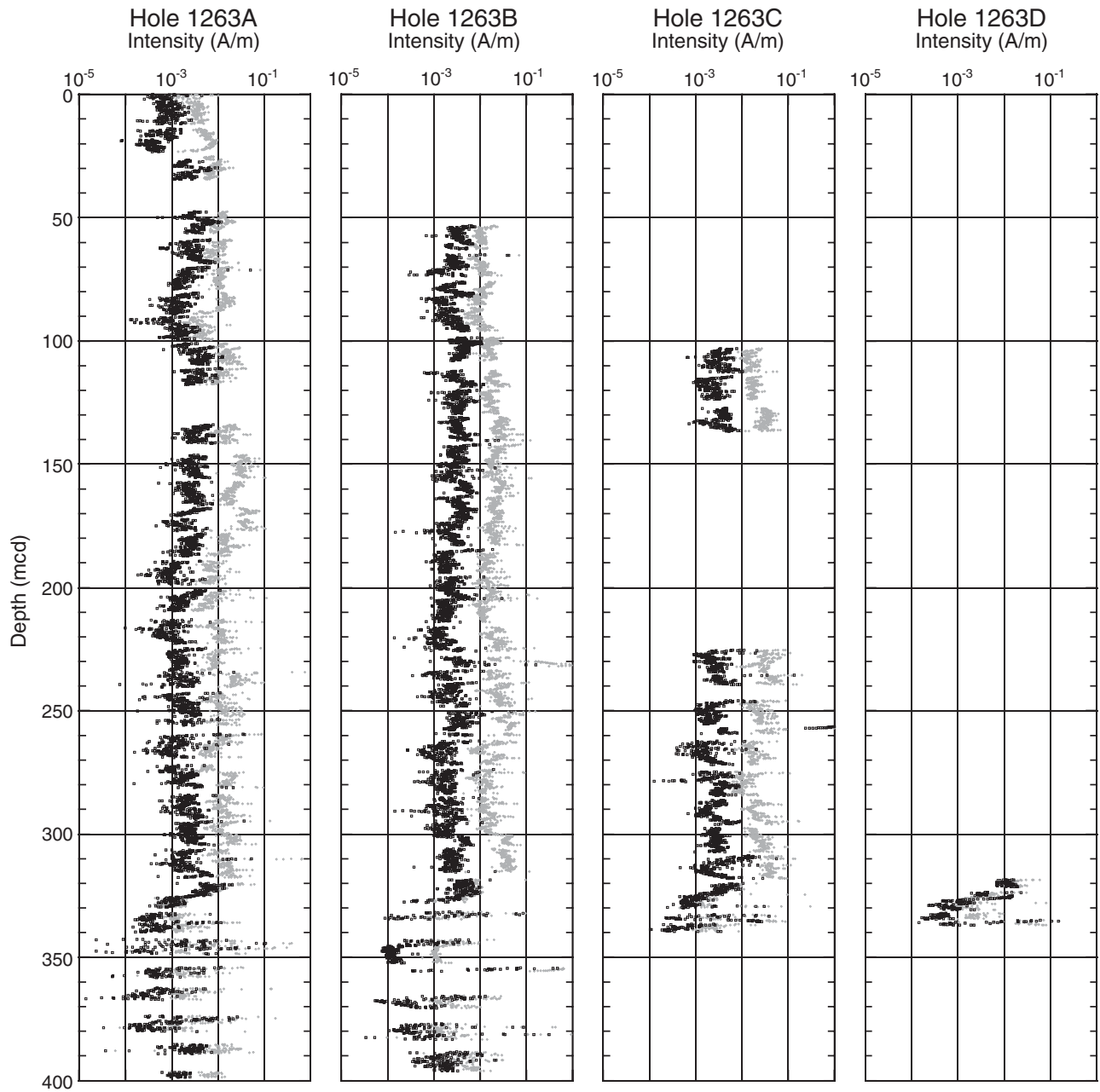


Figure F27. Preliminary magnetostratigraphic interpretation for Site 1263. Inclination data after demagnetization at 15 mT is shown for Holes 1263A, 1263B, and 1263C. Data within 50 cm of a core top and 5 cm of section ends are not shown. Core breaks are denoted by green squares. Black rectangles = normal polarity, white = reversed polarity, shaded = uncertain polarity. X = intervals with no core recovery. A. 0–110 mcd. (Continued on next three pages.)

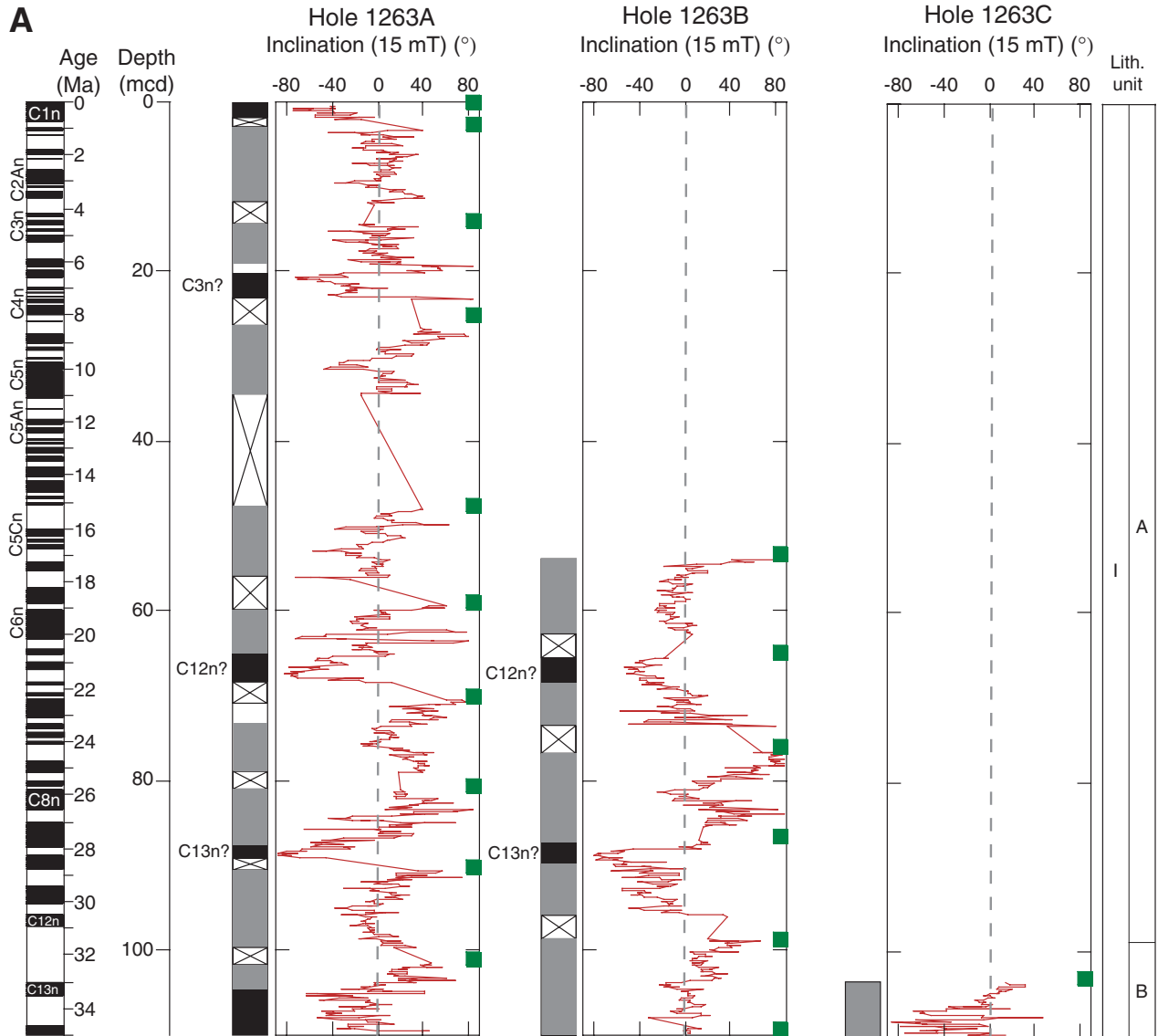


Figure F27 (continued). B. 100–210 mcd.

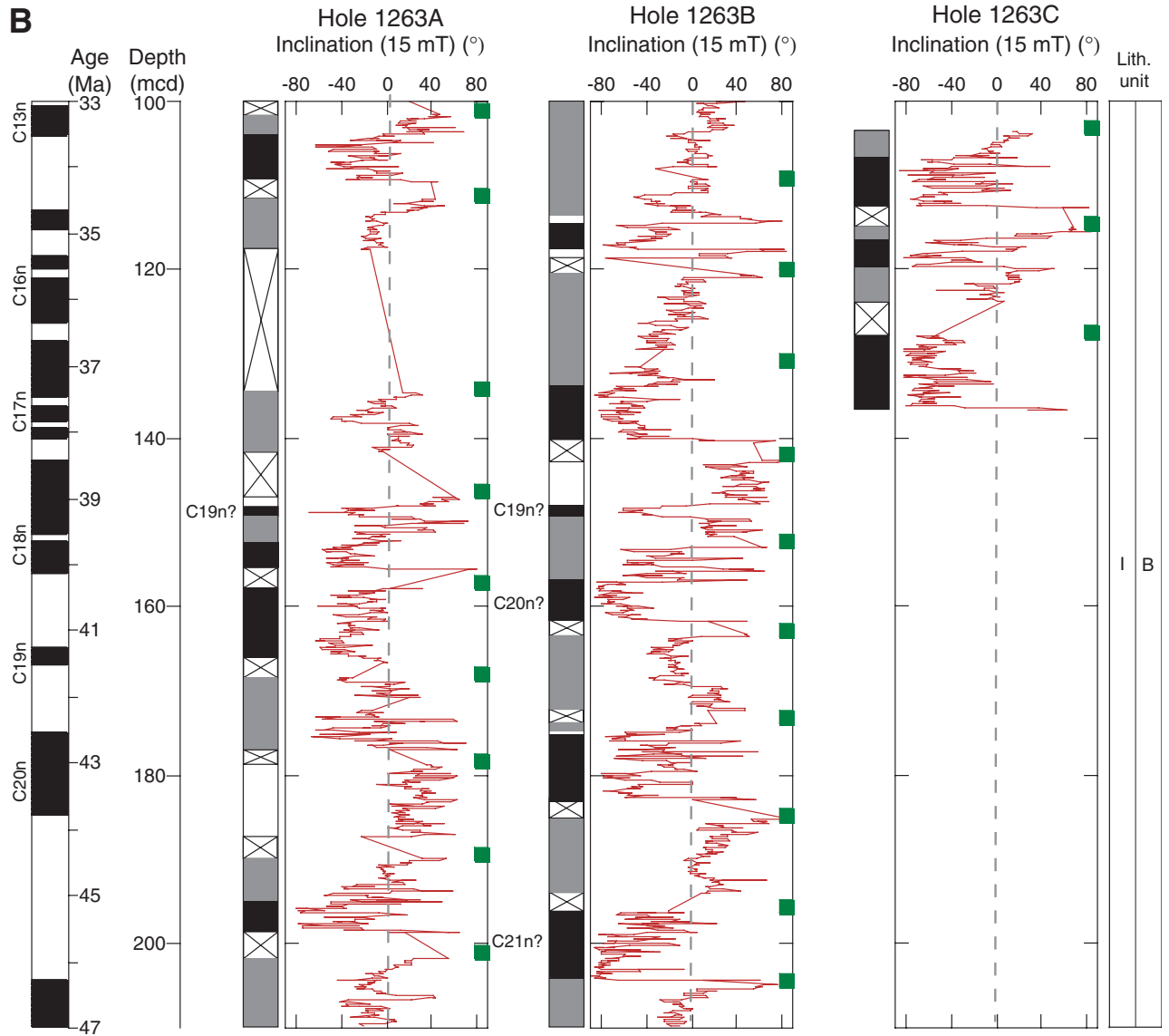


Figure F27 (continued). C. 200–310 mcd.

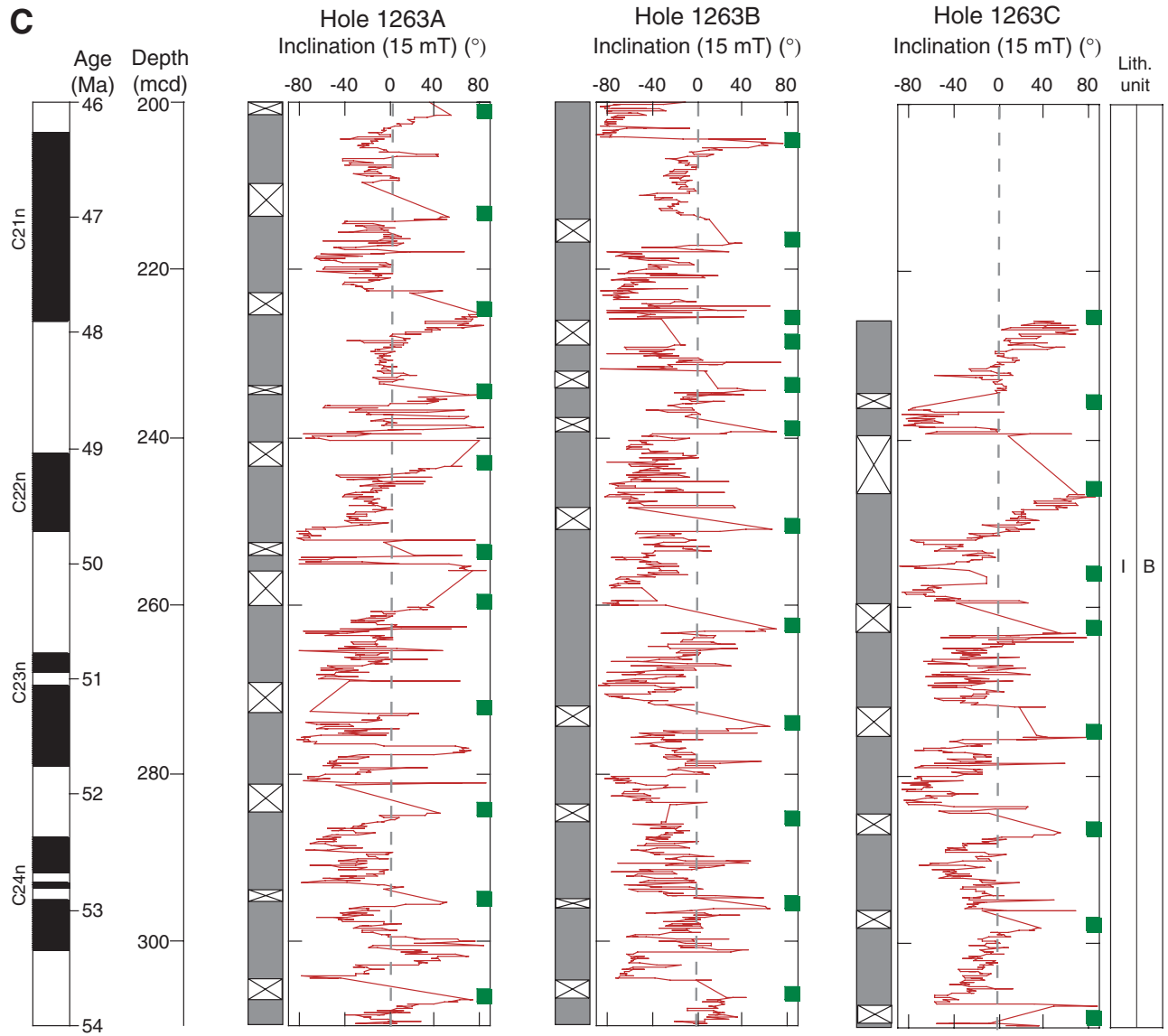


Figure F27 (continued). D. 300–410 mcd.

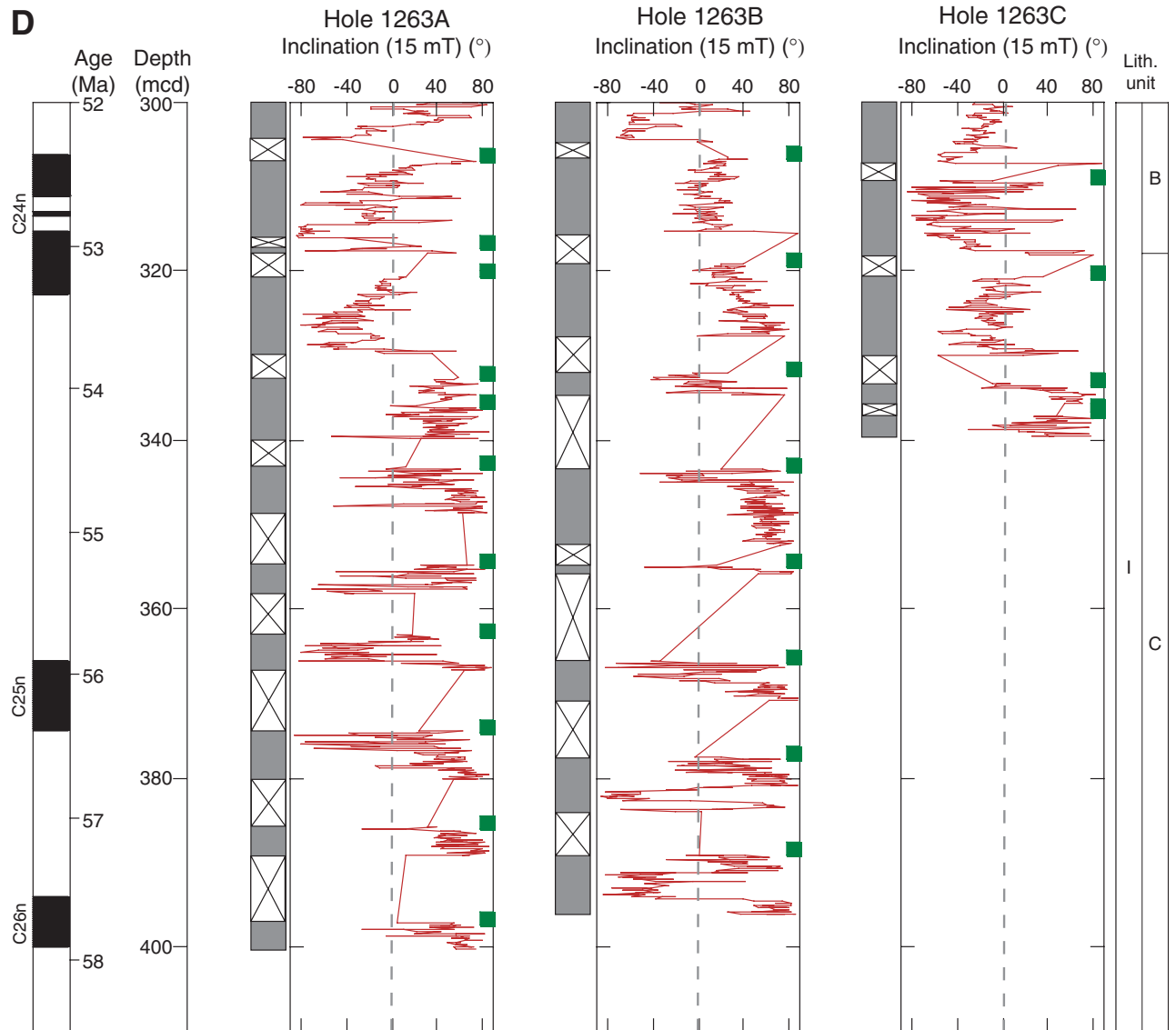


Figure F28. Profiles of chemical constituents in interstitial waters from Site 1263. Error bars (1σ relative standard deviation as a percentage) are plotted where they are larger than the plot symbols. A. Alkalinity. B. Chloride. C. Sodium. D. Potassium. E. Calcium. F. Magnesium. G. Strontium. H. Lithium. I. Boron. J. Barium. K. Sulfate. L. Manganese. M. Iron. N. Silicon. O. Zinc.

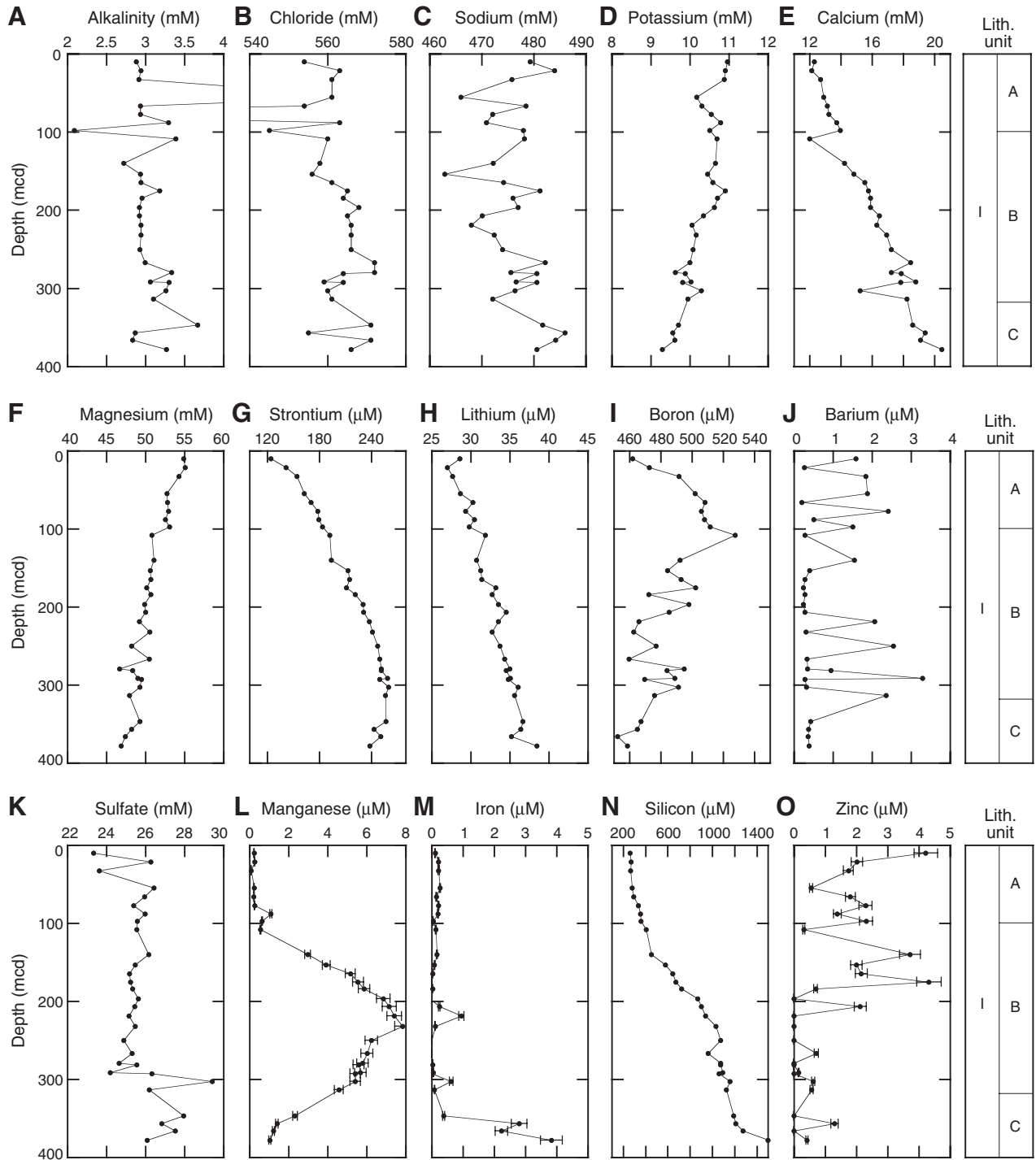


Figure F29. Sedimentary carbonate contents vs. composite depth for (A) the entire section and (B) the P/E boundary interval at high resolution.

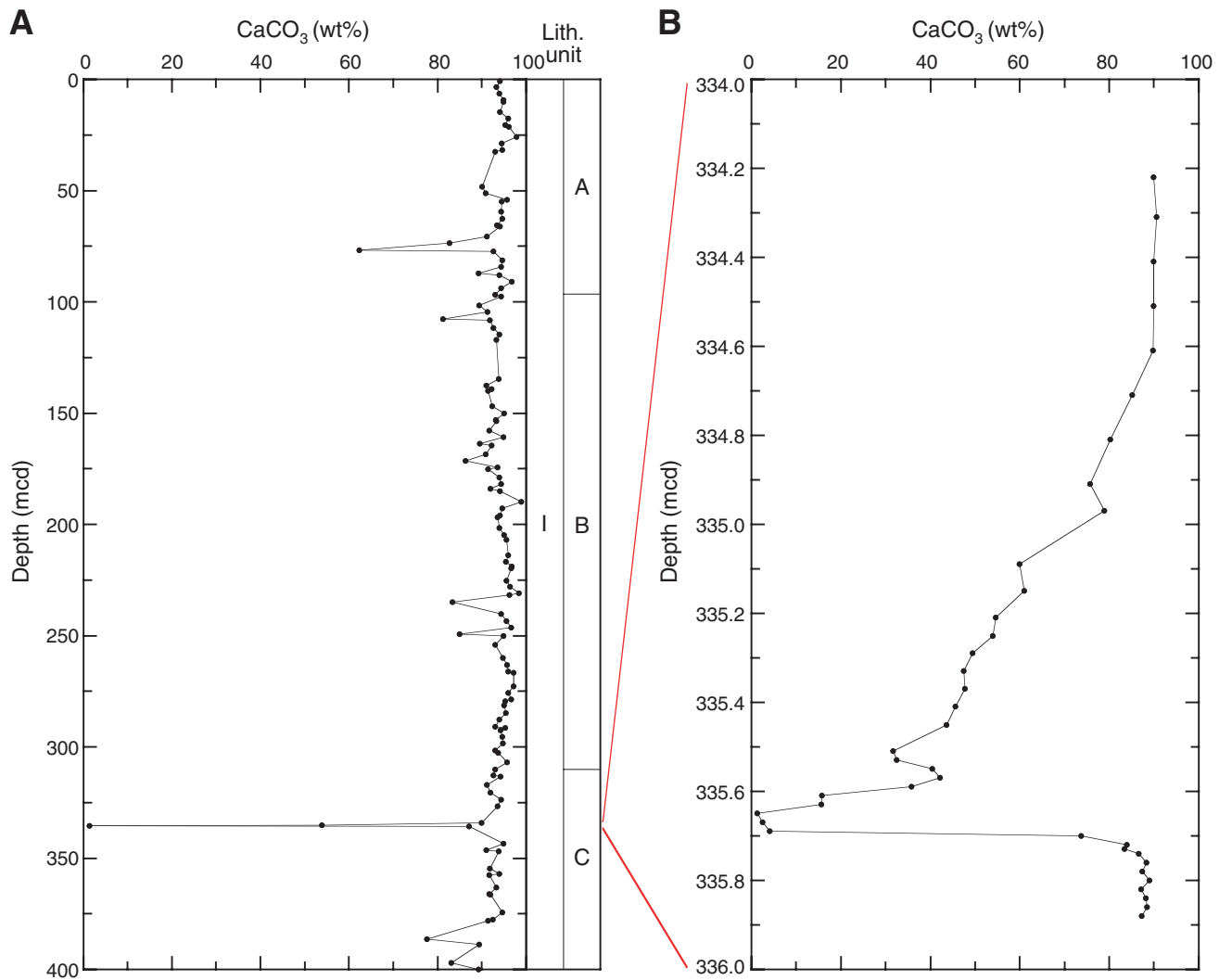


Figure F30. Summary of the logging operations undertaken at Hole 1263A.

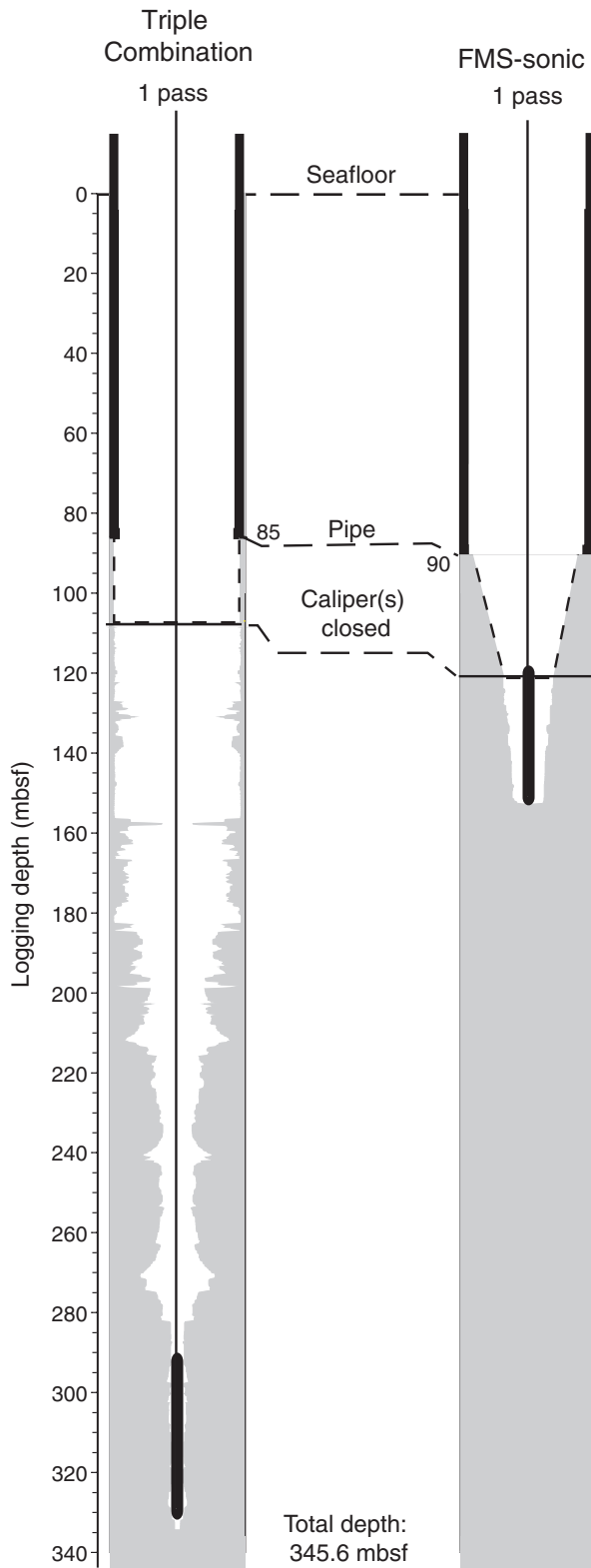


Figure F31. Quality control and depth matching of the data from the triple combo and FMS-sonic tool string. Triple combo tool string: (A) Caliper measurements of hole diameter, (B) normalized vertical tool acceleration (NAz), and (C) depth-scale (wavelet transform) representation of NAz between 130 and 280 mbsf. FMS-sonic tool string: (D) Caliper measurement of hole diameter, (E) NAz, (F) close-up (110 and 150 mbsf) of caliper measurements. Both tool strings: (G) Computed gamma radiation (HCGR and environmentally corrected gamma radiation (ECGR) logs from Hole 1263A. Note the discrepancy between the triple combo and the FMS caliper data. See Table T14, p. 85, for acronyms.

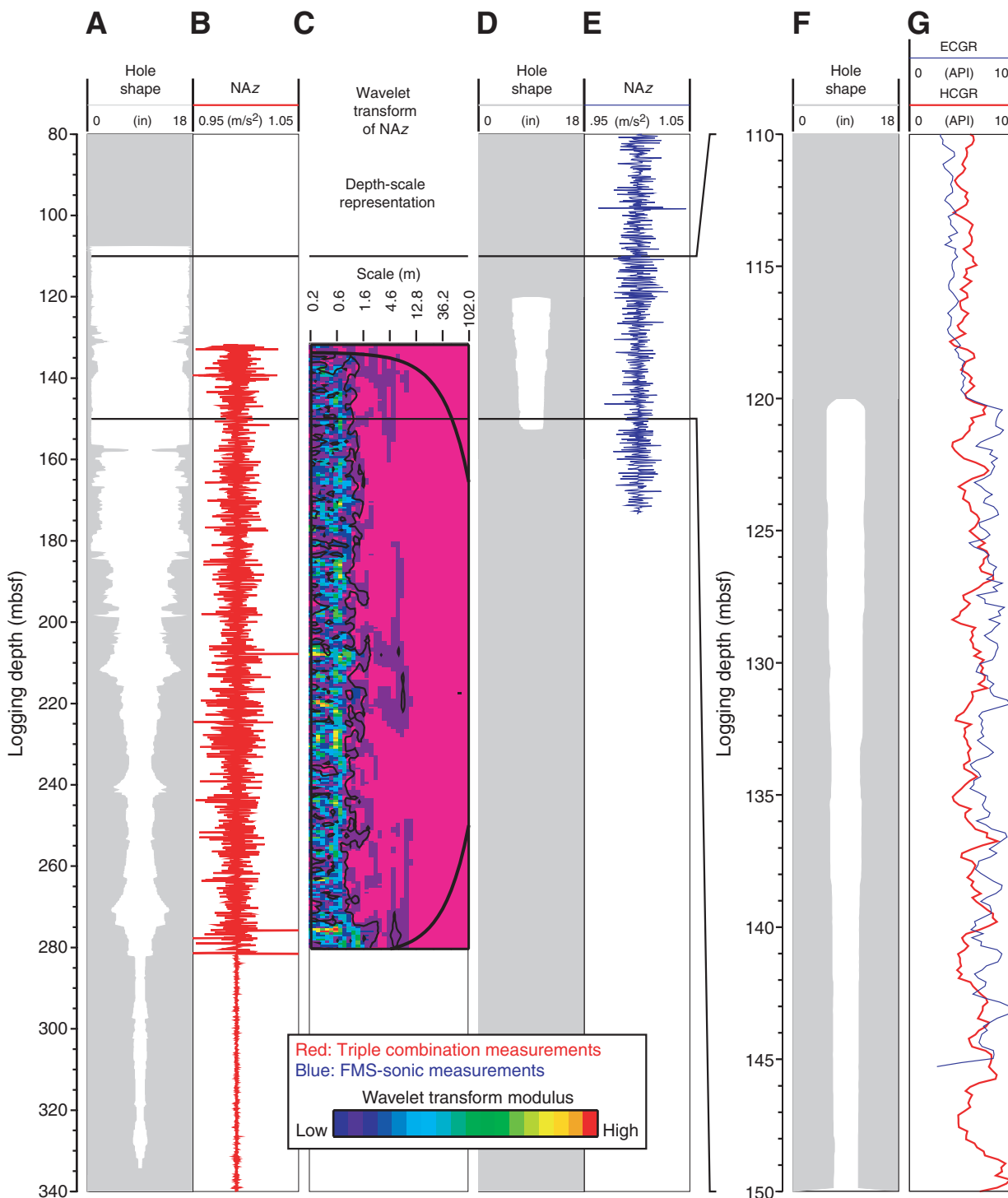


Figure F32. Downhole logging stratigraphy from triple combo tool string logs. **A.** Hole shape and computed gamma ray (HCGR). **B.** Total gamma ray (HSGR) and uranium contribution (HURA). **C.** Potassium (HFK) and thorium (HTHO) contributions to natural radioactivity. **D.** Deep (IDPH), intermediate (IMPH), and shallow (SFLU) resistivities. **E.** Porosity (APLC) and capture cross section (Σf). **F.** Formation density (RHOM) and photoelectric factor (PEF). **G.** Transient temperature downlog (T_{down}) and uplog (T_{up}). **H.** Logging subunits. **I.** Rescaling of the total gamma ray (HSGR) and shallow resistivity (SFLU) logs between 80 and 280 mbsf to better underline the limit between logging Subunits 1a and 1b.

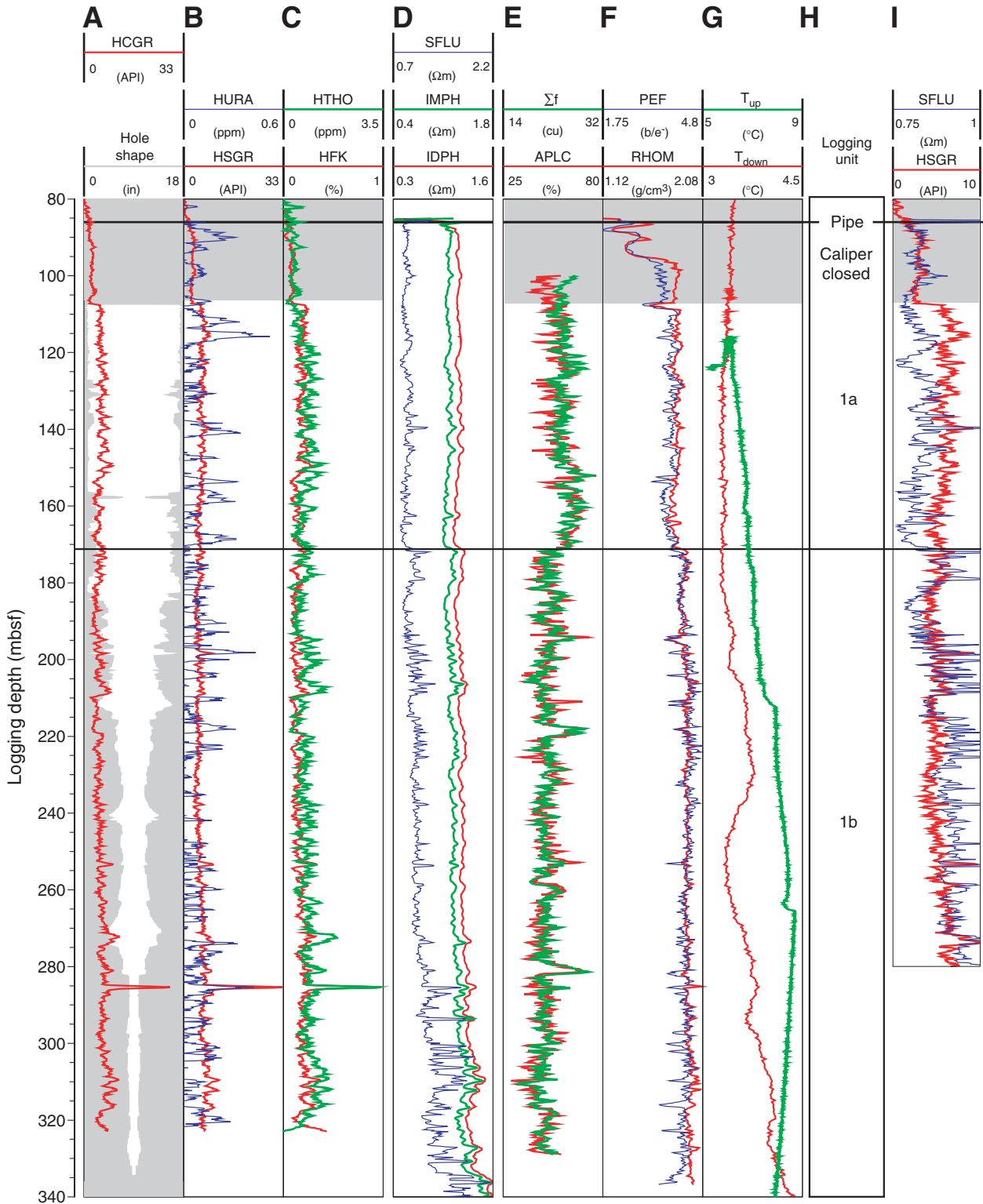


Figure F33. Wavelet transform (modulus) of density (RHOM), porosity (APLC), total gamma radiation (HSGR), medium resistivity (IMPH), and surface resistivity (SFLU) between 110 and 270 mbsf. Red = high modulus, blue = low modulus. Thin solid lines bracket intervals of statistically significant modulus. Thick solid lines separate zones where edge effects become important. Thin dashed lines mark the main cycles at ~4, ~11, and ~25 m.

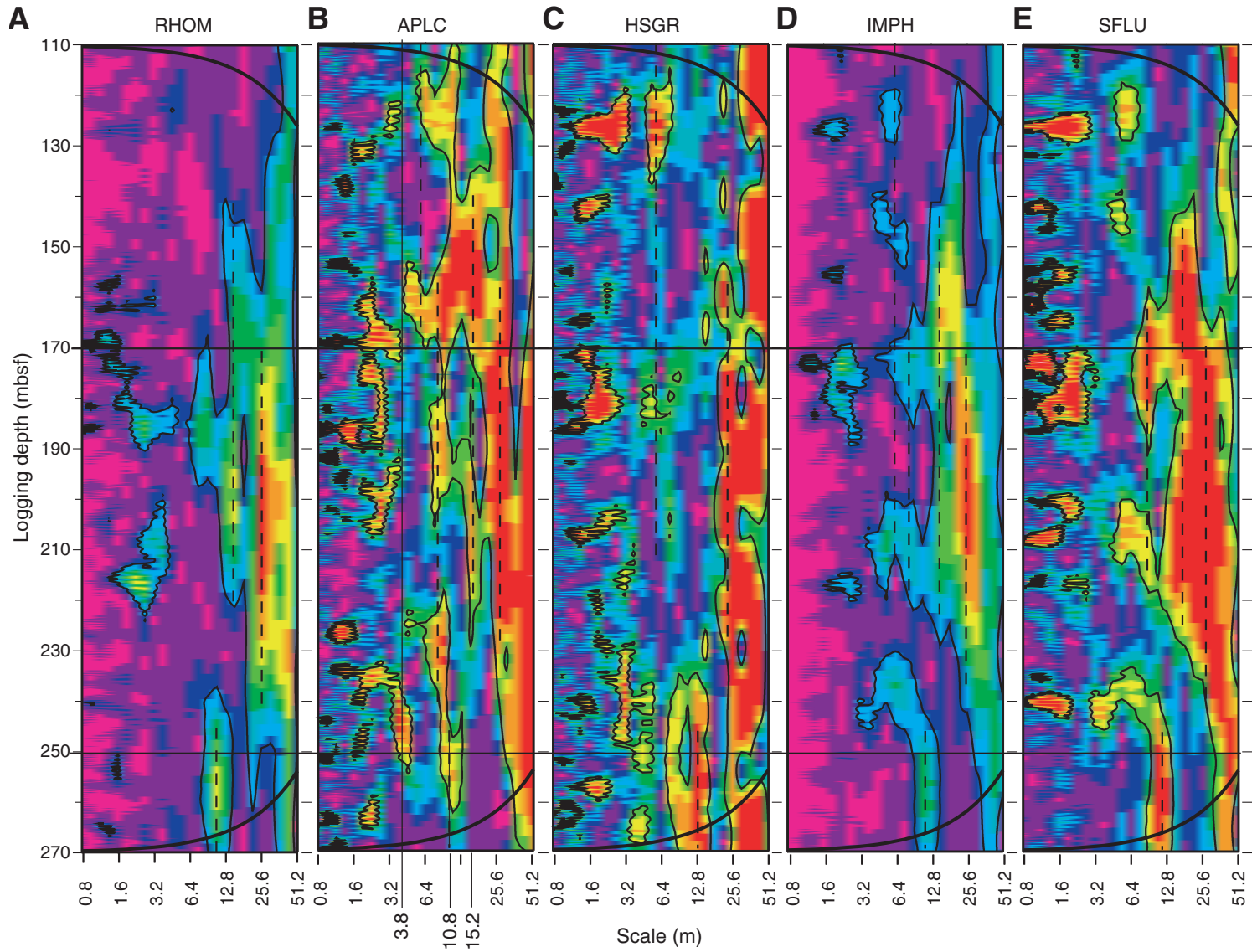


Figure F34. Core-log integration. A. Hole shape, total gamma radiation (HSGR), porosity (APLC), density (RHOM), compressional wave velocity (V_p), and lithostratigraphy and logging subunits. (Continued on next page.)

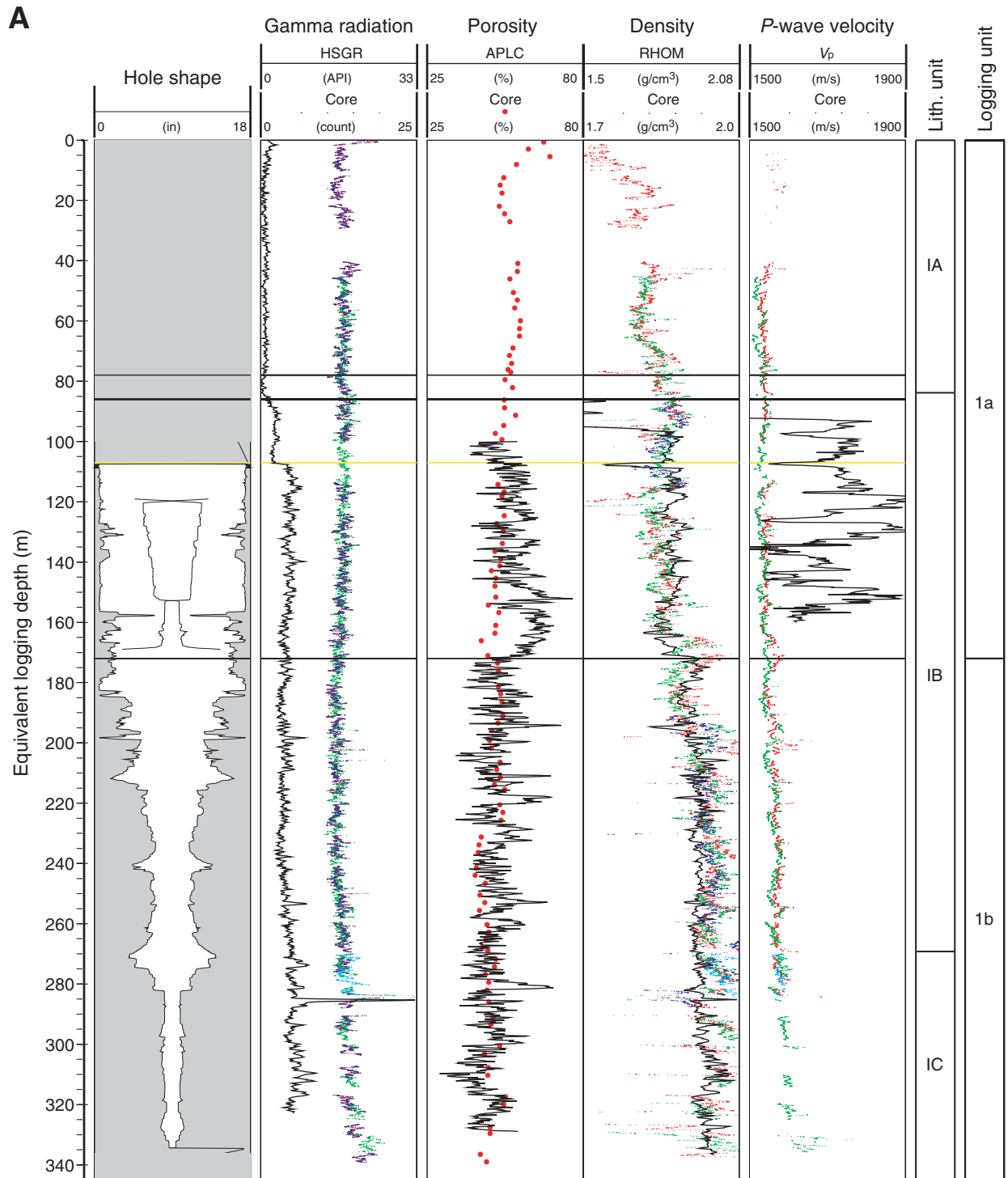


Figure F34 (continued). B. Core recovery, lithology, lithostratigraphic units, magnetic susceptibility, and color reflectance (L^* , a^* , and b^*) data vs. equivalent logging depth.

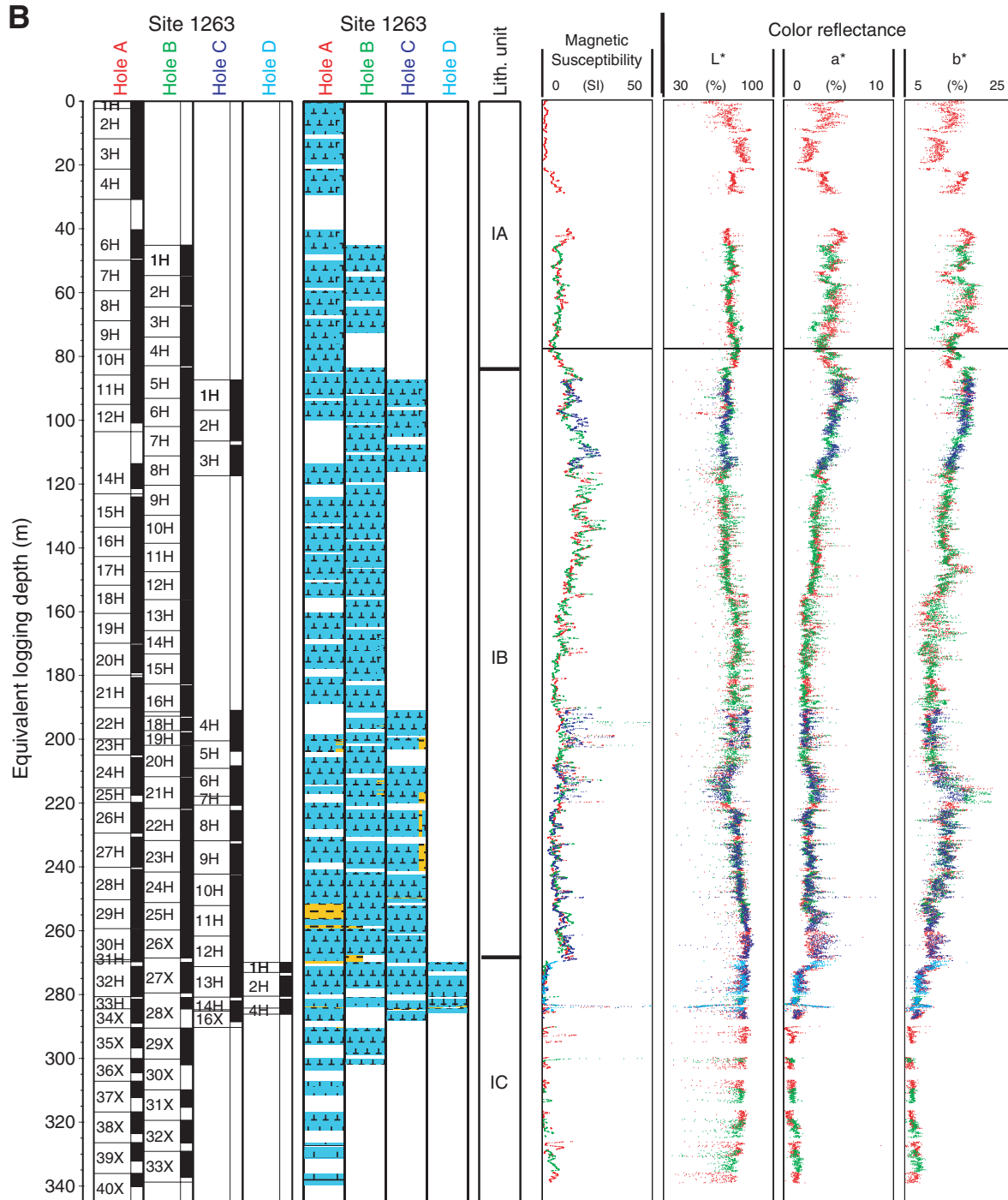


Figure F35. Formation MicroScanner (FMS) images and cyclostratigraphic limitations. A. Hole shape. B, C. Static and dynamic (window height = 0.5 m) normalization of the microresistivity images. D. Extracted FMS button records showing the weak amplitude of the resistivity measurement in spite of the good pad-formation contact. E. Shallow resistivity (SFLU) for comparison.

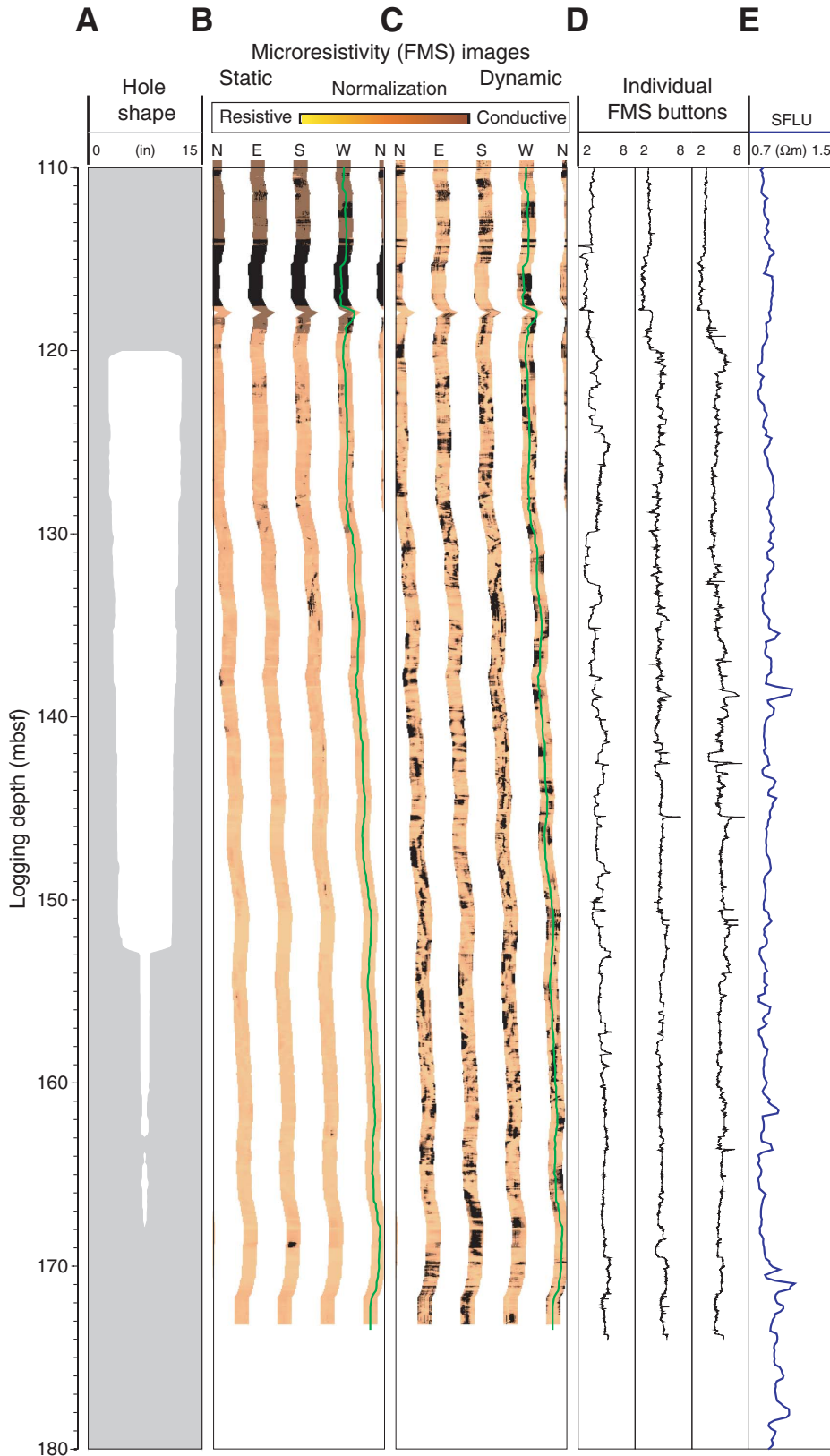


Figure F36. Seismic modeling inputs. (A) Sonic velocity in cores vs. core density, (B) downhole density vs. core density, and (C) downhole density vs. sonic velocity in cores. The equivalent logging depth was used as a common depth scale for the data.

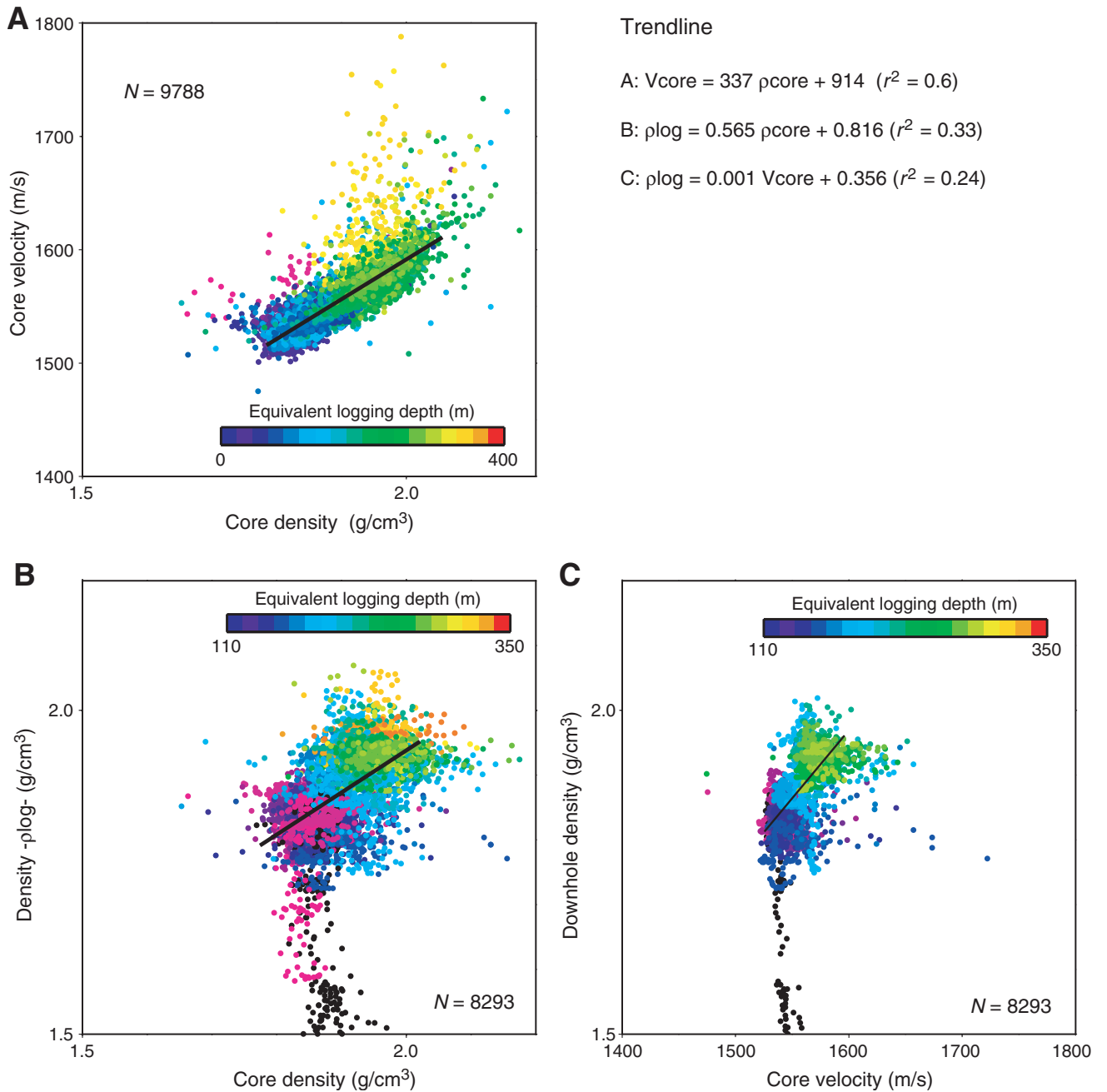


Figure F37. A. Core recovery plot. B. Shipboard biostratigraphic and magnetostratigraphic datums and the interpreted age-depth model. C. Corrected linear sedimentation rate (LSR), total, carbonate, and noncarbonate mass accumulation rates (MAR), calculated from the age model sampled at 1-m.y. intervals, and dry density and calcium carbonate concentrations averaged over the same 1-m.y. intervals. T = top, B = bottom.

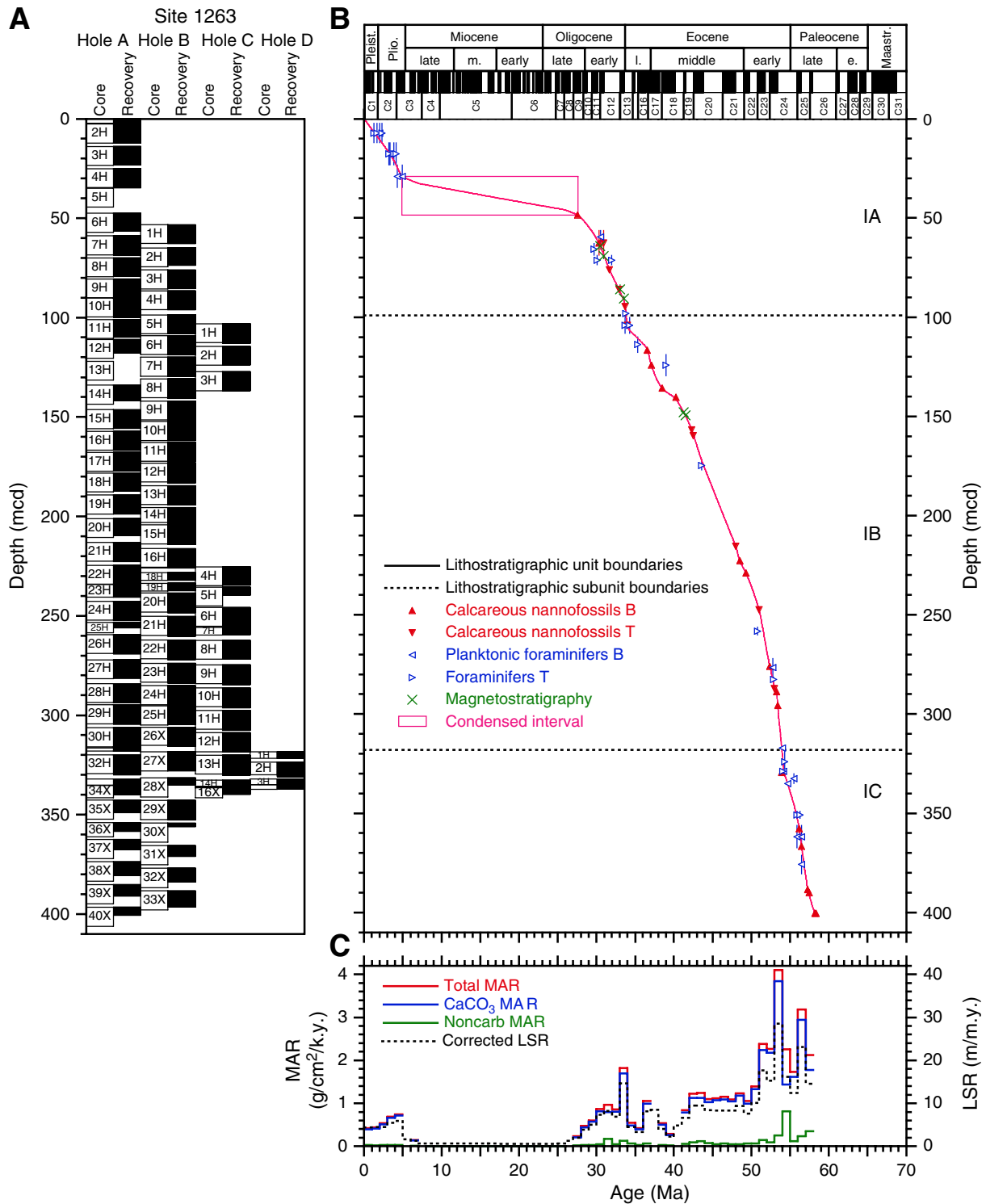


Table T1. Coring summary, Site 1263. (See table notes. Continued on next page.)

Core	Date (2003)	Local time (hr)	Depth (mbsf)		Length (m)		Recovery (%)	Comments
			Top	Bottom	Cored	Recovered		
208-1263A-								
1H	30 Mar	150	0.0	2.3	2.3	2.34	101.7	
2H	30 Mar	235	2.3	11.8	9.5	9.46	99.6	NMCB
3H	30 Mar	320	11.8	21.3	9.5	9.47	99.7	Tensor
4H	30 Mar	430	21.3	30.8	9.5	9.60	101.1	APCT, Tensor
5H	30 Mar	510	30.8	40.3	9.5	0.00	0.0	Tensor
6H	30 Mar	550	40.3	49.8	9.5	8.85	93.2	Tensor, NMCB
7H	30 Mar	705	49.8	59.3	9.5	9.86	103.8	APCT, Tensor
8H	30 Mar	750	59.3	68.8	9.5	9.10	95.8	Tensor, NMCB
9H	30 Mar	840	68.8	78.3	9.5	9.50	100.0	Tensor
10H	30 Mar	935	78.3	87.8	9.5	9.93	104.5	APCT, Tensor
11H	30 Mar	1020	87.8	97.3	9.5	8.87	93.4	Tensor
12H	30 Mar	1110	97.3	106.8	9.5	6.82	71.8	Tensor, NMCB
13H	30 Mar	1210	106.8	116.3	9.5	0.00	0.0	APCT, Tensor
14H	30 Mar	1300	116.3	125.8	9.5	7.80	82.1	Tensor, NMCB
15H	30 Mar	1340	125.8	135.3	9.5	9.50	100.0	Tensor
16H	30 Mar	1435	135.3	144.8	9.5	9.63	101.4	Tensor, NMCB
17H	30 Mar	1525	144.8	154.3	9.5	9.30	97.9	Tensor
18H	30 Mar	1610	154.3	163.8	9.5	9.18	96.6	Tensor, NMCB
19H	30 Mar	1655	163.8	173.3	9.5	9.55	100.5	Tensor
20H	30 Mar	1750	173.3	182.8	9.5	8.70	91.6	Tensor, NMCB
21H	30 Mar	1845	182.8	192.3	9.5	9.70	102.1	Tensor
22H	30 Mar	1935	192.3	201.8	9.5	9.22	97.1	Tensor, NMCB
23H	30 Mar	2200	201.8	208.1	6.3	6.31	100.2	Tensor
24H	30 Mar	2355	208.1	217.6	9.5	9.74	102.5	DO, Tensor
25H	31 Mar	110	217.6	222.6	5.0	2.69	53.8	Tensor
26H	31 Mar	315	222.6	232.1	9.5	9.74	102.5	DO, Tensor
27H	31 Mar	450	232.1	241.6	9.5	9.30	97.9	DO, Tensor
28H	31 Mar	615	241.6	251.1	9.5	9.77	102.8	DO, Tensor
29H	31 Mar	740	251.1	260.6	9.5	9.79	103.1	DO, Tensor
30H	31 Mar	900	260.6	270.1	9.5	10.03	105.6	DO, Tensor
31H	31 Mar	950	270.1	271.6	1.5	1.55	103.3	Tensor
32H	31 Mar	1140	271.6	281.1	9.5	10.06	105.9	DO, Tensor
33H	31 Mar	1235	281.1	284.1	3.0	3.10	103.3	DO, Tensor
34X	31 Mar	1415	284.1	290.3	6.2	4.78	77.1	
35X	31 Mar	1530	290.3	300.0	9.7	6.36	65.6	
36X	31 Mar	1745	300.0	307.1	7.1	4.45	62.7	
37X	31 Mar	1905	307.1	316.7	9.6	5.10	53.1	
38X	31 Mar	2010	316.7	326.4	9.7	6.80	70.1	
39X	31 Mar	2125	326.4	336.0	9.6	5.75	59.9	
40X	31 Mar	2305	336.0	345.6	9.6	4.12	42.9	
Cored totals:					345.6	295.82	85.6	
208-1263B-								
*****Drilled from 0.0 to 46.0 mbsf*****								
1H	2 Apr	445	46.0	55.5	9.5	9.50	100.0	NMCB, APCT
2H	2 Apr	525	55.5	65.0	9.5	8.83	93.0	
3H	2 Apr	615	65.0	74.5	9.5	9.53	100.3	NMCB
4H	2 Apr	705	74.5	84.0	9.5	9.59	101.0	
5H	2 Apr	750	84.0	93.5	9.5	9.50	100.0	NMCB
6H	2 Apr	840	93.5	103.0	9.5	9.69	102.0	
7H	2 Apr	930	103.0	112.5	9.5	9.74	102.5	NMCB
8H	2 Apr	1015	112.5	122.0	9.5	9.80	103.2	
9H	2 Apr	1100	122.0	131.5	9.5	9.87	103.9	NMCB
10H	2 Apr	1150	131.5	141.0	9.5	9.64	101.5	
11H	2 Apr	1225	141.0	150.5	9.5	9.81	103.3	NMCB
12H	2 Apr	1315	150.5	160.0	9.5	10.01	105.4	
13H	2 Apr	1400	160.0	169.5	9.5	9.62	101.3	NMCB
14H	2 Apr	1445	169.5	177.0	7.5	9.07	120.9	
15H	2 Apr	1535	177.0	186.5	9.5	9.84	103.6	NMCB
16H	2 Apr	1620	186.5	196.0	9.5	9.76	102.7	
17H	2 Apr	1710	196.0	196.1	0.1	0.13	130.0	NMCB
*****Drilled from 196.1 to 197.2 mbsf*****								
18H	2 Apr	1815	197.2	201.0	3.8	3.83	100.8	
19H	2 Apr	1920	201.0	204.9	3.9	3.89	99.7	NMCB
20H	2 Apr	2005	204.9	214.4	9.5	9.89	104.1	
21H	2 Apr	2100	214.4	223.9	9.5	10.00	105.3	
22H	2 Apr	2155	223.9	233.4	9.5	9.89	104.1	DO

Table T1 (continued).

Core	Date (2003)	Local time (hr)	Depth (mbsf)		Length (m)		Recovery (%)	Comments
			Top	Bottom	Cored	Recovered		
23H	2 Apr	2250	233.4	242.9	9.5	9.97	105.0	DO
24H	2 Apr	2355	242.9	252.4	9.5	9.77	102.8	DO
25H	3 Apr	50	252.4	261.9	9.5	9.50	100.0	DO
26X	3 Apr	230	261.9	271.1	9.2	9.65	104.9	
27X	3 Apr	340	271.1	280.7	9.6	9.50	99.0	
28X	3 Apr	510	280.7	290.3	9.6	3.58	37.3	
29X	3 Apr	610	290.3	300.0	9.7	9.92	102.3	
30X	3 Apr	730	300.0	309.6	9.6	1.83	19.1	
31X	3 Apr	855	309.6	319.2	9.6	5.48	57.1	
32X	3 Apr	1010	319.2	328.9	9.7	6.96	71.8	
33X	3 Apr	1140	328.9	338.5	9.6	8.16	85.0	
Cored totals:					291.4	275.75	94.6	
208-1263C-								
*****Drilled from 0.0 to 90.0 mbsf*****								
1H	3 Apr	1745	90.0	99.5	9.5	9.86	103.8	Tensor
2H	3 Apr	1835	99.5	109.0	9.5	9.36	98.5	Tensor, NMCB
3H	3 Apr	1920	109.0	118.5	9.5	9.59	101.0	Tensor
*****Drilled from 118.5 to 193.0 mbsf*****								
4H	3 Apr	2255	193.0	202.5	9.5	9.31	98.0	Tensor, NMCB
5H	3 Apr	2355	202.5	212.0	9.5	4.17	43.9	Tensor
6H	4 Apr	215	212.0	221.5	9.5	9.76	102.7	DO, Tensor, NMCB
7H	4 Apr	330	221.5	225.4	3.9	3.85	98.7	Tensor
8H	4 Apr	435	225.4	234.9	9.5	9.65	101.6	DO, Tensor
9H	4 Apr	540	234.9	244.4	9.5	9.96	104.8	DO, Tensor
10H	4 Apr	730	244.4	253.9	9.5	10.00	105.3	DO, Tensor
11H	4 Apr	1050	253.9	263.4	9.5	10.02	105.5	DO, Tensor
12H	4 Apr	1225	263.4	272.9	9.5	9.75	102.6	DO, Tensor
13H	4 Apr	1325	272.9	282.4	9.5	10.08	106.1	DO, Tensor
14H	4 Apr	1425	282.4	285.6	3.2	3.20	100.0	DO, Tensor
15H	4 Apr	1540	285.6	285.7	0.1	0.15	150.0	Tensor
16X	4 Apr	1650	285.7	290.8	5.1	3.35	65.7	
Cored totals:					126.3	122.06	96.6	
208-1263D-								
*****Drilled from 0.0 to 272.0 mbsf*****								
1H	5 Apr	325	272.0	275.2	3.2	3.25	101.6	
2H	5 Apr	455	275.2	281.5	6.3	7.45	118.3	DO
3H	5 Apr	600	281.5	284.3	2.8	2.83	101.1	DO
4H	5 Apr	730	284.3	286.6	2.3	2.32	100.9	DO
Cored totals:					14.6	15.85	108.6	
Totals:					777.9	709.48	91.2	

Notes: NMCB = nonmagnetic core barrel, including cutting shoe (made from Monel). Tensor = brand name for core barrel orientation tool. APCT = Advanced Piston Corer Temperature tool (stainless steel housing is cutting shoe). DO = drillover. See Table T1, p. 106, in the "Leg 208 Summary" chapter.

Table T2. Composite depth scale, Site 1263.

Core	Offset (m)	Depth		Core	Offset (m)	Depth	
		(mbsf)	(mcd)			(mbsf)	(mcd)
208-1263A-				8H	18.34	112.50	130.84
1H	0.00	0.00	0.00	9H	19.95	122.00	141.95
2H	0.41	2.30	2.71	10H	20.78	131.50	152.28
3H	2.12	11.80	13.92	11H	21.78	141.00	162.78
4H	3.83	21.30	25.13	12H	22.68	150.50	173.18
5H	3.85	30.80	34.65	13H	24.57	160.00	184.57
6H	7.25	40.30	47.55	14H	26.12	169.50	195.62
7H	9.11	49.80	58.91	15H	27.35	177.00	204.35
8H	10.71	59.30	70.01	16H	29.69	186.50	216.19
9H	11.77	68.80	80.57	17H	29.69	196.00	225.69
10H	11.79	78.30	90.09	18H	31.11	197.20	228.31
11H	13.17	87.80	100.97	19H	32.60	201.00	233.60
12H	13.73	97.30	111.03	20H	33.71	204.90	238.61
13H	17.53	106.80	124.33	21H	35.92	214.40	250.32
14H	17.75	116.30	134.05	22H	38.33	223.90	262.23
15H	20.52	125.80	146.32	23H	40.47	233.40	273.87
16H	21.89	135.30	157.19	24H	42.29	242.90	285.19
17H	23.02	144.80	167.82	25H	42.95	252.40	295.35
18H	23.94	154.30	178.24	26X	44.12	261.90	306.02
19H	25.47	163.80	189.27	27X	47.38	271.10	318.48
20H	27.77	173.30	201.07	28X	50.83	280.70	331.53
21H	30.34	182.80	213.14	29X	52.56	290.30	342.86
22H	32.34	192.30	224.64	30X	54.30	300.00	354.30
23H	32.55	201.80	234.35	31X	56.03	309.60	365.63
24H	34.65	208.10	242.75	32X	57.76	319.20	376.96
25H	35.85	217.60	253.45	33X	59.51	328.90	388.41
26H	36.85	222.60	259.45	208-1263C-			
27H	40.03	232.10	272.13	1H	13.11	90.00	103.11
28H	42.52	241.60	284.12	2H	14.98	99.50	114.48
29H	43.70	251.10	294.80	3H	18.26	109.00	127.26
30H	45.71	260.60	306.31	4H	32.32	193.00	225.32
31H	46.40	270.10	316.50	5H	33.00	202.50	235.50
32H	48.38	271.60	319.98	6H	33.83	212.00	245.83
33H	51.00	281.10	332.10	7H	34.27	221.50	255.77
34X	51.24	284.10	335.34	8H	36.94	225.40	262.34
35X	52.36	290.30	342.66	9H	39.79	234.90	274.69
36X	54.10	300.00	354.10	10H	41.88	244.40	286.28
37X	55.38	307.10	362.48	11H	43.71	253.90	297.61
38X	57.11	316.70	373.81	12H	45.42	263.40	308.82
39X	58.85	326.40	385.25	13H	47.21	272.90	320.11
40X	60.58	336.00	396.58	14H	50.31	282.40	332.71
208-1263B-				15H	50.31	285.60	335.91
1H	7.31	46.00	53.31	16X	50.83	285.70	336.53
2H	9.41	55.50	64.91	208-1263D-			
3H	11.04	65.00	76.04	1H	46.48	272.00	318.48
4H	12.09	74.50	86.59	2H	48.38	275.20	323.58
5H	14.69	84.00	98.69	3H	50.61	281.50	332.11
6H	15.64	93.50	109.14	4H	50.63	284.30	334.93
7H	16.98	103.00	119.98				

Table T3. Splice tie points.

Hole, core, section, interval (cm)	Depth			Hole, core, section, interval (cm)	Depth	
	(mbsf)	(mcd)			(mbsf)	(mcd)
208-				208-		
1263A-1H-2, 50.0	2.00	2.00	Append to	1263A-2H-1, 0.0	2.30	2.71
1263A-2H-7, 30.0	11.60	12.01	Append to	1263A-3H-1, 0.0	11.80	13.92
1263A-3H-7, 30.0	21.10	23.22	Append to	1263A-4H-1, 0.0	21.30	25.13
1263A-4H-7, 35.0	30.65	34.48	Append to	1263A-6H-1, 0.0	40.30	47.55
1263A-6H-6, 65.0	48.45	55.70	Tie to	1263B-1H-2, 88.5	48.39	55.70
1263B-1H-6, 75.0	54.25	61.56	Tie to	1263A-7H-2, 115.0	52.45	61.56
1263A-7H-6, 10.0	57.40	66.51	Tie to	1263B-2H-2, 10.0	57.10	66.51
1263B-2H-6, 65.0	63.65	73.06	Tie to	1263A-8H-3, 5.0	62.35	73.06
1263A-8H-6, 60.0	67.40	78.11	Tie to	1263B-3H-2, 56.0	67.07	78.11
1263B-3H-5, 110.0	72.10	83.14	Tie to	1263A-9H-2, 106.0	71.37	83.14
1263A-9H-6, 47.5	76.78	88.55	Tie to	1263B-4H-2, 44.5	76.46	88.55
1263B-4H-5, 70.0	81.20	93.29	Tie to	1263A-10H-3, 20.0	81.50	93.29
1263A-10H-7, 10.0	87.40	99.19	Tie to	1263B-5H-1, 50.0	84.50	99.19
1263B-5H-6, 102.5	92.36	107.05	Tie to	1263C-1H-3, 93.5	93.94	107.05
1263C-1H-6, 132.5	98.82	111.93	Tie to	1263B-6H-2, 128.5	96.29	111.93
1263B-6H-6, 135.0	102.35	117.99	Tie to	1263C-2H-3, 51.0	103.01	117.99
1263C-2H-6, 32.5	107.32	122.30	Tie to	1263B-7H-2, 82.5	105.32	122.30
1263B-7H-6, 135.0	111.85	128.83	Tie to	1263C-3H-2, 6.0	110.57	128.83
1263C-3H-4, 35.0	113.85	132.11	Tie to	1263B-8H-1, 126.0	113.77	132.11
1263B-8H-5, 87.5	119.38	137.72	Tie to	1263A-14H-3, 66.0	119.97	137.72
1263A-14H-6, 145.0	123.84	141.59	Append to	1263B-9H-1, 0.0	122.00	141.95
1263B-9H-6, 132.5	130.82	150.77	Tie to	1263A-15H-3, 145.0	130.25	150.77
1263A-15H-7, 10.0	134.60	155.12	Tie to	1263B-10H-2, 133.5	134.34	155.12
1263B-10H-5, 72.5	138.22	159.00	Tie to	1263A-16H-2, 31.0	137.11	159.00
1263A-16H-6, 12.5	142.92	164.81	Tie to	1263B-11H-2, 52.0	143.03	164.81
1263B-11H-4, 145.0	146.95	168.73	Tie to	1263A-17H-1, 91.0	145.71	168.73
1263A-17H-6, 57.5	152.88	175.90	Tie to	1263B-12H-2, 120.5	153.22	175.90
1263B-12H-6, 30.0	157.00	179.68	Tie to	1263A-18H-1, 144.0	155.74	179.68
1263A-18H-5, 130.0	161.60	185.54	Tie to	1263B-13H-1, 96.0	160.97	185.54
1263B-13H-6, 130.0	168.80	193.37	Tie to	1263A-19H-3, 110.0	167.90	193.37
1263A-19H-6, 52.5	171.82	197.29	Tie to	1263B-14H-2, 16.0	171.17	197.29
1263B-14H-5, 110.0	176.60	202.72	Tie to	1263A-20H-2, 15.0	174.95	202.72
1263A-20H-5, 45.0	179.75	207.52	Tie to	1263B-15H-3, 16.0	180.17	207.52
1263B-15H-7, 5.0	186.05	213.40	Tie to	1263A-21H-1, 24.5	183.06	213.40
1263A-21H-6, 105.0	191.35	221.69	Tie to	1263B-16H-4, 100.0	192.00	221.69
1263B-16H-7, 52.5	196.02	225.71	Tie to	1263A-22H-1, 106.0	193.37	225.71
1263A-22H-7, 27.5	201.32	233.66	Tie to	1263B-19H-1, 4.5	201.06	233.66
1263B-19H-3, 7.5	204.08	236.68	Tie to	1263A-23H-2, 83.5	204.13	236.68
1263A-23H-4, 47.5	206.76	239.31	Tie to	1263B-20H-1, 70.0	205.60	239.31
1263B-20H-7, 32.5	214.22	247.93	Tie to	1263A-24H-4, 67.5	213.28	247.93
1263A-24H-7, 25.0	217.25	251.90	Tie to	1263B-21H-2, 7.5	215.98	251.90
1263B-21H-5, 102.5	221.42	257.34	Tie to	1263C-7H-2, 11.0	223.07	257.34
1263C-7H-4, 15.0	225.28	259.55	Tie to	1263A-26H-1, 10.0	222.70	259.55
1263A-26H-7, 35.0	231.95	268.80	Tie to	1263B-22H-5, 56.0	230.47	268.80
1263B-22H-7, 65.0	233.55	271.88	Append to	1263A-27H-1, 0.0	232.10	272.13
1263A-27H-6, 55.0	240.15	280.18	Tie to	1263C-9H-4, 98.5	240.39	280.18
1263C-9H-7, 65.0	244.55	284.34	Tie to	1263A-28H-1, 22.5	241.82	284.34
1263A-28H-3, 77.5	245.38	287.90	Tie to	1263B-24H-2, 121.0	245.61	287.90
1263B-24H-6, 20.0	250.60	292.89	Tie to	1263C-10H-5, 61.0	251.01	292.89
1263C-10H-7, 92.5	253.82	295.70	Tie to	1263A-29H-1, 90.0	252.00	295.70
1263A-29H-5, 120.0	258.30	302.00	Tie to	1263C-11H-3, 138.5	258.29	302.00
1263C-11H-7, 45.0	263.35	307.06	Tie to	1263A-30H-1, 75.0	261.35	307.06
1263A-30H-7, 32.5	269.92	315.63	Tie to	1263C-12H-5, 81.0	270.21	315.63
1263C-12H-8, 32.5	273.14	318.56	Tie to	1263B-27X-1, 7.5	271.18	318.56
1263B-27X-6, 107.5	279.68	327.06	Tie to	1263A-32H-5, 107.5	278.68	327.06
1263A-32H-7, 52.5	281.12	329.50	Tie to	1263D-2H-4, 142.5	281.12	329.50
1263D-2H-5, 125.0	282.45	330.83	Append to	1263B-28X-1, 0.0	280.70	331.53
1263B-28X-2, 55.0	282.75	333.58	Tie to	1263C-14H-1, 86.0	283.27	333.58
1263C-14H-2, 142.5	285.32	335.63	Tie to	1263D-4H-1, 70.0	285.00	335.63
1263D-4H-2, 105.0	286.35	336.98	Tie to	1263C-16X-1, 43.0	286.15	336.98
1263C-16X-3, 57.5	288.78	339.61				

Note: This table is also available in [ASCII](#).

Table T4. Lithostratigraphic subdivisions, Site 1263.

Unit/ subunit	Unit boundary depth (mcd)	Hole 1263A						Hole 1263B						Hole 1263C					
		Core, section, interval (cm)		Depth (mbsf)		Depth (mcd)		Core, section, interval (cm)		Depth (mbsf)		Depth (mcd)		Core, section, interval (cm)		Depth (mbsf)		Depth (mcd)	
		Top	Base	Top	Base	Top	Base	Top	Base	Top	Base	Top	Base	Top	Base	Top	Base	Top	Base
IA	99.1	1H-1	10H-6	0.0	87.3	0.0	99.1	1H-1	5H-1, 40	46.0	84.4	53.3	99.1	—	—	—	—	—	—
IB	318.0	10H-7	31H-CC	87.3	271.6	99.1	318.0	5H-1, 40	26X-CC	84.4	271.6	99.1	315.7	1H-1	12H-7, 50	90.0	272.6	103.1	318.0
IC	(400.7)*	32H-1	40X-CC	271.6	340.12	318.0	400.7	27X-1	33X-CC	271.1	337.1	318.5	396.6	12H-7, 50	16X-CC	272.6	289.1	318.0	339.9

Notes: Bold intervals and depths define the unit boundaries; other intervals are recognized as part of units but do not contain the unit boundaries. — = lithostratigraphic unit not recovered. * = base of cored unit.

Unit/ subunit	Unit boundary depth (mcd)	Hole 1262D						Description
		Core, section, interval (cm)		Depth (mbsf)		Depth (mcd)		
		Top	Base	Top	Base	Top	Base	
IA	99.1	—	—	—	—	—	—	Foraminifer-bearing nannofossil ooze, nannofossil ooze
IB	318.0	—	—	—	—	—	—	Nannofossil ooze, clay-bearing nannofossil ooze, chalky nannofossil ooze, foraminifer-bearing nannofossil ooze
IC	(400.7)*	1H-1	4H-CC	272.0	286.6	318.5	337.3	Nannofossil ooze, chalky nannofossil ooze

Table T5. Stratigraphic positions of selected calcareous nannofossil datums, Site 1263. (See table notes. Continued on next page.)

Datum	Age (Ma)		Top of sample interval			Base of sample interval			Average (mcd)
	Youngest	Oldest	Core, section, interval (cm)	Depth		Core, section, interval (cm)	Depth		
				(mbsf)	(mcd)		(mbsf)	(mcd)	
			208-1263A-			208-1263A-			
T <i>Discoaster pentaradiatus</i>	2.52	2.52	1H-CC	2.29	2.29	2H-CC	11.66	12.07	7.18
T <i>Discoaster surculus</i>	2.63	2.63	1H-CC	2.29	2.29	2H-CC	11.66	12.07	7.18
T <i>Amaurolithus</i> spp.	4.56	4.56	2H-CC	11.66	12.07	3H-CC	21.17	23.29	17.68
CN9a/NN11 assemblage	7.39	8.28	4H-1, 120	22.50	26.33	4H-2, 50	23.30	27.13	26.73
B <i>Sphenolithus ciperoensis</i>	27.55	27.55	6H-1, 45	40.75	48.00	6H-1, 145	41.75	49.00	48.50
B <i>Sphenolithus distentus</i>	30.32	30.32	6H-CC	49.10	56.35	7H-CC	59.61	68.72	62.54
T <i>Sphenolithus pseudoradians</i>			6H-CC	49.10	56.35	7H-CC	59.61	68.72	62.54
T <i>Reticulofenestra umbilicus</i> >14 µm	31.7	31.7	8H-4, 140	65.20	75.91	8H-5, 45	65.75	76.46	76.19
T <i>Isthmolithus recurvus</i>	32.7	32.7	9H-4, 45	73.75	85.52	9H-4, 140	74.70	86.47	86.00
T <i>Ericsonia formosa</i>	32.9	32.9	9H-4, 45	73.75	85.52	9H-4, 140	74.70	86.47	86.00
B <i>Ericsonia obruta</i> increase	33.7	33.7	10H-3, 140	82.70	94.49	10H-4, 45	83.25	95.04	94.77
T <i>Discoaster saipanensis</i>	34.0	34.0	11H-2, 140	90.70	103.87	11H-3, 36	91.16	104.33	104.10
B <i>Isthmolithus recurvus</i>	36.6	36.6	12H-4, 140	102.57	116.30	12H-5, 45	103.12	116.85	116.58
B <i>Dictyococcites bisectus</i>	38.5	38.5	14H-1, 140	117.70	135.45	14H-2, 60	118.40	136.15	135.80
B <i>Dictyococcites scrippsae</i>	40.3	40.3	14H-5, 10	120.99	138.74	14H-CC	124.05	141.80	140.27
T <i>Nannotetrina</i> spp.	42.3	42.3	15H-CC	135.23	155.75	16H-1, 45	135.75	157.64	156.70
B <i>Reticulofenestra umbilicus</i> >14 µm	42.5	42.5	16H-2, 45	137.25	159.14	16H-2, 140	138.20	160.09	159.62
B <i>Nannotetrina</i> spp.	47.8	47.8	21H-1, 40	183.20	213.54	21H-1, 140	184.20	214.54	214.04
T <i>Discoaster lodoensis</i>	48.0	48.0	21H-2, 40	184.70	215.04	21H-2, 140	185.70	216.04	215.54
B <i>Rhabdosphaera inflata</i>	48.5	48.5	21H-7, 55	192.35	222.69	21H-CC	192.40	222.74	222.72
B <i>Discoaster sublodoensis</i>	49.3	49.3	22H-3, 130	196.34	228.68	22H-4, 40	196.94	229.28	228.98
T <i>Tribrachiatus orthostylus</i>	51.0	51.0	24H-3, 140	212.50	247.15	24H-4, 45	213.05	247.70	247.43
B <i>Discoaster lodoensis</i>	52.4	52.4	27H-3, 45	235.55	275.58	27H-3, 140	236.50	276.53	276.06
B <i>Towieus crassus</i>	51.5	51.5	27H-7, 60	241.20	281.23	28H-1, 80	242.40	284.92	283.08
T <i>Discoaster multiradiatus</i>	53.0	53.0	28H-2, 80	243.90	286.42	28H-3, 80	245.40	287.92	287.17
B <i>Sphenolithus radians</i>	53.3	53.3	28H-3, 80	245.40	287.92	28H-4, 80	246.90	289.42	288.67
B <i>Tribrachiatus orthostylus</i>	53.4	53.4	29H-1, 50	251.60	295.30	29H-1, 140	252.50	296.20	295.75
T <i>Fasciculithus</i> spp.			32H-2, 60	273.70	322.08	32H-4, 60	276.70	325.08	323.58
B <i>Discoaster diastypus</i>	53.9	53.9	32H-6, 130	280.40	328.78	32H-CC	281.61	329.99	329.39
Increase <i>Zygrhaliolithus bijugatus</i>			33H-2, 110	283.70	334.70	33H-2, 126	283.86	334.86	334.78
B <i>Rhomboaster</i> spp.			34X-1, 10	284.20	335.44	34X-1, 30	284.40	335.64	335.54
B <i>Discoaster multiradiatus</i>	56.2	56.2	36X-3, 40	303.40	357.50	36X-3, 115	304.15	358.25	357.88
B <i>Discoaster nobilis</i>	56.5	56.5	37X-3, 86	310.96	366.34	37X-4, 70	311.80	367.18	366.76
B <i>Heliolithus riedelii</i>	57.3	57.3	39X-2, 140	329.30	388.15	39X-3, 40	329.80	388.65	388.40
B <i>Discoaster mohleri</i>	57.5	57.5	39X-3, 140	330.80	389.65	39X-4, 70	331.60	390.45	390.05
B <i>Heliolithus kleinpellii</i>	58.2	58.2	40X-3, 65	339.65	400.23	40X-CC	340.07	400.65	400.44
B <i>Sphenolithus anarrhopus</i>	58.4	58.4	40X-3, 65	339.65	400.23	40X-CC	340.07	400.65	400.44
			208-1263B-			208-1263B-			
B <i>Sphenolithus distentus</i>	30.4	30.4	1H-CC	55.40	62.71	2H-1, 5	55.55	64.96	63.84
T <i>Sphenolithus pseudoradians</i>			2H-5, 40	61.90	71.31	2H-5, 140	62.90	72.31	71.81
T <i>Reticulofenestra umbilicus</i> >14 µm	42.5	42.5	3H-CC	74.43	85.47	4H-CC	84.04	96.13	90.80
T <i>Ericsonia formosa</i>	32.9	32.9	3H-CC	74.43	85.47	4H-CC	84.04	96.13	90.80
T <i>Discoaster saipanensis</i>	34.0	34.0	5H-4, 66	88.99	103.68	5H-5, 40	90.23	104.92	104.30
T <i>Chiasmolithus grandis</i>	37.1	37.1	7H-3, 60	106.60	123.58	7H-4, 40	107.90	124.88	124.23
B <i>Dictyococcites bisectus</i>	38.5	38.5	8H-1, 40	112.90	131.24	8H-1, 120	113.70	132.04	131.64
T <i>Nannotetrina</i> spp.	42.3	42.3	9H-CC	131.77	151.72	10H-CC	141.04	161.82	156.77
B <i>Reticulofenestra umbilicus</i> >14 µm	42.5	42.5	11H-CC	150.76	172.54	12H-CC	160.46	183.14	177.84
T <i>Nannotetrina fulgens</i>	43.4	43.4	11H-3, 80	144.80	166.58	11H-4, 80	146.30	168.08	167.33
T <i>Chiasmolithus gigas</i>	44.0	44.0	12H-1, 40	150.90	173.58	12H-1, 140	151.90	174.58	174.08
B <i>Chiasmolithus gigas</i>	46.1	46.1	13H-3, 120	164.21	188.77	13H-4, 40	164.90	189.47	189.12
B <i>Nannotetrina fulgens</i>	47.0	47.0	14H-3, 40	172.90	199.02	14H-3, 120	173.70	199.82	199.42
B <i>Discoaster sublodoensis</i>	49.3	49.3	13H-CC	169.52	194.09	14H-CC	178.52	204.64	199.37
T <i>Discoaster lodoensis</i>	48.0	48.0	14H-CC	178.52	204.64	15H-CC	186.79	214.14	209.39
T <i>Tribrachiatus orthostylus</i>	51.0	51.0	19H-CC	204.84	237.44	20H-CC	214.74	248.45	242.95
B <i>Discoaster lodoensis</i>	52.4	52.4	22H-CC	233.74	272.07	23H-CC	243.32	283.79	277.93
T <i>Discoaster multiradiatus</i>	53.0	53.0	23H-CC	243.32	283.79	24H-CC	252.62	294.91	289.35
B <i>Sphenolithus radians</i>	53.3	53.3	23H-CC	243.32	283.79	24H-CC	252.62	294.91	289.35
B <i>Tribrachiatus orthostylus</i>	53.4	53.4	23H-CC	243.32	283.79	24H-CC	252.62	294.91	289.35
T <i>Fasciculithus</i> spp.			26X-CC	271.50	315.62	27X-CC	280.55	327.93	321.78
B <i>Rhomboaster</i> spp.			28X-CC	284.26	335.09	29X-1, 1	290.30	342.86	338.98
B <i>Discoaster multiradiatus</i>	56.2	56.2	30X-CC	301.78	356.08	31X-CC	315.03	371.06	363.57
B <i>Heliolithus riedelii</i>	57.3	57.3	31X-CC	315.03	371.06	32X-CC	326.11	383.87	377.47
B <i>Discoaster mohleri</i>	57.5	57.5	31X-CC	315.03	371.06	32X-CC	326.11	383.87	377.47
B <i>Heliolithus kleinpellii</i>	58.2	58.2	32X-CC	326.11	383.87	33X-CC	336.98	396.49	390.18

Table T5 (continued).

Datum	Age (Ma)		Top of sample interval			Base of sample interval			Average (mcd)
	Youngest	Oldest	Core, section, interval (cm)	Depth		Core, section, interval (cm)	Depth		
				(mbsf)	(mcd)		(mbsf)	(mcd)	
T <i>Discoaster lodoensis</i>	48.0	48.0	208-1263C- 3H-CC	118.54	136.80	208-1263C- 4H-CC	202.26	234.58	185.69
T <i>Tribraehiatus orthostylus</i>	51.0	51.0	5H-CC	206.62	239.62	6H-CC	221.66	255.49	247.56
B <i>Discoaster lodoensis</i>	52.4	52.4	8H-CC	234.95	271.89	9H-CC	244.81	284.60	278.25
T <i>Discoaster multiradiatus</i>	53.0	53.0	9H-CC	244.81	284.60	10H-CC	254.35	296.23	290.42
B <i>Sphenolithus radians</i>	53.3	53.3	9H-CC	244.81	284.60	10H-CC	254.35	296.23	290.42
B <i>Tribraehiatus orthostylus</i>	53.4	53.4	10H-CC	254.35	296.23	11H-CC	263.87	307.58	301.91
T <i>Fasciculithus</i> spp.			12H-CC	272.81	318.23	13H-CC	282.93	330.14	324.19
B <i>Rhomboaster</i> spp.			14H-2, 92	284.87	335.13	14H-2, 110	285.00	335.31	335.22
			208-1263D- 1H-CC	275.20	321.68	208-1263D- 2H-CC	282.60	330.98	326.33
B <i>Rhomboaster</i> spp.			3H-CC	284.01	334.62	4H-CC	286.49	337.12	335.87

Note: T = top, B = bottom.

Table T7. Stratigraphic positions of selected planktonic foraminiferal datums, Site 1263.

Datum	Age (Ma)		Top of sample interval			Base of sample interval			Average (mcd)
	Youngest	Oldest	Hole, core, section, interval (cm)	Depth		Hole, core, section, interval (cm)	Depth		
				(mbsf)	(mcd)		(mbsf)	(mcd)	
			208-			208-			
T <i>Globigerinoides obliquus</i>	1.30	1.30	1263A-1H-CC	2.29	2.29	1263A-2H-CC	11.66	12.07	7.18
T <i>Globigerina apertura</i>	1.68	1.68	1263A-1H-CC	2.29	2.29	1263A-3H-CC	11.66	12.07	7.18
B <i>Globorotalia truncatulinoides</i>	2.03	2.03	1263A-1H-CC	2.29	2.29	1263A-2H-CC	11.66	12.07	7.18
T <i>Globoturbotalia woodi</i>	2.30	2.30	1263A-1H-CC	2.29	2.29	1263A-2H-CC	11.66	12.07	7.18
T <i>Sphaeroidinellopsis seminulina</i>	3.18	3.18	1263A-2H-CC	11.66	12.07	1263A-3H-CC	21.17	23.29	17.68
B <i>Globorotalia tosaensis</i>	3.35	3.35	1263A-2H-CC	11.66	12.07	1263A-3H-CC	21.17	23.29	17.68
T <i>Neogloboquadrina acostaensis</i>	3.83	3.83	1263A-2H-CC	11.66	12.07	1263A-3H-CC	21.17	23.29	17.68
T <i>Globorotalia plesiotumida</i>	4.15	4.15	1263A-2H-CC	11.66	12.07	1263A-3H-CC	21.17	23.29	17.68
B <i>Globorotalia crassaformis</i> s.l.	4.31	4.31	1263A-3H-CC	21.17	23.29	1263A-4H-CC	30.85	34.68	28.99
B <i>Sphaeroidinella dehiscens</i> s.l.	4.94	4.94	1263A-3H-CC	21.17	23.29	1263A-4H-CC	30.85	34.68	28.99
T <i>Subbotina angiporooides</i>	29.67	29.67	1263B-1H-CC	55.40	62.71	1263A-7H-CC	59.61	68.72	65.72
T " <i>Globigerina</i> " <i>ampliapertura</i>	30.12	30.12	1263A-7H-CC	59.61	68.72	1263B-2H-CC	64.28	73.69	71.21
B <i>Paragloborotalia opima</i>	30.54	30.54	1263A-6H-CC	49.10	56.35	1263B-1H-CC	55.40	62.71	59.53
T <i>Pseudohastigerina</i> spp.	32.00	32.00	1263A-7H-CC	59.61	68.72	1263B-2H-CC	64.28	73.69	71.21
T <i>Hantkenina</i> spp.	33.70	33.70	1263A-10H-CC	88.18	99.97	1263B-5H-CC	93.44	108.13	104.05
T <i>Turborotalia cerroazulensis</i>	33.80	33.80	1263B-4H-CC	84.04	96.13	1263A-10H-CC	88.18	99.97	98.05
T <i>Globigerinatheka index</i>	34.30	34.30	1263A-10H-CC	88.18	99.97	1263B-5H-CC	93.44	108.13	104.05
T <i>Globigerinatheka semiinvoluta</i>	35.30	35.30	1263A-11H-CC	96.62	109.79	1263A-12H-CC	104.07	117.80	113.80
T <i>Acarinina primitiva</i>	39.00	39.00	1263B-6H-CC	103.09	118.73	1263B-7H-CC	112.69	129.67	124.20
T <i>Morozovella aragonensis</i>	43.60	43.60	1263B-11H-CC	150.76	172.54	1263A-17H-CC	154.00	177.02	174.78
T <i>Morozovella formosa</i>	50.80	50.80	1263A-25H-CC	220.24	256.09	1263B-21H-CC	224.35	260.27	258.18
B <i>Morozovella aragonensis</i>	52.76	52.76	1263B-22H-CC	233.74	272.07	1263A-27H-CC	241.35	281.38	276.73
T <i>Morozovella aequa</i>	52.89	52.89	1263A-27H-CC	241.35	281.38	1263B-23H-CC	243.32	283.79	282.59
B <i>Morozovella formosa</i>	54.00	54.00	1263A-30H-CC	270.58	316.29	1263A-31H-CC	271.60	318.00	317.15
T <i>Subbotina triangularis</i>	54.07	54.07	1263B-27X-CC	280.55	327.93	1263A-32H-CC	281.61	329.99	328.96
B <i>Subbotina velascoensis</i>	54.17	54.17	1263B-27X-CC	280.55	327.93	1263A-32H-CC	281.61	329.99	328.96
T <i>Morozovella velascoensis</i>	54.31	54.31	1263A-31H-CC	271.60	318.00	1263A-32H-CC	281.61	329.99	324.00
B <i>Igorina broedermanni</i>	54.70	54.70	1263B-28X-CC	284.26	335.09	1263A-33H-CC	284.15	335.15	335.12
T <i>Stensioeina beccariiiformis</i> *	55.00	55.00	1263A-34X-1, 27-28	284.37	335.61	1263A-34X-1, 37-38	284.47	335.71	335.66
B <i>Globanomalina australiformis</i>	55.50	55.50	1263A-32H-CC	281.61	329.99	1263B-28X-CC	284.26	335.09	332.54
T <i>Globanomalina pseudomenardii</i>	55.90	55.90	1263A-35X-CC	296.61	348.97	1263B-29X-CC	300.17	352.73	350.85
B <i>Morozovella subbotinae</i>	55.90	55.90	1263B-30X-CC	301.78	356.08	1263A-37X-CC	312.15	367.53	361.81
T <i>Acarinina mckannai</i>	56.30	56.30	1263A-35X-CC	296.61	348.97	1263B-29X-CC	300.17	352.73	350.85
B <i>Morozovella aequa</i>	56.50	56.50	1263B-30X-CC	301.78	356.08	1263A-37X-CC	312.15	367.53	361.81
B <i>Acarinina soldadoensis</i>	56.50	56.50	1263B-31X-CC	315.03	371.06	1263A-38X-CC	323.45	380.56	375.81

Notes: T = top, B = bottom. * = benthic foraminiferal datum level.

Table T8. Stratigraphic ranges and relative abundances for selected planktonic foraminifer taxa, Site 1263.
(This table is available in an [oversized format](#).)

Table T9. Occurrence of selected benthic foraminifer taxa, Site 1263. (This table is available in an [oversized format](#).)

Table T10. Magnetostratigraphic age-depth tie points, Site 1263.

Chron	Age (Ma)		Top			Bottom		
	1	2	Hole, core, section, interval (cm)	Depth		Hole, core, section, interval (cm)	Depth	
				(mbsf)	(mcd)		(mbsf)	(mcd)
			208-			208-		
C12n (y)	30.476	30.476	1263A-7H-3, 50	53.30	62.41	1263B-2H-1, 85	56.35	65.76
C12n (o)	30.939	30.939	1263A-7H-6, 145	58.75	67.86	1263A-8H-1, 55	59.85	70.56
C13n (y)	33.058	33.058	1263A-9H-3, 5	71.85	83.62	1263B-4H-2, 5	76.05	88.14
C13n (o)	33.545	33.545	1263A-9H-7, 35	77.65	89.42	1263B-4H-4, 65	79.65	91.74
C19n (y)	41.257	41.257	1263B-9H-4, 135	127.85	147.80	1263A-15H-2, 40	127.70	148.22
C19n (o)	41.521	41.521	1263B-9H-5, 125	129.25	149.20	1263A-15H-3, 50	129.30	149.82

Notes: o = old end of chron, y = young end of chron. 1 = ages as in Lourens et al. (in press), 2 = ages as in Cande and Kent (1995).

Table T11. Composition of headspace gases, Hole 1263A.

Core, section, interval (cm)	Depth (mcd)	C ₁ (ppm)
208-1263A-		
2H-6, 0-5	10.2	1.9
3H-6, 0-5	21.4	1.8
4H-6, 0-5	32.6	1.8
6H-6, 0-5	55.1	1.8
7H-6, 0-5	66.4	1.8
8H-6, 0-5	77.5	1.9
9H-6, 0-5	88.1	1.8
10H-6, 0-5	97.6	1.8
11H-6, 0-5	108.5	1.8
12H-5, 0-5	116.4	1.8
14H-6, 0-5	140.1	1.8
15H-6, 0-5	153.8	1.8
16H-6, 0-5	164.7	1.8
17H-6, 0-5	175.3	1.7
18H-5, 0-5	184.2	1.8
19H-6, 0-5	196.8	2.0
20H-5, 0-5	207.1	1.8
21H-5, 0-5	219.1	1.8
22H-6, 0-5	231.9	2.0
23H-3, 0-5	237.3	1.9
24H-6, 0-5	250.6	1.9
25H-2, 0-5	255.0	2.0
26H-6, 0-5	267.0	1.7
27H-6, 0-5	279.6	1.8
28H-6, 0-5	291.6	1.9
29H-6, 0-5	302.3	1.8
30H-6, 0-5	313.8	1.9
32H-6, 0-5	327.5	2.0
35X-4, 0-5	347.2	2.2
36X-3, 0-5	357.1	2.0
37X-4, 0-5	366.5	2.3
38X-4, 0-5	378.3	2.6
39X-3, 0-5	388.3	2.8
40X-2, 0-5	398.1	2.5

Table T12. Interstitial water analyses, Site 1263.

Hole, core, section, interval (cm)	Depth (mcd)	pH	Alkalinity (mM)	Salinity	Cl (mM)	SO ₄ (mM)	Na (mM)	Mg (mM)	Ca (mM)	K (mM)	B (μM)	Fe (μM)	Mn (μM)	Li (μM)	Ba (μM)	Sr (μM)	Si (μM)	Zn (μM)	
208-																			
1263A-2H-5, 145-150	10.2	7.55	2.88	35.0	554	23.3	479	54.9	12.3	11.0	462	0.11	0.23	28.6	1.58	124	262	4.22	
1263A-3H-5, 145-150	21.4	7.51	2.94	35.5	563	26.3	484	55.0	12.1	10.9	473	0.21	0.26	27.0	0.26	142	269	2.01	
1263A-4H-5, 140-150	32.5	7.42	2.91	35.5	561	23.6	476	54.3	12.7	10.9	491	0.22	0.08	27.6	1.83	154	267	1.74	
1263A-6H-5, 140-150	55.0	7.48	5.93	35.0	561	26.4	466	52.7	12.9	10.2	502	0.26	0.22	28.6	1.88	163	281	0.55	
1263A-7H-5, 140-150	66.3	7.50	2.93	34.5	554	25.9	478	52.8	13.1	10.3	508	0.15	0.21	30.2	0.19	171	296	1.80	
1263A-8H-5, 140-150	77.4	7.43	2.93	34.5	476	25.4	472	52.9	13.2	10.5	506	0.21	0.25	29.3	2.41	178	335	2.29	
1263A-9H-5, 140-150	88.0	7.48	3.29	35.0	563	26.0	471	52.5	13.7	10.8	508	0.19	1.08	30.4	0.50	179	358	1.38	
1263A-10H-5, 140-150	97.5	7.45	2.09	35.0	545	25.6	478	53.1	14.0	10.5	512	0.04	0.64	29.8	1.50	184	358	2.31	
1263A-11H-5, 140-150	108.4	7.48	3.38	34.5	560	25.5	478	50.8	12.0	10.7	528	0.13	0.55	31.8	0.28	192	405	0.31	
1263A-14H-5, 140-150	140.0	7.48	2.72	35.0	558	26.2	472	51.1	14.2	10.7	492	0.16	2.97	30.7	1.54	194	453	3.71	
1263A-15H-5, 140-150	153.7	7.31	2.93	34.0	556	25.5	463	50.6	14.8	10.5	484	0.08	3.92	31.2	0.40	213	578	2.00	
1263A-16H-5, 140-150	164.6	7.33	2.94	34.0	561	25.2	474	50.6	15.5	10.6	493	0.02	5.16	31.4	0.27	215	646	2.15	
1263A-17H-5, 140-150	175.2	7.41	3.18	35.0	565	25.2	481	50.1	15.8	10.9	502	0.00	5.55	33.2	0.23	212	673	4.32	
1263A-18H-4, 140-150	184.1	7.43	2.95	35.0	564	25.3	476	50.7	15.9	10.7	472	0.02	5.85	32.7	0.27	221	723	0.69	
1263A-19H-5, 140-150	196.7	7.50	2.92	34.0	568	25.6	477	49.8	15.9	10.6	498	0.00	6.85	33.5	0.23	231	868	0.00	
1263A-20H-4, 140-150	207.0	7.49	2.92	35.0	565	25.4	470	50.0	16.5	10.3	485	0.24	7.15	34.5	0.27	231	900	2.12	
1263A-21H-4, 140-150	219.0	7.29	2.94	35.0	566	25.1	468	49.2	16.3	10.1	466	0.94	7.40	33.5	2.06	238	936	0.00	
1263A-22H-5, 140-150	231.8	7.32	2.94	34.5	566	25.5	472	50.5	16.9	10.2	463	0.11	7.82	32.7	0.30	241	1033	0.00	
1263A-24H-5, 140-150	250.2	7.70	2.93	34.6	566	24.9	474	48.2	17.2	10.1	477	0.00	6.23	33.7	2.55	247	1074	0.00	
1263A-26H-5, 140-150	266.9	7.52	2.99	35.0	572	25.3	482	50.5	18.5	10.0	460	0.00	6.01	34.3	0.33	250	963	0.71	
1263A-27H-5, 140-150	279.5	7.39	3.34	35.0	572	24.6	476	46.7	17.2	9.6	495	0.00	5.78	35.0	0.34	252	1074	0.00	
1263B-23H-5, 140-150	281.3	7.41	ND	35.0	564	25.5	481	48.3	17.9	9.9	484	0.03	5.59	34.5	0.94	251	1072	0.00	
1263A-28H-5, 140-150	291.5	7.46	3.06	34.5	559	24.2	477	49.0	18.8	10.0	489	0.05	5.67	35.1	3.29	259	1093	0.15	
1263B-24H-5, 140-150	292.6	7.44	3.30	35.0	564	26.3	481	49.5	17.8	9.8	470	0.00	5.41	34.8	0.28	250	1059	0.00	
1263B-25H-5, 140-150	302.8	7.3	3.26	35.0	560	29.4	476	49.3	15.2	10.3	491	0.62	5.40	36.1	0.32	260	1160	0.61	
1263B-26X-5, 140-150	313.4	7.36	3.10	35.0	561	26.2	472	47.9	18.2	9.9	476	0.08	4.57	35.6	2.35	256	1126	0.56	
1263A-35X-3, 140-150	347.1	7.44	3.67	34.0	571	27.9	482	49.3	18.6	9.7	467	0.38	2.32	36.6	0.42	257	1190	0.00	
1263A-36X-2, 140-150	357.0	7.53	2.86	35.0	555	26.8	486	48.2	19.4	9.6	465	2.80	1.40	36.4	0.37	243	1209	1.29	
1263A-37X-3, 90-100	366.4	7.44	2.83	35.0	571	27.5	484	47.4	19.1	9.6	452	2.23	1.22	35.2	0.35	251	1273	0.00	
1263A-38X-3, 140-150	378.2	7.49	3.26	35.0	566	26.1	481	46.9	20.5	9.3	459	3.83	1.04	38.4	0.38	238	1498	0.41	

Note: ND = not determined.

Table T13 (continued).

Core, section, interval (cm)	Depth (mcd)	Inorganic carbon (wt%)	CaCO ₃ (wt%)	Total carbon (wt%)	Organic carbon (wt%)
14H-2, 60-60	334.81	9.6	80.2		
14H-2, 70-70	334.91	9.1	75.7		
14H-2, 76-76	334.97	9.5	78.9		
14H-2, 88-88	335.09	7.2	59.9		
14H-2, 94-94	335.15	7.3	61.1		
14H-2, 100-100	335.21	6.6	54.6		
14H-2, 104-104	335.25	6.5	54.0		
14H-2, 108-108	335.29	5.9	49.5		
14H-2, 112-112	335.33	5.7	47.5		
14H-2, 116-116	335.37	5.7	47.7		
14H-2, 120-120	335.41	5.5	45.6		
14H-2, 124-124	335.45	5.2	43.7		
14H-2, 130-130	335.51	3.8	31.7		
14H-2, 132-132	335.53	3.9	32.5		
14H-2, 134-134	335.55	4.9	40.4		
14H-2, 136-136	335.57	5.1	42.2		
14H-2, 138-138	335.59	4.3	35.9		
14H-2, 140-140	335.61	1.9	15.8		
14H-2, 142-142	335.63	1.9	15.7		
14H-2, 144-144	335.65	0.2	1.3		
14H-2, 146-146	335.67	0.3	2.6		
14H-2, 148-148	335.69	0.5	4.2		
14H-2, 149-149	335.70	8.9	73.7		
14H-CC, 1-1	335.72	10.1	83.9		
14H-CC, 2-2	335.73	10.0	83.5		
14H-CC, 3-3	335.74	10.4	86.6		
14H-CC, 5-5	335.76	10.6	88.4		
14H-CC, 7-7	335.78	10.5	87.5		
14H-CC, 9-9	335.80	10.7	89.0		
14H-CC, 11-11	335.82	10.5	87.1		
14H-CC, 13-13	335.84	10.6	88.2		
14H-CC, 15-15	335.86	10.6	88.5		
14H-CC, 17-17	335.88	10.5	87.2		

Table T14. Breakdown of logging operations, Hole 1263A.

Date (Apr 2003)	Local time (hr)	Operations
1	0230	Hole preparation complete, rig up wireline
	0515	Run into hole with triple combo (HNGS-APS-HLDS-DIT-TAP)
	0630	Uplog with triple combo at 900 ft/hr from total depth (345 mbsf)
	0800	Lockable flapper valve problem—pumping
	1000	Pull tools out of hole and rig down
	1200	Rig up FMS-sonic
	1300	Run into hole with FMS-sonic (SGT-DSI-GPIT-FMS)
	1400	Cannot pass bridge at 159 mbsf
	1500	Pull tools out of hole and wiper trip
	1830	Run into hole with FMS-sonic (SGT-DSI-GPIT-FMS)
	2230	Uplog with FMS-sonic at 500 ft/hr from bridge at 172 mbsf
2	2250	Pull tools out of hole and rig down
	0030	End of logging operations

Notes: Drillers total depth = 3073.9 mbrf, water depth = 2728 m, initial end of pipe = 85.0 mbsf, final end of pipe = 90.0 mbsf. HNGS = Hostile Environment Natural Gamma Ray Sonde, APS = Accelerator Porosity Sonde, HLDS = Hostile Environment Litho-Density Sonde, DIT = Dual Induction Tool, TAP = Temperature/Acceleration/Pressure tool, FMS = Formation MicroScanner, SGT = Scintillation Gamma Ray Tool, DSI = Dipole Sonic Imager tool, GPIT = General Purpose Inclination Tool.

Table T15. Age-depth control points, Site 1263.

	Datum	Type	Upper depth (mcd)	Lower depth (mcd)	Minimum age (Ma)	Maximum age (Ma)
T	<i>Globigerinoides obliquus</i>	PF	2.29	12.07	1.3	1.3
T	<i>Globigerina apertura</i>	PF	2.29	12.07	1.68	1.68
B	<i>Globorotalia truncatulinoides</i>	PF	2.29	12.07	2.03	2.03
T	<i>Globoturborotalia woodi</i>	PF	2.29	12.07	2.3	2.3
T	<i>Sphaeroidinellopsis seminulina</i>	PF	12.07	23.29	3.18	3.18
B	<i>Globorotalia tosaensis</i>	PF	12.07	23.29	3.35	3.35
T	<i>Neogloboquadrina acostaensis</i>	PF	12.07	23.29	3.83	3.83
T	<i>Globorotalia plesiotumida</i>	PF	12.07	23.29	4.15	4.15
B	<i>Globorotalia crassaformis</i> s.l.	PF	23.29	34.68	4.31	4.31
B	<i>Sphaeroidinella dehiszens</i> s.l.	PF	23.29	34.68	4.94	4.94
B	<i>Sphenolithus ciperoensis</i>	CN	48.00	49.00	27.55	27.55
B	<i>Paragloborotalia opima</i>	PF	56.35	62.71	30.54	30.54
B	<i>Sphenolithus distentus</i>	CN	56.35	68.72	30.32	30.32
	C12n (y)	PMAG	62.41	65.76	30.476	30.476
T	<i>Subbotina angiporoides</i>	PF	62.71	68.72	29.67	29.67
	C12n (o)	PMAG	67.86	70.56	30.939	30.939
T	" <i>Globigerina</i> " " <i>ampliapertura</i> "	PF	68.72	73.69	30.12	30.12
T	<i>Pseudohastigerina</i> spp.	PF	68.72	73.69	32	32
T	<i>Reticulofenestra umbilicus</i> >14 µm	CN	75.91	76.46	31.7	31.7
	C13n (y)	PMAG	83.62	88.14	33.058	33.058
T	<i>Ericsonia formosa</i>	CN	85.52	86.47	32.9	32.9
	C13n (o)	PMAG	89.42	91.74	33.545	33.545
	Increase <i>Ericsonia obruta</i>	CN	94.49	95.04	33.7	33.7
T	<i>Turborotalia cerroazulensis</i>	PF	96.13	99.97	33.8	33.8
T	<i>Hantkenina</i> spp.	PF	99.97	108.13	33.7	33.7
T	<i>Globigerinatheka index</i>	PF	99.97	108.13	34.3	34.3
T	<i>Discoaster saipanensis</i>	CN	103.87	104.33	34	34
T	<i>Globigerinatheka semiinvoluta</i>	PF	109.79	117.80	35.3	35.3
B	<i>Istmolithus recurvus</i>	CN	116.30	116.85	36.6	36.6
T	<i>Acarinina primitiva</i>	PF	118.73	129.67	39	39
T	<i>Chiasmolithus grandis</i>	CN	123.58	124.88	37.1	37.1
B	<i>Dictyococcites bisectus</i>	CN	135.45	136.15	38.5	38.5
B	<i>Dictyococcites scrippsae</i>	CN	138.74	141.80	40.3	40.3
	C19n (y)	PMAG	147.80	148.22	41.257	41.257
	C19n (o)	PMAG	149.20	149.82	41.521	41.521
T	<i>Nannotetrina</i> spp.	CN	155.75	157.64	42.3	42.3
T	<i>Reticulofenestra umbilicus</i> >14 µm	CN	159.14	160.09	42.5	42.5
T	<i>Morozovella aragonensis</i>	PF	172.54	177.02	43.6	43.6
T	<i>Discoaster lodoensis</i>	CN	215.04	216.04	48	48
B	<i>Rhabdosphaera inflata</i>	CN	222.69	222.74	48.5	48.5
B	<i>Discoaster sublodoensis</i>	CN	228.68	229.28	49.3	49.3
T	<i>Tribrachiatius orthostylus</i>	CN	247.15	247.70	51	51
T	<i>Morozovella formosa</i>	PF	256.09	260.27	50.8	50.8
B	<i>Morozovella aragonensis</i>	PF	272.07	281.38	52.76	52.76
B	<i>Discoaster lodoensis</i>	CN	275.58	276.53	52.4	52.4
T	<i>Morozovella aequa</i>	PF	281.38	283.79	52.89	52.89
T	<i>Discoaster multiradiatus</i>	CN	286.42	287.92	53	53
B	<i>Sphenolithus radians</i>	CN	287.92	289.42	53.3	53.3
B	<i>Tribrachiatius orthostylus</i>	CN	295.30	296.20	53.4	53.4
B	<i>Morozovella formosa</i>	PF	316.29	318.00	54	54
T	<i>Subbotina triangularis</i>	PF	327.93	329.99	54.07	54.07
B	<i>Subbotina velascoensis</i>	PF	327.93	329.99	54.17	54.17
B	<i>Discoaster diastypus</i>	CN	328.78	329.99	53.9	53.9
B	<i>Globanomalina australiformis</i>	PF	329.99	335.09	55.5	55.5
B	<i>Igorina broedermanni</i>	PF	335.09	335.15	54.7	54.7
T	<i>Stensioeina beccariiiformis</i>	BF	335.61	335.71	55.0	55.0
T	<i>Globanomalina pseudomenardii</i>	PF	348.97	352.73	55.9	55.9
T	<i>Acarinina mckannai</i>	PF	348.97	352.73	56.3	56.3
B	<i>Morozovella subbotinae</i>	PF	356.08	367.53	55.9	55.9
B	<i>Morozovella aequa</i>	PF	356.08	367.53	56.5	56.5
B	<i>Discoaster multiradiatus</i>	CN	357.50	358.25	56.2	56.2
B	<i>Discoaster nobilis</i>	CN	366.34	367.18	56.5	56.5
B	<i>Acarinina soldadoensis</i>	PF	371.06	380.56	56.5	56.5
B	<i>Heliolithus riedelii</i>	CN	388.15	388.65	57.3	57.3
B	<i>Discoaster mohleri</i>	CN	389.65	390.45	57.5	57.5
B	<i>Heliolithus kleinpellii</i>	CN	400.23	400.65	58.2	58.2
B	<i>Sphenolithus anarrhopus</i>	CN	400.23	400.65	58.4	58.4

Notes: T = top, B = bottom. o = oldest, y = youngest. PF = planktonic foraminifers, CN = calcareous nannoplankton, BF = benthic foraminifers, PMAG = paleomagnetic reversals.
This table is also available in [ASCII](#).

Table T16. Age model, linear sedimentation rates, and mass accumulation rates, Site 1263.

Age (Ma)	Depth (mcd)	LSR	Growth Factor	Corrected LSR	Dry density (g/cm ³)	CaCO ₃ (wt%)	Total MAR (g/cm ² /k.y.)	CaCO ₃ MAR (g/cm ² /k.y.)	Noncarbonate MAR (g/cm ² /k.y.)
1	5.22	5.22	1.18	4.42	0.96	93.7	0.42	0.397	0.027
2	10.49	5.27	1.18	4.47	0.98	94.6	0.44	0.414	0.024
3	15.79	5.30	1.18	4.49	1.20	94.2	0.54	0.507	0.031
4	22.21	6.42	1.18	5.44	1.26	95.9	0.69	0.659	0.028
5	29.13	6.92	1.18	5.87	1.26	96.3	0.74	0.712	0.028
6	31.01	1.88	1.18	1.60					
7	32.50	1.49	1.18	1.26	1.14	94.7	0.14	0.136	0.008
8	33.30	0.80	1.18	0.68		93.1			
9	34.02	0.72	1.18	0.61					
10	34.73	0.71	1.18	0.60					
11	35.44	0.71	1.18	0.60					
12	36.15	0.71	1.18	0.60					
13	36.87	0.71	1.18	0.60					
14	37.58	0.71	1.18	0.60					
15	38.29	0.71	1.18	0.60					
16	39.00	0.71	1.18	0.60					
17	39.71	0.71	1.18	0.60					
18	40.41	0.70	1.18	0.60					
19	41.11	0.70	1.18	0.59					
20	41.81	0.70	1.18	0.59					
21	42.50	0.69	1.18	0.59					
22	43.19	0.69	1.18	0.58					
23	43.87	0.68	1.18	0.58					
24	44.55	0.68	1.18	0.58					
25	45.23	0.68	1.18	0.58					
26	46.00	0.77	1.18	0.65					
27	47.50	1.50	1.18	1.27					
28	49.86	2.36	1.18	2.00	1.15	90.1	0.23	0.207	0.023
29	54.45	4.59	1.18	3.89	1.21	93.3	0.47	0.438	0.031
30	60.39	5.94	1.18	5.03	1.20	94.5	0.60	0.569	0.033
31	69.00	8.61	1.18	7.29	1.19	94.1	0.87	0.817	0.051
32	78.70	9.70	1.18	8.22	1.18	82.3	0.97	0.797	0.172
33	86.84	8.14	1.18	6.90	1.24	94.5	0.85	0.806	0.046
34	104.10	17.26	1.18	14.63	1.25	93.1	1.82	1.696	0.126
35	109.35	5.25	1.18	4.45	1.23	88.1	0.55	0.483	0.065
36	113.26	3.92	1.18	3.32	1.27	92.7	0.42	0.392	0.031
37	122.88	9.62	1.18	8.15	1.30	93.6	1.06	0.990	0.067
38	132.84	9.96	1.18	8.44					
39	137.63	4.78	1.18	4.05	1.32	93.9	0.54	0.502	0.033
40	140.31	2.68	1.18	2.27	1.25	91.6	0.28	0.261	0.024
41	146.05	5.75	1.18	4.87					
42	153.87	7.82	1.18	6.62	1.27	93.5	0.84	0.785	0.054
43	165.07	11.20	1.18	9.50	1.29	92.2	1.22	1.126	0.096
44	176.29	11.21	1.18	9.50	1.31	90.6	1.24	1.126	0.117
45	186.16	9.87	1.18	8.37	1.31	93.6	1.10	1.030	0.070
46	196.00	9.84	1.18	8.34	1.34	95.9	1.12	1.073	0.045
47	205.77	9.77	1.18	8.28	1.39	94.2	1.15	1.084	0.066
48	215.54	9.77	1.18	8.28	1.32	95.8	1.09	1.044	0.046
49	226.59	11.05	1.18	9.37	1.31	96.1	1.23	1.179	0.048
50	235.57	8.98	1.18	7.61	1.39	93.7	1.06	0.991	0.067
51	247.43	11.85	1.18	10.05	1.39	95.5	1.39	1.331	0.062
52	268.26	20.84	1.18	17.66	1.35	93.8	2.39	2.238	0.147
53	286.30	18.04	1.18	15.29	1.48	95.9	2.27	2.177	0.092
54	320.00	33.70	1.18	28.56	1.43	93.9	4.10	3.845	0.252
55	339.00	19.00	1.18	16.10	1.40	63.8	2.26	1.440	0.817
56	353.70	14.70	1.18	12.46	1.39	93.3	1.73	1.616	0.116
57	380.98	27.28	1.18	23.12	1.38	92.6	3.18	2.945	0.235
58	398.16	17.18	1.18	14.56	1.46	83.4	2.12	1.771	0.352

Notes: LSR = linear sedimentation rate, MAR = mass accumulation rate. This table is also available in ASCII.